ISBN 978-82-326-3672-3 (printed ver.)
ISBN 978-82-326-3673-0 (electronic ver.)
ISSN 1503-8181

Doctoral theses at NTNU, 2019:34

Akash Pakanati

Towards 3D Modelling of Macrosegregation Formation and Modification in DC Casting of Aluminium Alloys Accounting for Equiaxed Grain Growth and Transport

Akash Pakanati

Doctoral thesis

Doctoral theses at NTNU, 2019:34

NTNU
Norwegian University of Science and Technology
Thesis for the Degree of
Philosophiae Doctor
Faculty of Natural Sciences
Department of Materials Science and
Engineering

NTNU
Norwegian University of
Science and Technology

NTNU

NTNU
Norwegian University of
Science and Technology

Akash Pakanati

Towards 3D Modelling of Macrosegregation Formation and Modification in DC Casting of Aluminium Alloys Accounting for Equiaxed Grain Growth and Transport

Thesis for the Degree of Philosophiae Doctor

Trondheim, February 2019

Norwegian University of Science and Technology
Faculty of Natural Sciences
Department of Materials Science and Engineering

NTNU
Norwegian University of
Science and Technology

NTNU
Norwegian University of Science and Technology

Thesis for the Degree of Philosophiae Doctor

Faculty of Natural Sciences
Department of Materials Science and Engineering

ISBN 978-82-326-3672-3 (printed ver.)
ISBN 978-82-326-3673-0 (electronic ver.)
ISSN 1503-8181

Doctoral theses at NTNU, 2019:34

Printed by NTNU Grafisk senter

“All we have to decide is what to do with the time that is given to us.”

- *Gandalf to Frodo in LOTR, Fellowship of the Ring*

List of Publications

This thesis work is based on the following publications:

Paper I

Akash Pakanati, Mohammed M'Hamdi, Hervé Combeau and Miha Založnik, "INVESTIGATION OF MACROSEGREGATION FORMATION IN ALUMINIUM DC CASTING FOR DIFFERENT ALLOY SYSTEMS ", *Metallurgical and Materials Transactions A, Vol 49, Issue 10, pp 4710-4721, October 2018*.

DOI: https://doi.org/10.1007/s11661-018-4731-z

Paper II

Akash Pakanati, Mohammed M'Hamdi, Hervé Combeau and Miha Založnik, "3D MACROSEGREGATION MODELLING OF DC CASTING OF ALUMINIUM ALLOY AND ITS COMPARISON WITH 2D MODEL AND EXPERIMENT", Prepared manuscript be submitted.

Paper III

Knut Omdal Tveito, Akash Pakanati, Mohammed M'Hamdi, Hervé Combeau and Miha Založnik, " A SIMPLIFIED THREE-PHASE MODEL OF EQUIAXED SOLIDIFICATION FOR THE PREDICTION OF MICROSTRUCTURE AND MACROSEGREGATION IN CASTINGS ", *Metallurgical and Materials Transactions A*, *Vol 49, Issue 7, pp 2778-2794, July 2018.*

DOI: https://doi.org/10.1007/s11661-018-4632-1

Paper IV

Akash Pakanati, Knut Omdal Tveito, Mohammed M'Hamdi, Hervé Combeau and Miha Založnik, "APPLICATION OF AN EQUIAXED GRAIN GROWTH AND TRANSPORT MODEL TO STUDY MACROSEGREGATION IN A DC CASTING EXPERIMENT", revised version submitted to *Metallurgical and Materials Transactions A*.

Paper V

Akash Pakanati, Knut Omdal Tveito, Mohammed M'Hamdi, Hervé Combeau and Miha Založnik, "IMPACT OF INLET FLOW ON MACROSEGREGATION FORMATION ACCOUNTING FOR GRAIN MOTION AND MORPHOLOGY EVOLUTION IN DC CASTING OF ALUMINIUM", *Light Metals*, *Pages 1089-1096, March 2018.*

DOI: https://doi.org/10.1007/978-3-319-72284-9_142

Paper VI
Akash Pakanati, Mohammed M'Hamdi, Hervé Combeau and Miha Založnik, "3D NUMERICAL ANALYSIS OF MACROSEGREGATION FORMATION IN DC CASTING OF ALUMINIUM ALLOYS ACCOUNTING FOR INLET FLOW AND GRAIN MORPHOLOGY AND TRANSPORT ", Prepared manuscript be submitted.

Statement of author contributions

I performed the numerical simulations based on the numerical model developed by Knut Omdal Tveito. Prof. Mohammed M'Hamdi, Prof. Hervé Combeau and Dr. Miha Založnik contributed in defining the problem statements and analyzing the simulation data. Knut Omdal Tveito also participated in some of these discussions. I wrote all the manuscripts with a substantial contribution by Knut Omdal Tveito for Paper II. All of them were involved in reviewing the manuscripts.

Other scientific contributions

Conference Paper

- 3D MODELLING OF THE IMPACT OF INLET FLOW ON MACROSEGREGATION FORMATION IN DC CASTING OF ALUMINIUM ALLOYS ACCOUNTING FOR GRAIN MORPHOLOGY AND TRANSPORT
  Akash Pakanati, Mohammed M'Hamdi, Hervé Combeau and Miha Založnik
  The 7th International Conference on Solidification and Gravity, September 2018, Miskolc, Hungary

- ANALYSIS OF THE INTERPLAY BETWEEN THERMO-SOLUTAL CONVECTION AND EQUAIXED GRAIN MOTION IN RELATION TO MACROSEGREGATION FORMATION IN AA5182 SHEET INGOTS
  Akash Pakanati, Knut Omdal Tveito, Mohammed M'Hamdi, Hervé Combeau and Miha Založnik
  The Minerals, Metals and Materials Society (TMS) Conference, March 2019, San Antonio, USA

Oral Presentation (presenter underlined)

- IMPACT OF INLET FLOW ON MACROSEGREGATION FORMATION ACCOUNTING FOR GRAIN MOTION AND MORPHOLOGY EVOLUTION IN DC CASTING OF ALUMINIUM
  Akash Pakanati, Knut Omdal Tveito, Mohammed M'Hamdi, Hervé Combeau and Miha Založnik
  The Minerals, Metals and Materials Society (TMS) Conference, March 2018, Phoenix, USA

- MODIFICATION OF MACROSEGREGATION FORMATION IN DC CASTING OF ALUMINIUM ALLOYS WITH INLET FLOW AND ACCOUNTING FOR EQUIAXED GRAIN GROWTH AND TRANSPORT: A NUMERICAL STUDY
  Akash Pakanati, Knut Omdal Tveito, Mohammed M'Hamdi, Hervé Combeau and Miha Založnik
  Nasjonal Konferanse for Materialteknologi, 2018, May Oslo, Norway

- 3D MODELLING OF THE IMPACT OF INLET FLOW ON MACROSEGREGATION FORMATION IN DC CASTING OF ALUMINIUM ALLOYS ACCOUNTING FOR GRAIN MORPHOLOGY AND TRANSPORT
  Akash Pakanati, Mohammed M'Hamdi, Hervé Combeau and Miha Založnik
  The 7th International Conference on Solidification and Gravity, September 2018, Miskolc, Hungary

Poster Presentation (presenter underlined)

- NUMERICAL INVESTIGATION OF MACROSEGREGATION MECHANISMS IN DC CASTING FOR DIFFERENT ALLOY SYSTEMS
  Akash Pakanati, Mohammed M'Hamdi, Hervé Combeau and Miha Založnik
  The Minerals, Metals and Materials Society (TMS) Conference, March 2018, Phoenix, USA

Preface

This thesis is submitted to the Norwegian University of Science and Technology (NTNU) for partial fulfilment of the requirements for the degree of philosophiae doctor.

This doctoral work has been performed at the Department of Materials Science and Engineering Faculty of Natural Sciences and Technology, NTNU, Trondheim, with Professor Mohammed M'Hamdi as main supervisor.

Funding for this work is provided within the framework of PRIMAL project of which Hydro Aluminium AS, Alcoa Norway AS, Aleris Rolled Products Germany GmbH and Institute of Energy Technology (IFE), Norway are project partners. The PRIMAL project is supported by Research Council of Norway. NOTUR High Performance Computing program provided the necessary computational resources required to conduct this work.

Acknowledgments

"Each generation stands on the shoulders of those who have gone before them, just as I did as a young PhD student in Cambridge, inspired by the work of Isaac Newton, James Clerk Maxwell and Albert Einstein."

- ***Stephen Hawking***

Several researchers across the world have been working in the field of solidification science, casting process and numerical modelling. This research work was possible only by standing on their shoulders and I would like to take this opportunity to thank them all. Related to my work, I would like to show my gratitude to the following people-

- My supervisor Prof. Mohammed M'Hamdi, firstly for providing me with the opportunity to do my PhD work under his supervision. He has supported me in every possible way, academic and non-academic, during my stay in his group. His patience, encouragement and active support was extremely helpful in shaping up the research progress. I am always indebted to the creative and organizational freedom he has given me. He has taken a lot of time in reviewing every article, conference paper and this thesis. I am grateful for his patience and feedback; the latter has been unequivocally responsible for the betterment of my scientific writing aptitude.
- Co-supervisors Prof. Herve Combeau and Dr. Miha Založnik, for suggesting this project for my PhD thesis. Regular discussions of simulation results with them were important to improve my understanding of the subject. I would like to thank them for advising me in preparing the topics for journal articles and their encouragement at every step. A special thanks to Dr. Miha Založnik for showing patience in reviewing some of the manuscripts.
- Co-supervisor Dr. Kjerstin Ellingsen, for the regular discussions on various topics related to my work. I would like to thank her for providing me with some data to run deformation simulations and for reviewing some of my work.
- Co-supervisor Prof. Yanjun Li, for taking active interest in my work and providing me with kind and encouraging words every time we meet.
- Knut Omdal Tveito, for engaging in active discussions with respect to software development in OpenFoam and providing me with the inhouse code "KSIM".
- Dr. Sylvain Gouttebroze, for reviewing an important manuscript based on 3D macrosegregation simulations.

- Numerous colleagues at SINTEF, Oslo for several kinds of support, including Ms. Nina Dahl, Dr. Christian Simensen, Dr. Trond Aukrust, Dr. Xiang Ma, Dr. Amin S. Azar and Dr. Qiang Du.
- The people at Department of Materials Science and Engineering, NTNU, especially Prof. Jostein Mårdalen, Prof. Knut Marthinsen, Ms. Hilde Martinsen Nordø, Ms. Elin Synnøve Isaksen Kaasen for their organizational support.
- The people at Research and Technology Development (RTD) at Hydro Aluminium AS, Sunndaløra for providing me with time, flexibility and resources to finish this work.
- My friend Sofie Vega Wollbraaten, for proof reading this technical manuscript in spite of having a non-technical background.
- My friends in India, Europe and USA for always being there to talk and discuss casual things in spite of being separated in time and space.
- My parents and family members, for being a strong support system I could rely on, especially during testing times. Their encouragement and love, in spite of being thousands of kilometers away, is something I will always cherish.

Abstract

Macrosegregation refers to the inhomogeneous distribution of solute elements at the scale of cast product. It is a severe defect affecting the quality of cast product produced through Direct Chill (DC) casting process. Several casting process parameters like casting speed, cooling rate, inoculants, inlet melt flow etc. affect macrosegregation formation. Shrinkage induced flow, natural convection and equiaxed grain motion are some of the macroscopic transport processes contributing to macrosegregation formation. Of these, equiaxed grain motion and its interplay with other transport mechanisms leading to macrosegregation formation is not well understood. The complexity increases when the grain morphology is accounted for which further influences macrosegregation formation. Experimental studies provide limited insight and are both expensive and difficult to perform. This is where numerical tools, complemented with increase in computational resources in recent times, offer the scope to provide an improved understanding of these complex interactions especially accounting for grain morphology. The goal of this work is to establish a numerical framework within which the effects of transport mechanisms with focus on grain motion and morphology on macrosegregation formation can be studied. Additionally, the effect of modification of the inlet melt flow on macrosegregation is studied using this framework. Furthermore, we move from 2D sheet ingot simulations to full scale 3D sheet ingot simulations providing an opportunity to assess the impact of space on macrosegregation formation.

A previously published two-phase volume averaged solidification model is used to study the effect of the alloy elements (Mg, Cu and Zn) on macrosegregation formation in 2D sheet ingots by studying the transport mechanisms individually and in combination. Mg is lighter than Al whereas Cu and Zn are heavier. This modified the natural convection which further effected the other transport mechanisms, especially grain settling. As a consequence, the mechanisms contributing to macrosegregation depended on the type of the alloy, in spite of the relative macrosegregation formation being similar for all three alloys considered. To study the influence of spatial variations on macrosegregation, the same model was used to conduct a comparison study of 3D and 2D sheet ingot simulation against experiment. For open inlet, both 2D and 3D (in the center) sheet ingot simulations compared well with each other and had a reasonable agreement with the experiments. Since the simulation was done in 3D, the horizontal macrosegregation map could be compared with experiment for the first time.

The two-phase model is extended to a simplified three-phase model, as a part of this work, to also account for grain morphology. The simplified three-phase model is novel in its approach as it solves for the grain growth kinetics accounting for three phases (solid, intragranular liquid and extragranular liquid) but solves for the macroscopic transport accounting for only two phases (solid and liquid), similar to the two-phase model. This simplification significantly reduces the computational cost and complexity of its numerical implementation. The simplified model is verified against the full three-phase model and it is shown that the model is viable and is able to accurately predict recalescence. The simplified model

gives somewhat more dendritic morphologies than full model but captures the morphology transition well. This simplified three-phase model is also validated against experimental data for AA7050 on axis symmetric billets. A good correlation between experiment and simulation is obtained.

Macrosegregation reduction or optimization is important to maintain ingot quality. The first step towards achieving this is by modifying macrosegregation by controlling process parameters. This has been investigated experimentally in the recent times by modifying the inlet flow. Equiaxed grains usually settle at the center of the ingot and an inlet jet was used to resuspend these solute lean grains. This resuspension resulted in macrosegregation modification and in some cases macrosegregation reduction. An attempt is made to complement these experimental studies by numerically modifying macrosegregation by introducing an inlet jet. This qualitative study is conducted on axis symmetric billets and 3D sheet ingots using the simplified three-phase model. It is shown that macrosegregation modification due grain resuspension is possible by using an inlet jet. The extent of modification depended on the grain morphology: globular or dendritic.

Contents

1. Introduction

1.1. Aluminium: Some Background

Aluminium is formed by fusion reactions in stars where a single proton is added to Magnesium. But on earth, Aluminium is found in the crust. It is the most abundant metal found in the universe and third most abundant element found on earth after Oxygen and Silicon [1]. Owing to its reactive nature, it is never found in its pure form. Bauxite is the most important ore for aluminium extraction. Though various scientists and engineers tried to extract pure aluminium during the 19th century, the cost of the extraction of pure aluminium remained higher than the cost of extraction of pure gold. This resulted in aluminium being called "Metal of Kings"! [2]. True to its name, the price of 1kg aluminium was about $1200 in 1850s in comparison to $664 per kg for gold. By 1859, the price of aluminium came down to $34 per kg as potassium was replaced with much cheaper sodium used in the reaction to isolate aluminium. Aluminium prices dropped to around $1.2 per kg in 1895 due to the discovery of Hall-Heroult electrolytic process a decade earlier. From then onwards, the world's production of aluminium increased exponentially and it is used in a wide variety of products ranging from an aluminium foil to cover food to the aluminium body of an aircraft. Some of the interesting applications and facts of aluminium are described below.

- Aluminium is light weight and has a density of approximately one-third of the density of steel. In addition to this, the mechanical strength to weight ratio aluminium is a contributing factor for its application in aerospace and automotive sector. The major weight of aircraft and spacecraft bodies is from aluminium. In the automotive sector, aluminium is gaining importance due to its recyclability.
- The electrical conductivity of aluminium is only about 60 percent that of copper per cross section area. Nonetheless, it is used in the electrical transmission lines due to its light weight.
- Recycling aluminium needs only 5 percent of energy required to extract pure aluminium from its ore. This is a very important aspect for reduction of environmental pollution. Estimates indicate that about 75 percent of aluminium ever made is still in use because of recyclability.
- Aluminium should in principle be a highly corrosive metal. It is highly reactive with oxygen and loses an electron easily, the same process which results in rusting of iron. Surprisingly, the reaction product aluminium oxide sticks to the metal and forms a fine layer which shields the metal from further decay. This property offers the possibility of using aluminium in packaging and shipping industry.

Due to these interesting and economically important properties, engineers and scientists' interest in aluminium never ceases.

1.2. Aluminium Alloys

Aluminium is a soft, light weight, ductile and malleable metal. Its elastic modulus is around 70 GPa, about one third of steel. This would result in greater deformation of an engineering component for a given load when compared to that of steel. To make it stronger and more durable, it is mixed with different alloying elements. For example, to survive the heat and temperature loads in an aircraft or car engine, we usually mix aluminium with copper. For packaging, we need aluminium which can be easy to shape and seal. This can be done by mixing it with magnesium. As mentioned before, aluminium is used in transmission lines owing to its lightweight even though copper conducts electricity more efficiently. In order to retain the efficiency, aluminium is alloyed with boron which has comparable efficiency to that of copper. Other metals which are used to make aluminium alloys are lithium, manganese, silicon, tin, zinc etc. Depending on the application, these alloys are mixed with aluminium. But aluminium alloys generally have 90-99 percent pure aluminium. Detailed information of influence of alloys on aluminium are well documented [3]. Aluminium alloys can be classified into primary and secondary alloys based on the impurities present. Primary alloys are produced from electrolysis and have negligible impurities. Secondary alloys are obtained from recycled material and have higher impurities.

1.3. Aluminium Production

Fig 1-1 shows the step by step production of aluminium [4]. Due to its reaction with oxygen, aluminium is never found in its pure form. Aluminium exists in the Earth`s crust as bauxite ore. This ore has one third water molecules embedded into the crystal structure of aluminium oxide. Also, there could be other impurities in the bauxite ore. Getting pure aluminium requires a multi stage process where different kinds of impurities, water and oxygen are removed at different steps.

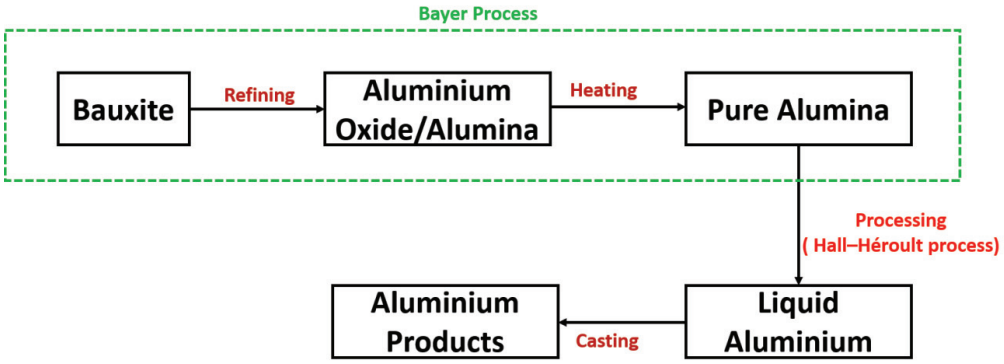

Fig 1-1 Schematics of Aluminium Production

The raw bauxite is extracted from earth and is washed off in the production plants and passed through a grinder. This powder is mixed with hot solution of caustic soda and lime to separate alumina (or aluminium oxide). This process is called refining. Alumina obtained after refining is heated and filtered

to obtain pure alumina. The pure alumina is dried to a white powder. The whole process up to this point is known as the Bayer Process. In the processing stage, Hall Héroult process is typically employed. Extra raw materials are used to obtain pure aluminium, carbon and electricity. Electricity is run between cathode and anode, both made up of carbon. Oxygen in the alumina reacts with the anode and forms carbon dioxide. What remains is pure liquid aluminium which can be tapped and cast into products of desired shape and size. The casting product might or might not result in the final product. Mould casting is an example of casting methodology which produces the desired product directly. But in case of ingot or billet casting, aluminium is cast into an intermediate product which is subsequently used to transform into finished products.

1.4. DC Casting of Aluminium Alloys

In commercial aluminum alloy processing, semi-continuous Direct-Chill (DC) casting is an important industrial casting process for producing ingots (for rolling sheets of aluminum) or round billets (for extrusion) which can be up to 10m long and up to 2m wide. A schematic representation of the DC casting process is shown in Fig 1-2. The liquid metal at melt temperature enters from the top. It starts to solidify against the water-cooled moulds (primary cooling) and is further cooled directly by water jets underneath the mould (secondary cooling). As the liquid solidifies, the solidified metal is pulled down with a pre-defined casting speed. We can see three regions from Fig 1-2: the liquid zone indicated in blue, the solid zone indicated in red and the mushy zone indicated by different colors. The mushy zone comprises of both liquid and solid.

The existence and extent of the mushy zone can be pointed to the fact that most alloys solidify over a range of temperatures instead of a precise melting point T_m [5]. During the solidification interval, solid phase nucleates and grows as equixed dendrites in the liquid during DC Casting of aluminium alloys. This forms an isotropic mushy zone where the solid and liquid co-exist in a temperature interval that depends on the alloy composition. With increase in alloy composition, the thickness of this mushy zone increases. Understanding the mushy zone dynamics is critical in understanding the formation of major defects during the casting process. Some common defects observed during DC Casting are described in the next section.

1.5. DC Casting Defects

Several defects are observed during the solidification of the melt during DC Casting. Some of them are porosity, hot tears, macrosegregation etc. [5]. These defects also occur in other forms of casting process, like in the case continuous casting of steel. These defects can form early during the solidification process or during the later stages. Porosity for example can manifest in many forms [6]. However, the most severe form is microporosity. This defect occurs mainly due to shrinkage porosity or gas porosity. The former mechanism occurs due to the density difference between the liquid and solid phase. This is observed deep within the mushy zone and as a result, there is restrictive feeding leading to formation of pores. Gas porosity on the other hand is due to the presence of gaseous elements in the liquid melt. During solidification, these gaseous elements condense during the early stages of solidification and result in pore formation. The presence of pores due to either of the mechanisms will be detrimental to

the mechanical behavior of the alloy. These pores act like local stress concentrators and promote cracks thereby lowering the fatigue life of the alloy.

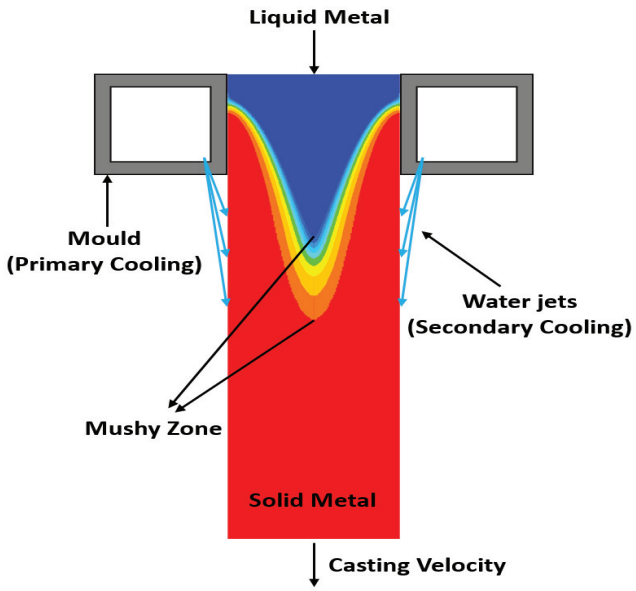

Fig 1-2 Direct Chill (DC) Casting Process

In addition to restrictive feeding due to shrinkage porosity, mushy zone subjected to tensile stress can result in aggravated condition and results in hot tear (or hot cracking) formation. Porosity causes uniform distribution of pores within the mushy zone but a hot tear is localized at grain boundaries [7].

Another important casting defect commonly encountered is macrosegregation. It refers to the solute inhomogeneity at the scale of casting [7]. Heat treatment of solidified product will not be able to remove this defect due to the forbidding time scale of solid state diffusion. Assuming $D_s \approx 10^{-13}\, m^2 s^{-1}$ and L=1 m, the diffusion time is around 125,000 years. Like porosity, macrosegregation can result in variations of mechanical properties of ingot. It therefore becomes important to understand the underlying phenomena resulting in macrosegregation. It is here that numerical tools have become indispensable in understanding, modelling and controlling macrosegregation. Macrosegregation is positive when the composition of the alloy is above the nominal value and negative when the composition of the alloy is below the nominal value. A typical macrosegregation profile can be seen in Fig 1-3. At the center of the cast product, negative segregation is typically observed. It is followed by positive segregation in the immediate vicinity of the center. Negative sub-surface and positive surface segregation is observed as we move away from the center of the ingot. Before we move to study

macrosegregation formation, we need to understand microsegregation which happens at the scale of secondary dendrite arm of an equiaxed grain.

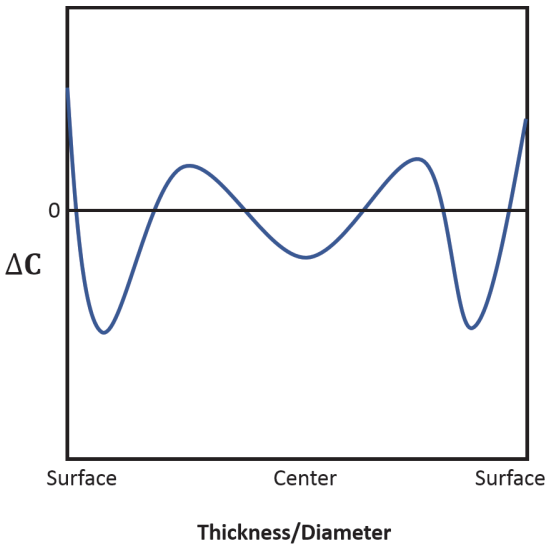

Fig 1-3 Macrosegregation pattern in DC casting process

1.6. Microsegregation

Compositions of solid and liquid phases evolve as solidification proceeds. The solubility of solute in liquid phase and solid phase is different. In eutectic alloys typically used in DC Casting process, the primary solid phase has solute content lower than that of liquid phase. This can be better explained with the help of a phase diagram. Fig 1-4 shows the simplified phase diagram of Al-Cu with solidification path of Al-10wt%Cu.

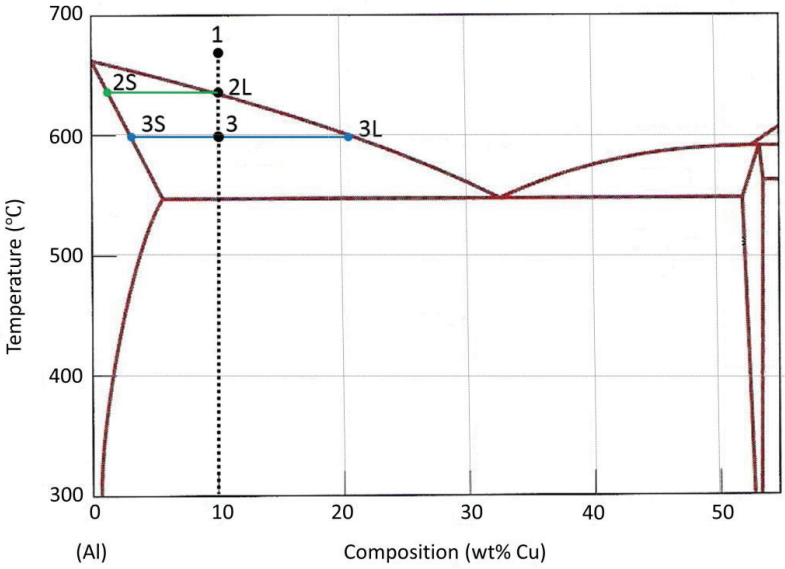

Fig 1-4 Simplified phase diagram of Al-Cu

At point 1, we have pure liquid and the composition is uniform and nominal – here 10wt% Cu. As the system cools down, we reach point 2L. At that instant, solid is formed with solute content lower than the nominal concentration as indicated by point 2S. As the system further cools down to point 3, the solute content in the solid reaches 3S whereas the solute content in liquid reaches 3L. Though the solute content is higher at 3S compared to 2S, the solute content in liquid is much higher compared to the content in solid at the given temperature (2S<2L and 3S<3L). This redistribution of solute is characterized by the partition coefficient (k_p) given in Eq. (1-1) and this occurs at the scale of a secondary dendrite arm (10-100 μm). This phenomenon is known as microsegregation [8].

$$k_p = \frac{C_s}{C_l} \tag{1-1}$$

1.7. Macrosegregation and its Mechanisms

The solute rejected at the microscopic scale is redistributed macroscopically due to several transport mechanisms or due to the relative motion between solid and liquid phase resulting in macrosegregation formation [7]. This relative motion can manifest in many forms and understanding them is very important in understanding overall macrosegregation formation. The mechanisms of relative motion (also referred as transport mechanisms) are discussed in this section. Fig 1-5 shows the schematics of various transport mechanisms resulting in macrosegregation formation.

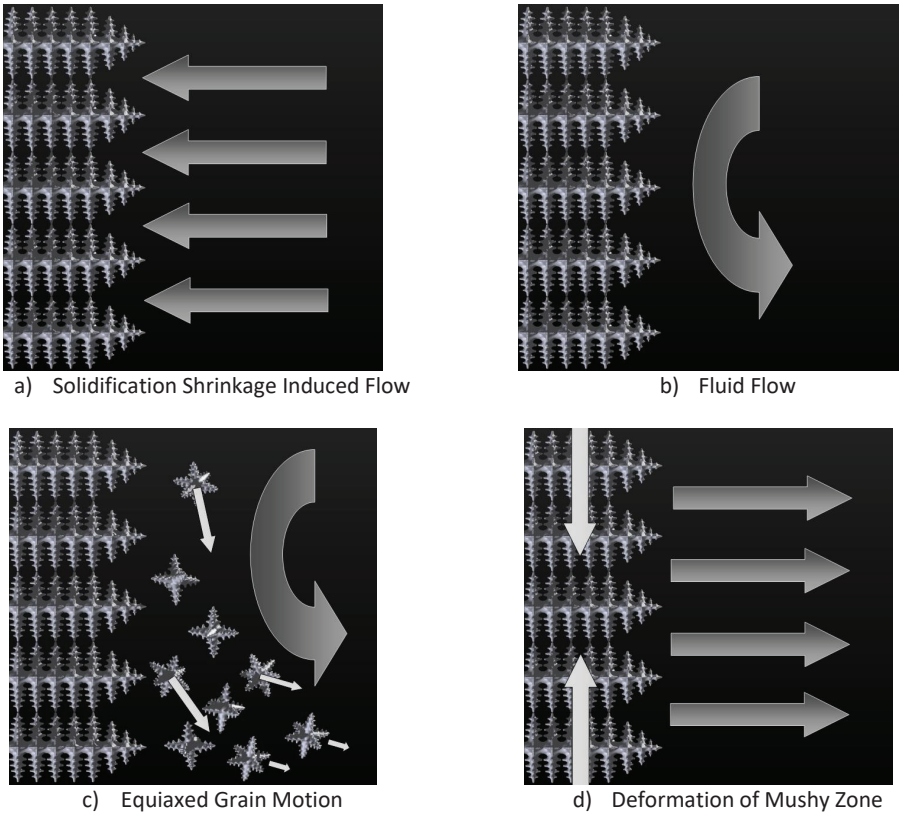

a) Solidification Shrinkage Induced Flow
b) Fluid Flow
c) Equiaxed Grain Motion
d) Deformation of Mushy Zone

Fig 1-5 Macrosegregation Mechanisms [7]

- **Solidification shrinkage induced flow** occurs due to the increase in density when the liquid metal solidifies into solid metal. Due to the volume change or contraction of the solid, flow is induced to feed the contraction. This flow occurs in the deeper parts of mushy zone where the enrichment on liquid is high. This causes solute redistribution resulting in macrosegregation. Negative segregation at the center of the ingot and positive segregation at the surface of the ingot during DC casting process is typically due to solidification shrinkage induced flow [9].
- **Natural and forced convection** causes complex flow pattern resulting in macrosegregation formation. Natural convection is normally due to the combination of thermal convection and solutal convection. This arises due to the density variations due to thermal and compositional gradients in the liquid. Forced convection can be induced by the inlet mechanism, magnetic fields, stirring etc.
- **Equiaxed Grain Motion** is another known cause of macrosegregation. Equiaxed grain nucleation is due to the heterogenous nucleation in the melt due to inoculation in DC Casting process. For alloys used in DC Casting process, these equiaxed grains are formed by rejecting solute in the surroundings. These solute lean grains at lower solid fractions of mushy zone are not connected

to any structure and are free to move – settle or float depending on their density relative to liquid phase. The movement of these grains can cause redistribution of solute, resulting in negative segregation to the regions they are transported to.

- **Deformation of Mushy zone** occurs in deeper parts of mushy zone where the mush starts to form a continuous network. It obtains the ability to transmit strains which can induce fluid flow resulting in macrosegregation. As an example, the mushy zone can be visualized as a sponge with liquid [7]. Compressing the sponge results in expulsion of the liquid and traction of the sponge results in the liquid to be sucked in.

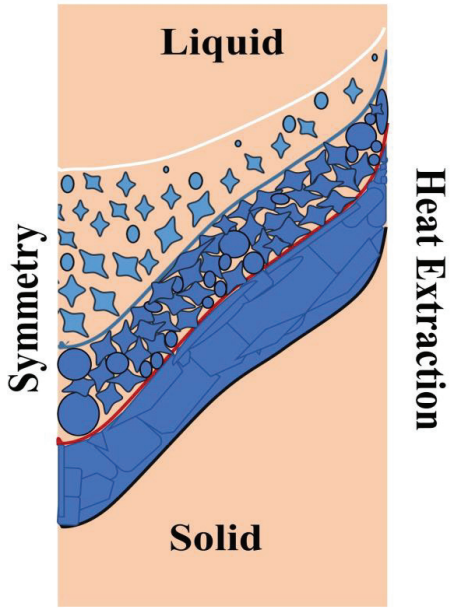

Fig 1-6 A simple representation of solidification regimes during DC Casting process

The incidence of the above-mentioned transport mechanisms depends on the region of the solidification domain in the DC Casting process. Fig 1-2 provides an overview of the three main regions in DC casting process – liquid, mushy zone and solid. In Fig 1-6 we further divide the mushy zone into three regions. It should be noted that only the half section of the ingot is shown. The regions are described below.

- The first region, called the slurry, is between the white curve and the blue curve. The white curve is the liquidus and the blue curve is the packing front (or fraction). Liquidus marks the beginning of solidification and grain nucleation and motion occurs in this region. Also, solutal and thermal convection have significant presence in this region. The packing fraction (g_{pack}) is the volume fraction at which the grains begin to interlock and cease to move. The definition of packing fraction is ambiguous and can depend on the grain morphology. Previous experimental

research estimated the value between 0.2-0.3 [10]. The value used during DC Casting modelling is usually between 0.15-0.3[11–16]

- The second region, called the packed region, is between the packing fraction and the coherency fraction, represented by the red curve. Grain motion is non-existent in this region as the grains are interlocked and begin to coalesce. The fluid flow due to thermal or solutal convection is very weak due to the low permeability of the region. Only shrinkage induced flow is active in this part.
- The third region, called the coherency region, is between the coherency fraction and the solidus (represented by black curve). The coherency fraction is the volume fraction at which the solid grains begin to form a continuous network of solid and obtain the ability to transmit thermal strains. Due to this, thermally induced deformations can occur. Along with this, shrinkage induced flow also acts in this region. The value of coherency fraction depends on the type of alloy. For example, Stangeland et al. [17] showed that the coherency region begins in the range of 0.48 to 0.97 for Al-Cu alloys with Cu concentration from 0.3 to 9 wt% Cu.

The mechanisms mentioned above together contribute to macrosegregation formation during DC Casting process of Aluminium alloys. Referring to Fig 1-3, the positive segregation at the surface is due to shrinkage induced flow. The adjacent negative segregation in the sub-surface region is due to shrinkage induced flow towards the surface resulting in depletion. In addition to this, surface exudation can also cause solute rich layer on top of solute depleted region [18]. This is not described in this work as we focus mainly on the above-mentioned mechanisms. The mechanisms contributing to negative segregation at the center and the positive segregation next to center is not well established. It is believed that shrinkage induced flow predominantly causes negative segregation at the center of the domain. Equiaxed grain settling in conjunction with thermal and solute convection can also cause negative segregation. The formation of positive segregation next to center is not well established but it is generally agreed that multiple phenomenon could contribute towards it [19].

1.8. Experimental Observations of Macrosegregation in DC casting of Aluminium Alloys

Yu and Granger provided one of the first results for macrosegregation formation in DC cast ingots [20]. The positive segregation towards the ingot surface and the negative segregation at the center of the ingot were investigated and they concluded that the former phenomena was due to shrinkage induced flow and the later phenomena was due to grain motion. They observed duplex grain structure at the center of the ingot with a mix of fine and coarse cell dendritic grains. This varying microstructure suggested different origins and thermal histories of the grains and have been transported towards the center of the ingot. Dorward and Beernsten [21] studied the relation between sump depth and macrosegregation formation. With higher casting speed, a deeper sump was observed which promoted macrosegregation. Later Gariepy and Caron [22] analyzed the impact of melt feeding system and grain refiners on macrosegregation. They observed that negative segregation increased with grain refinement. Under the European EMPACT project [23–25], macrosegregation formation for AA5182 alloy was studied under different conditions: with and without grain refiners and different kinds of melt

distribution system. They found that macrosegregation severity increases with addition of grain refiners and related this finding to the presence and transport of equiaxed grains which form typically on the grain refiners. Also, the melt distributor system played an important role in modifying macrosegregation. This showed the importance interdendritic melt flow through the porous mushy zone and demanded attention to the accurate modelling of permeability of the mushy zone.

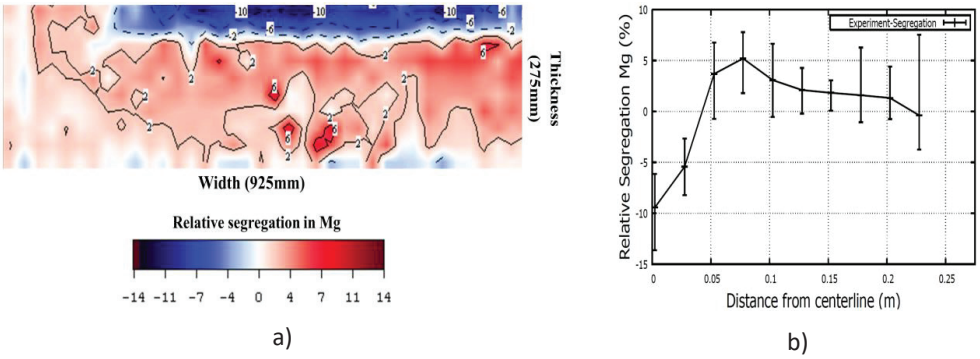

Fig 1-7 a) Relative segregation of Mg in color map on the horizontal plane for quarter ingot and b) Relative segregation of Mg along the thickness of the ingot

Fig 1-7a shows the relative macrosegregation of Mg along the horizontal plane for a casting trail where an inlet combo-bag setup and grain refiners were used [9]. For the same case, relative segregation of Mg along the ingot thickness can be seen in Fig 1-7b [26].

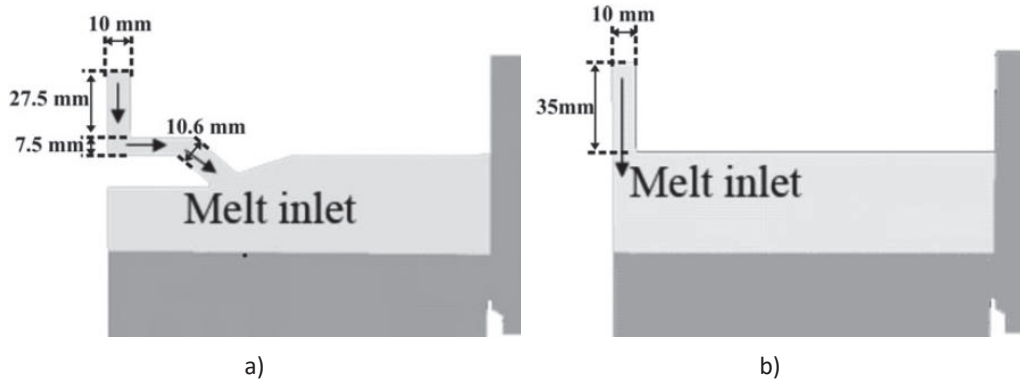

Fig 1-8 Geometry of the melt feeding systems [27]**. a) Semi-horizontal melt feeding system and b) Vertical melt feeding system**

Eskin et al. [28,29] conducted a series of experiments on Al-Cu alloy to study the impact of various process parameters on macrosegregation, microstructure and various other casting defects. They also observed that increasing casting speed increased macrosegregation in all regions of the cast product [28]. In the same paper they also discussed the impact of water flow rate in secondary cooling on macrosegregation formation and microstructure. Structure refinement was observed with increasing the flow rate although the effect was found to be minimal. Similarly, macrosegregation was also found to be minimally affected with water flow rate. They found little to no impact of inlet melt temperature on macrosegregation and the influence was restricted close to the surface [29].

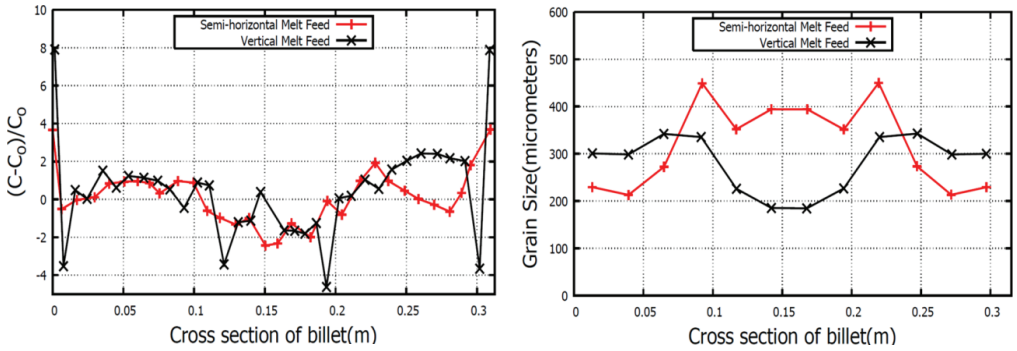

Fig 1-9 Reproduced curves [30,31] **across the billet diameter of a) relative macrosegregation of Zn for semi-horizontal and vertical melt feeding system and b) grain size for semi-horizontal and vertical melt feeding system**

Zhang et al. [27,30] carried out experiments to study the influence of melt feeding system on macrosegregation formation and grain structure in DC cast billets with AA7050 alloy. Two kinds of inlet melt system were used – a semi horizontal melt feeding system and a vertical melt feeding system, both shown in Fig 1-8. Only the half section is shown and the left vertical side for each system corresponds to symmetry axis. It was observed that the melt feeding scheme played a crucial role in macrosegregation and microstructure formation by modifying the sump profile and flow patterns. The macrosegregation pattern for Zn and microstructure profile for the two types of inlet melt system can be seen in Fig 1-9a and Fig 1-9b respectively. For the semi-horizontal melt feeding system, a gentle slope of solidification front was found. In contrast, for the vertical melt feeding system, a vertical solidification front was observed 40 mm away from the center of the billet. This was attributed to the presence of vertical jet directed towards the center of the ingot which penetrated the mushy zone creating a cliff like solidification front [27]. This work [30] also reported for the first time the recirculation of the grains by pushing them away from the center of the billet due to vertical inlet jet. But this shift in position of the settling of solute lean grains did not result in less pronounced negative segregation at the center of the

billet. In fact, severe negative segregation was observed and it was understood that the strong inlet flow could wash away solute from the center and transport it to other parts of the billet [32].

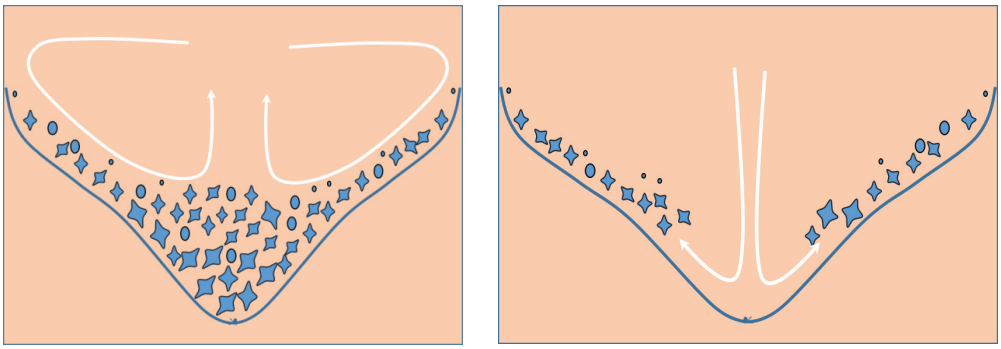

a) b)

Fig 1-10 Schematics of equiaxed grains in DC cast sump where in a) grains settle and form a packed bed at the center of the ingot and b) inlet jet penetrates the settled grains and recirculates them away from the center of the ingot. The blue line indicates packing limit – volume fraction at which grains begin to coalesce

Very recently, Wagstaff and Allanore [33–35] conducted experimental studies on sheet ingots with Al-4.5wt%Cu alloy. Similar to Zhang et al. [30], they used an inlet jet to modify macrosegregation formation. Wagstaff and Allanore proposed an optimal jet condition [33] strong enough to resuspend grains from the center of the ingot and at the same time weak enough to avoid any erosion of solute elements . An illustration of this grain resuspension can be seen in Fig 1-10. Wagstaff and Allanore [33] introduced jet Reynolds number (Re_j) which was dependent on the mold length(M_l) and width(M_w), casting velocity(V_{cast}), radius of the inlet(r) and kinematic viscosity of the liquid metal(ϑ). The expression for jet Reynolds number is given in

$$Re_j = \frac{2M_l M_w V_{cast}}{\pi r \vartheta} \tag{1-2}$$

Casting trials were conducted with standard casting procedure (combo bag) and with varying inlet jet velocity based on the jet Reynolds number. Fig 1-11 gives an illustration of the relative macrosegregation contour maps on the horizontal quarter section for two cases – inlet system with a combo bag and inlet system with a vertical jet with jet Reynolds number of 81,000. By using a combo bag, a large region of negative segregation is observed along the ingot width. But this negative segregation was eliminated by using an inlet vertical jet. Resuspension of the grains was considered as the primary reason for this effect. The existence of an optimal jet to potentially eliminate negative segregation was confirmed by this work.

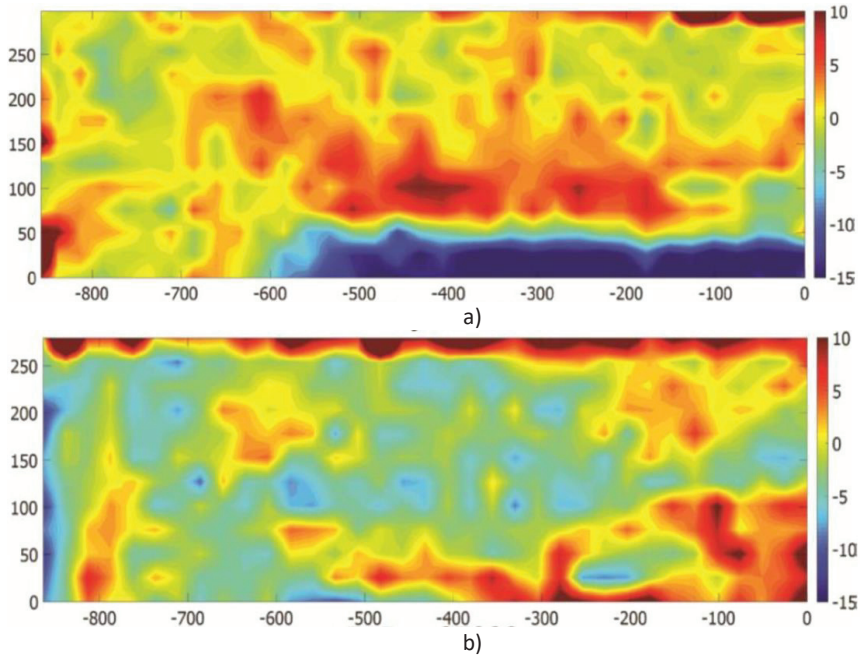

Fig 1-11 Relative macrosegregation contours measured in one quadrant of the horizontal section [33]**: a) Standard casting with combo bag and b) Using inlet jet with Re_j=81,000**

1.9. Review of Macrosegregation Modelling

In the current section we focus on the advances in mathematical modelling of macrosegregation. We first discuss the modelling aspects of alloy solidification in general and then emphasize on modelling of DC Casting process.

1.9.1. Solidification and Macrosegregation Modelling of Alloys

The first efforts to provide a quantitative expression for macrosegregation was done by Flemings and co-workers [36–38] in 1960's. The Local Solute Redistribution Equation (LSRE) proposed by them assumes perfect local mixing of solute in the liquid phase and no mixing in solid phase. Flemings showed that the incidence of macrosegregation depends on the velocity vector being parallel to the thermal gradient. The LSRE equation was modified by accounting for gravity by Mehrabian et al. [39]. Thermal buoyancy was included by calculating the change in liquid density through a temperature gradient in the mushy zone. They have also accounted for Darcy's law to calculate the flow through the mushy zone. This work was later extended to include diffusion in solid by Poirier et al. [40], Wanqi [41] and Ohnaka [42]. Ohnaka emphasized the need for 3D modelling of diffusion through primary and secondary dendrites to

accurately predict solute redistribution. The earlier models were heat transfer based where a given temperature gradient was given as input. Also, the fluid flow in the liquid and mushy zone were not coupled. These limitations were overcome with more advanced modelling in the form of multi-domain models and continuum models [43].

The first multi-domain model was proposed by Ridder et al. [44]. Two domains in the form of bulk liquid and mushy zone were considered. The segregation model allowed for the coupling of convective heat and fluid flow in the fully liquid regime ahead of the liquidus isotherm and the interdendritic fluid flow in the mushy zone. The model also extended the previous macrosegregation studies with 1D heat flow and 2D fluid flow to 2D heat flow and fluid flow in axis-symmetric conditions. Shrinkage induced flow in the mushy zone was included by using Darcy's law. Experiments were also conducted which compared well with model predictions. For the given case investigated by Ridder et al., they concluded that there was little effect of natural convection in pure liquid on the interdendritic flow in the mushy zone. For steady state solidification process, the interface between liquid and mushy zone is fixed and explicit tracking is not necessary. But for non-steady state case, the interface needs to be tracked and the mesh needs to be adapted for each calculation. This is difficult and is the biggest drawback of the above model [45].

To avoid these difficulties associated with interfacial tracking, single domain models were proposed. They are also referred to as continuum mixture models [46–50] and have been applied to various case studies [47,50]. The mixture quantities were considered as the dependent variables in the governing equations. These mixture quantities, defined in terms of solid or liquid phase, were weighted by mass or volume fractions. Ni and Incropera [51,52] extended the continuum model to account for microscopic phenomena which has important impact on the macroscopic process. Vreeman et al. [12] proposed an extension of the continuum mixture model by including the equiaxed grain motion and its effect on macrosegregation formation for binary alloys. Separate and distinct mixture momentum equations were employed to resolve the slurry region, where solid was free to move, and porous region, where solid was fixed and formed a continuous network. This work was extended by Krane [53] to account for ternary alloys. However, a major issue with these continuum models was that the interactions between the solid and liquid phases were not accounted for. As a result, the solid concentration was either averaged over both the phases or not calculated at all. This meant that the resolution of grain motion which results in negative macrosegregation in casting process was not complete. The model results in significant discrepancies when compared with experimental data [54]. To overcome this difficulty, volume averaging method was proposed which couples microscopic and macroscopic phenomena during the solidification process.

Unlike the continuum mixture models, volume average models consider two-phase and multi-phase models. For two-phase models, distinct conservation equations for solid and liquid phase are solved. They are valid in all regions and extra constitutive models are needed to describe the interfacial interactions and provide closure to the model. These models were originally developed by Beckermann and co-workers [54–57] and by Ganesan and Poirier [58]. A comprehensive description of volume averaging model is described in the subsequent sections.

The volume average models proposed until that point had many simplifications, the chief of which is fixed solid. Further extension of the model was done by Wang and Beckermann to include and improve the microstructure growth model [59] and the corresponding motion of equiaxed grains during solidification process of binary alloys [60–62]. This model introduces an additional phase, interdendritic liquid, to distinguish between solid and bulk liquid. This offered the possibility of modelling the diffusion length scales in different phases and coupling them to provide more comprehensive description of grain morphology. Schneider and Beckermann extended this model to account for multicomponent alloys [63]. Lever rule or Scheil model was not used in this model to calculate interfacial concentration, which is typically how it was done earlier. Instead, solid-state diffusion was accounted for to calculate interfacial concentration. Ludwig and Wu [64] and Wu et al. [65] simplified the model by Wang and Beckermann [60] without reducing the physics of solidification and grain sedimentation. Additional work was done by the same group to propose a new model to account for three phases and three dimensions [66,67]. Combeau et al. [68–70] stressed the importance of grain morphology on their settling and corresponding macrosegregation formation. They compared experimental macrosegregation profile in a large steel ingot to that of model predictions. Significant discrepancies were observed when grain morphology was assumed to be globular. In parallel, Wu and Ludwig [71,72] also proposed a modified volume averaged equiaxed solidification model which accounts for globular-to-dendritic (GDT) of equiaxed grains and its motion in presence of melt convection. The model considers two hydrodynamic phases – extradendritic melt and equiaxed grains and three thermodynamic phases – solid dendrites, interdentritic melt and extradendritic melt. The extradendritic melt was separated by the interdendritic melt by the grain envelope. Like the previous models, a two-phase approach is used to solve for the velocities of the hydrodynamic phases. Columnar dendritic growth was not accounted for in this model and was added later [73–76]. This resulted in a total of five thermodynamic phases - solid dendrites in equiaxed grains, the interdendritic melt between equiaxed dendrites, solid dendrites in columnar trunks, the interdendritic melt between trunk dendrites, and the extradendritic melt. Further, the five phases were subcategorized under three hydrodynamic phases - equiaxed grains consisting of solid dendrites and interdendritic melt, columnar trunks consisting of solid dendrites and interdendritic melt, and extradendritic melt. With a better morphology description, the model essentially evolved into a three-phase approach for velocity resolution of the hydrodynamic phases, thereby increasing the complexity of the model. Equiaxed grain growth was assumed to occur on grain refiners or inoculant particles. Tveito et al. [77] and Bedel et al. [78] provided an extension of the two-phase model from Combeau and Založnik [79] by modelling inoculant flow and studying its impact on macrosegregation and microstructure heterogonies for a binary alloy in a rectangular cavity. Inoculant flow is an important phenomenon during DC Casting process and this provided a platform for subsequent models. Most recently Xu [80] as a part of PhD work proposed a new grain size prediction model for inoculated aluminum alloys and compared the model predictions with experiment. Both globular and dendritic grain growth kinetics were implemented, taking GDT into account. It was observed that for well grain refined aluminium alloys, globular model provided an acceptable prediction of grain size. For poorly inoculated alloys, consideration of dendritic grain growth was important to provide better prediction of grain size when compared with experiment.

1.9.2. Solidification and Macrosegregation Modelling of DC Casting of Al alloys

The earliest attempt at modelling DC casting process can be traced back to the work done by Flood et al. in 1991 [81]. It was a simple model where solidification shrinkage was neglected and solid was assumed to be a rigid body moving with the casting speed. The model was applied to simulate DC casting process of Al-4.5wt%Cu alloy on a 210mm radius billet. They observed positive segregation at the center of the ingot due to solutal convection indicating its importance. Later Reddy and Beckermann [13] made the first attempt to model grain motion for Al-4.5wt%Cu alloy on a 533mm diameter billet. A constant grain density was assumed, and grain transport equation was added to evaluate local grain density. The grain size was calculated using the solid fraction and local grain density. In the same paper, they also presented results without grain motion and compared the model predictions with experimental data. The results from model with and without grain motion had limited correlation with experimental results but it was the first model (with grain motion) to predict negative segregation at the center of billet. For the same alloy and casting setup, Reddy and Beckermann studied the effect of permeability of mushy zone, thermal-solutal convection and solidification shrinkage induced flow [82]. The centerline segregation depends on the competition between solidification shrinkage induced flow and thermal-solutal convection, which in turn depends on the permeability of the mushy zone. High permeability results in convection dominating over shrinkage flow and results in positive segregation at the center of the billet. Low permeability results in weaker convection and shrinkage flow dominates resulting in negative segregation at the center of the billet. Also, the importance of solidification shrinkage induced flow on inverse (positive) segregation formation towards the surface of the billet was discussed.

Vreeman et al. [83] studied macrosegregation formation in DC cast billets (200 mm radius) accounting for grain motion and thermal-solutal convection. They considered two alloys Al-4.5wt%Cu and Al-6wt%Mg. In this study they assumed a constant grain diameter and they studied the impact of packing fraction (the solid fraction value at which the grains are assumed to coalesce) and characteristic grain diameter on macrosegregation formation. This parametric study showed the huge impact of these parameters on macrosegregation formation. It was also agreed that these parameters were poorly understood and difficult to evaluate from experimental studies. Overall, the macrosegregation trend for the two alloys were qualitatively similar to observed experimental profiles. In addition, the flow pattern observed for these two binary alloys was found to be different. Mg being lighter than Al, was floating to the top of the domain and interacting with incoming flow resulting in turbulence. Cu on the other hand being heavier than Al, was settling towards the center of the ingot. Vreeman et al. [10] further studied to determine the value of packing fraction by comparing model predictions of 450mm diameter billet cast with Al-6wt%Cu alloy with experiment. They concluded that the packing fraction could be less than 30% solid volume though it could depend on the position in the casting domain and casting parameters.

Jalanti [9] and Jalanti et al. [84] studied macrosegregation formation in an industrial sized (275mm thick) Al-Mg sheet ingot in 2D which was based on the experimental data from the EMPACT project [23–25]. Thermal-solutal convection and shrinkage induced flow were accounted for in the models. Jalanti concluded that the thermal-solutal convection played little to no role and shrinkage flow only contributed to macrosegregation formation. The comparison with experiments also showed reasonable

agreement, especially with negative segregation at the center of the ingot. But the positive segregation in the mid-section of the ingot was not predicted well and lack of grain motion in the model was cited as the potential reason.

Založnik and Šarler [85] and Založnik [19] studied in detail the implications of thermos-solutal flow in liquid metals by using the non-dimensional numbers (*Pr*, *Sc*, Ra_T and Ra_C). It was concluded that flow patterns are highly unstable and results in complex flow structures and fine-scale features of the concentration field. Also, the flow patterns depended on the type of alloy used – Mg being lighter than Al results in competing solutal convection with thermal convection and Cu or Zn being heavier than Al results in co-operating solutal convection with thermal convection. The importance of DC casting parameters on the flow structure in the liquid pool – casting speed and size which decides the sump depth, casting temperature which drives the thermal flow, alloy type which decides the solutal convection, partition co-efficient etc. Also the work was based on free growth model of grain initiation on inoculant particles [19] and the need for an improved microstructure model to account for grain growth dynamics in the presence of liquid melt was discussed.

Založnik et al. [11] made a systematic study of the impact of transport mechanisms (thermal-solutal convection, shrinkage induced flow, grain motion) on macrosegregation in industrial sized DC cast sheet ingot in 2D. They focused on understanding the effects of individual transport mechanisms and their combined role through various cases. The model was based on a multiscale two-phase solidification model [79] which was extended to include grain nucleation on grain refiners and grain growth. Založnik et al. [86] extended their previous work to study the coupling of flow structure in the slurry zone, grain growth and macrosegregation formation. But both the studies including the studies before, assumed grain to be globular. Bedel [26] and Bedel et al. [78,87] recently presented an advanced model of DC casting, accounting for macrosegregation formation with grain motion, coupled with nucleation on grain refiner particles and kinetics of grain growth and morphology. This model was an extension of the two-phase model [79] and was based on the volume averaging method with three hydrodynamic phases [60,88]. In her PhD thesis, Bedel [26] conducted an extensive study to compare the EMPACT experiment data with model predictions accounting for thermal-solutal convection, solidification shrinkage and grain motion. Different morphology models were included to account for grain motion- globular morphology, dendritic morphology with hemispherical tip growth [8] and dendritic morphology with paraboloid tip growth [89]. It was concluded that taking the grain motion and morphology into account, reasonable model prediction of grain size was possible when compared with experiment. But the macrosegregation pattern, accounting for grain morphology and variation of packing fraction, did not yield good correlation with experimental macrosegregation profiles. Also, the need for 3D simulation was discussed when it comes to modelling sheet ingots.

The most recent work in DC casting modelling was done by Heyvaert et al. [90]. Their work pushed the envelope of understanding the coupling between microstructure and macrosegregation at the process scale. The model study was supported by experimental work [10] where two conditions were used – with grain refiners and without grain refiners. Model predictions of macrosegregation showed the presence of grain motion in grain refined cases with globular morphology showing the best comparison with experiment. The non-grain refined cases were modelled by reducing the inoculant density and

better comparison of macrosegregation prediction with the experimental profiles was possible when grain morphology was accounted for. This showed the presence of dendritic grains (which result in less severe segregation) in non-grain refined case. A detailed investigation on the dendrite tip model was conducted and it was shown that hemispherical model over predicts the dendritic morphology and a paraboloid tip model could capture the morphology transition from dendritic to globular as a function of grain density. The need for improved microstructure model accounting for transition of grain morphology and an extensive comparison of the models with well characterized experiments was also discussed.

Macrosegregation formation for alloys and more specifically during DC casting process has been and is still under investigation. All the recent work in this field discussed in the previous paragraphs uses the volume average method [57] to model the solidification process. The current work also builds on that method which is described briefly in the next sections.

1.10. Scope of Current Work

Significant efforts have been put to understand macrosegregation formation using experimental methods in the last few decades. These were being complemented with numerical studies. Especially for analyzing the contributions of transport phenomena like natural and forced convection, shrinkage induced flow, transport of equiaxed grains etc. However, grain motion and its interplay with other transport mechanisms leading to macrosegregation formation is still in its early stages of understanding. This is mainly due to the challenges in modelling all the coupled effects, especially when grain morphology needs to be accounted for. Additionally, previous numerical studies were mostly conducted using 2D simulations (for sheet ingots). This might provide an unrealistic flow pattern and an incomplete description of macrosegregation formation due to the asymmetric shape of the ingot. The goal of this work is to introduce a 3D framework within which the effects of the grain motion and morphology, its interplay with other transport processes can be studied. Within the framework, the concept of macrosegregation modification by resuspension of equiaxed grains with an inlet jet (forced convection) is also explored. This goal is approached by subtasks which are described below.

Influence of alloy elements and 3D space on macrosegregation

DC casting of aluminium employs a variety of alloying elements: Mg, Cu, Zn etc. Mg is lighter than Al whereas Cu and Zn are heavier than Al. Solutal convection, which forms a part of natural convection, is affected by the lighter or heavier alloys. This in turn affects the overall strength of natural convection. By studying the transport mechanisms both individually and in combination, the influence of alloy elements on transport mechanisms and their interplay with grain motion leading to macrosegregation formation can be assessed. A study is conducted by considering a simplified 2D sheet ingot with three binary alloys: Al-4.5wt%Mg, Al-4.5wt%Cu and Al-8.375wt%Zn. A two-phase globular grain growth model based on Ref [11,79] is used in this study. This work is covered in *paper I.* Since the previous study is in 2D, it is important to assess the influence of 3D space on macrosegregation. This assessment can be performed by comparing with 2D simulation. The capability of the model to handle 3D simulations can be further established by comparing the simulation results with experiment. The importance of grain motion on macrosegregation formation is also discussed. This work is covered in *paper II.*

Development and validation of a simplified three-phase grain growth model

Globular grain growth model is a simple model which assumes spherical grains. This model provides a reasonable insight into macrosegregation formation. Experimental studies indicate that the grain structure can be dendritic, and this influences the interplay between morphology and various transport mechanisms, which can further influence macrosegregation occurrence. This calls for an improved microstructure model accounting for dendritic morphology. At the same time, a complex grain growth model also increases the complexity of its numerical implementation. Hence a simplified three-phase model is proposed which has all the ingredients of a three-phase model, but the implementation is similar to that of a two-phase model. The model development, its validation against the full three-phase model and its limited verification on a DC cast ingot is presented in *paper III.*

The proposed model is then used to conduct a validation study by comparing the model predictions of macrosegregation and microstructure with that of experimental studies on an axis symmetric billet for AA7050 alloy. This work is covered in *paper IV.*

Application of the simplified-three phase grain growth model

Macrosegregation optimization or reduction is a subject of high scientific and economic interest. Recent experimental studies have established the possibility of macrosegregation modification by resuspension of equiaxed grains due to the inlet jet for Al-4.5wt%Cu [91]. Studies are conducted in this work to numerically simulate macrosegregation modification by using an inlet vertical jet and comparing it with standard inlets. First, the simplified three-phase model is applied to study macrosegregation modification due to inlet flow for an AA7050 alloy in an axis symmetric billet. Resuspension of equiaxed grains and its relation to macrosegregation modification is presented. Additionally, the relative ease with which globular and dendritic grains can be resuspended is also discussed. This is covered in *paper V*.

The work conducted in *paper V* is extended by studying macrosegregation modification in a 3D sheet ingot. The extent of modification is also addressed by accounting for the grain morphology. As previous studies were conducted using 2D models for sheet ingots, this work provides the opportunity for the first time to study the complex 3D flow pattern and its subsequent effect on macrosegregation. This work is covered in *paper VI.*

2. Mathematical Modelling of Macrosegregation

Mathematical modelling of the solidification process and macrosegregation formation, based on previous works and novel to the current work is discussed in this chapter.

2.1. Conservation Equations and Volume Averaging Technique

Solidification is characterized by three distinctive phases - solid, liquid and mushy region. In mushy zone, the solid and liquid phases exist in equilibrium. The treatment of mushy zone is crucial due to its influence on casting defects like macrosegregation and hot tearing. Hence a mathematical framework is required to account for this two-phase region in addition to accounting for individual phases. An isotropic mushy zone is defined, and the solid and liquid phases are free to move and interact. In the current work, the mathematical model of solidification process is based on volume averaged conservation equations [57].

The mass, momentum and energy conservation equations are applicable at all length scales of solidification - from dendrites to full domain. Owing to morphological complexities and widely different length and time scales, direct application of conservation equations to dendrites and quantities of similar sizes is difficult. A simple but effective work around for this problem is to use a macroscopic model which is developed by averaging the microscopic model over a finite size control volume. This way, each phase can be treated separately apart from explicitly considering the interaction between the phases. The advantage of this method is two ways: the microscopic data is imbibed in the macroscopic model and the macroscopic transport process is connected directly to the microscopic processes like interfacial mass, heat transfer and stresses and microstructure evolution. Additionally, the averaged conservation equations explicitly contain micro-scale parameters such as the phase volume fractions, grain density, interfacial area concentration, local diffusion lengths, drag coefficients etc. [92]. In the subsequent section, microscopic equations are presented. Next the volume averaging method is explained which eventually leads us to the averaged macroscopic conservation equations.

2.1.1. Microscopic Conservation Equations

For a specific quantity $\emptyset$, the microscopic transport equation can be written using Reynolds transport theorem:

$$\frac{\partial \emptyset_k}{\partial t} + \nabla \cdot (\emptyset_k \vec{v}_k) = -\nabla \cdot \boldsymbol{J}_k + S_k \tag{2-1}$$

Depending on the type of equation, $\emptyset$ can represent mass ρ, momentum $\rho\vec{v}$, enthalpy ρh or species concentration ρc. $\boldsymbol{J}$ is a tensor of one order greater than that of $\emptyset$. It accounts for diffusion of momentum, heat or species while *S* is a source term. The subscript *k* is used to indicate different phases.

The microscopic equations for mass, momentum, enthalpy and species for a particular phase *k* are given from Eq. (2-2) to (2-5).

$$\frac{\partial \rho_k}{\partial t} + \nabla \cdot (\rho_k \vec{v}_k) = 0 \tag{2-2}$$

$$\frac{\partial \rho_k \vec{v}_k}{\partial t} + \nabla \cdot (\rho_k \vec{v}_k \vec{v}_k) = -\nabla \cdot \boldsymbol{\sigma}_k + b_k \tag{2-3}$$

$$\frac{\partial \rho_k h_k}{\partial t} + \nabla \cdot (\rho_k h_k \vec{v}_k) = -\nabla \cdot \boldsymbol{q}_k \tag{2-4}$$

$$\frac{\partial \rho_k c_k}{\partial t} + \nabla \cdot (\rho_k c_k \vec{v}_k) = -\nabla \cdot \boldsymbol{j}_k \tag{2-5}$$

$\boldsymbol{\sigma}$ is the stress tensor, *b* is the body force, $\boldsymbol{q}$ is the heat flux and $\boldsymbol{j}$ is the species diffusion flux. The equations must be solved for both the liquid and solid phases. This reduces *k* to either *s* or *l* depending on the domain being solid or liquid.

2.1.2. Volume Averaging Method

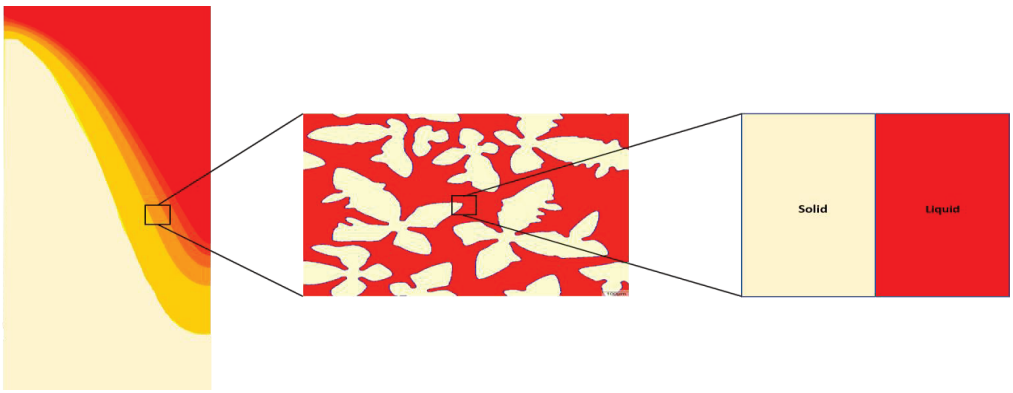

a) b) c)

Fig 2-1 Length Scales in Solidification Process

The interfacial configuration in solidification process is quite complex. Its impractical to solve the conservation equations at the microscopic level. Especially providing boundary conditions and front tracking in the mathematical model becomes very difficult. To avoid these issues, the microscopic conservation equations are averaged over a macroscopic volume which is smaller than the actual length scale of the domain but larger when compared to the scales of microstructures. By using this scale, we are able to capture the macroscopic heat and fluid transfer and smooth out the details of the morphological complexities. The different length scales in the solidification process are represented in Fig 2-1. Red color here represents liquid phase and light gold color represents the solid phase. The mushy zone is represented by intermediate colors as can be seen in Fig 2-1a. Process scale (Fig 2-1a) has orders of 10^{-1} m to 10^{-0}m and 10^{-5} m to 10^{-4}m for the interfacial structures (Fig 2-1c). The resulting size of the volume averaged element (Fig 2-1b) would be between 10^{-3} m to 10^{-2}m.

The complete mathematical framework is laid out in literature [57] and only the main idea is presented here. Each phase *k* in the control volume *dV* occupies volume dV_k and it is bounded by interfacial area A_k. This interface has a velocity $\vec{w}_k$. We introduce the phase function ς_k which takes the value of 1 in phase *k* and 0 in other phases. The volume fraction of phase *k* is defined as

$$g_k = \frac{dV_k}{dV} \tag{2-6}$$

For a quantity $\psi(x,t)$ in phase *k,* its volume average over the entire volume *dV* can be given by $< \psi >$

$$< \psi_k >= \frac{1}{dV}\int_{dV} \psi_k \, \varsigma_k(x,t) dV \tag{2-7}$$

The intrinsic volume average is given by

$$< \psi_k >^k = \frac{1}{dV_k}\int_{dV} \psi_k \, \varsigma_k(x,t) dV = \frac{< \psi_k >}{g_k} \tag{2-8}$$

When $< \psi_k >^k$ is uniformly distributed in dV_k, we have $< \psi_k >^k = \psi_k$. The fluctuating component is the deviation of ψ_k from the intrinsic volume averaged quantity $< \psi_k >^k$.

$$\widehat{\psi}_k = (\psi_k - < \psi_k >^k) g_k \tag{2-9}$$

The fluctuating component is zero in a phase *k* when ψ_k is uniformly distributed.

2.1.3. Macroscopic Conservation Equations

Multiplying the microscopic conservation equations by ς_k, integrating it over volume *dV* and using the averaging methods mentioned in the previous section, we obtain the macroscopic transport equation for phase *k*

$$\frac{\partial g_k \emptyset_k}{\partial t} + \nabla \cdot (g_k \emptyset_k \vec{v}_k) = -\nabla \cdot \boldsymbol{J}_k + S_k + I_k^j + I_k^w + I_k^f \tag{2-10}$$

The microscopic equations have introduced three more additional terms compared to microscopic equation given by Eq. (2-1).

$$I_k^j = \frac{1}{dV}\int_{dA_k} \boldsymbol{J}_k . \mathrm{n}_k dA \tag{2-11}$$

$$I_k^w = \frac{1}{dV}\int_{dA_k} \emptyset_k (\vec{w}_k - \vec{v}_k) . \mathrm{n}_k dA \tag{2-12}$$

$$I_k^f = \nabla . \frac{1}{dV}\int_{dV} (\widehat{\emptyset}_k \hat{v}_k) dV = - < \widehat{\emptyset}_k \hat{v}_k > \tag{2-13}$$

I_k^j represents the diffusion of ∅ through solid-liquid interface dA_k, I_k^w is the interfacial transfer due to phase change and I_k^f represents the dispersive fluxes. Fluctuating terms are not included in accordance to the literature based on this theory[57]. Hence $< \rho_k >^k = \rho_k$, $< \mu_k >^k = \mu_k$, $< c_k^p >^k = c_k^p$ and $< D_k >^k = D_k$. This results in the following macroscopic conservation equations.

$$\frac{\partial g_k \rho_k}{\partial t} + \nabla \cdot \left(g_k \rho_k < \vec{v}_k >^k \right) = \Gamma_k \tag{2-14}$$

$$\frac{\partial g_k \rho_k < \vec{v}_k >^k}{\partial t} + \nabla \cdot \left(g_k \rho_k < \vec{v}_k >^k < \vec{v}_k >^k \right) = \nabla . < \boldsymbol{\sigma}_k >^k + g_k < b_k >^k + M_k \tag{2-15}$$

$$\frac{\partial g_k \rho_k < c_k >^k}{\partial t} + \nabla \cdot \left(g_k \rho_k < c_k >^k < \vec{v}_k >^k \right) = -\nabla \cdot \boldsymbol{j}_k + J_k \tag{2-16}$$

$$\frac{\partial g_k \rho_k < h >^k}{\partial t} + \nabla \cdot \left(g_k \rho_k < h_k >^k < \vec{v}_k >^k \right) = -\nabla \cdot \boldsymbol{q}_k + Q_k \tag{2-17}$$

The newly added terms are described below.

$$\Gamma_k = I_k^w, \qquad \emptyset_k = \rho_k \tag{2-18}$$

$$M_k = I_k^j + I_k^w, \qquad \emptyset_k = \rho_k < \vec{v}_k >^k \tag{2-19}$$

$$J_k = I_k^j + I_k^w, \qquad \emptyset_k = \rho_k < c_k >^k \tag{2-20}$$

$$Q_k = I_k^j + I_k^w, \qquad \emptyset_k = \rho_k < h_k >^k \tag{2-21}$$

In case the averaged macroscopic equations from different phases are added within the given averaging volume *dV*, the terms $\Gamma_k, M_k, J_k \; and \; Q_k$ sum to zero as the mass, momentum, solute and heat lost by one phase is gained by the other phase. This leads to:

$$\sum_k I_k^j = 0 \; and \; \sum_k I_k^w = 0 \tag{2-22}$$

Meticulous modelling of the interfacial terms is avoided by this approach. When porosity is not considered, only two phases (solid and liquid) are present in the mushy zone, i.e., *k=s* or *k=l* and $g_s + g_l = 1$.

2.2. Microstructure Modelling

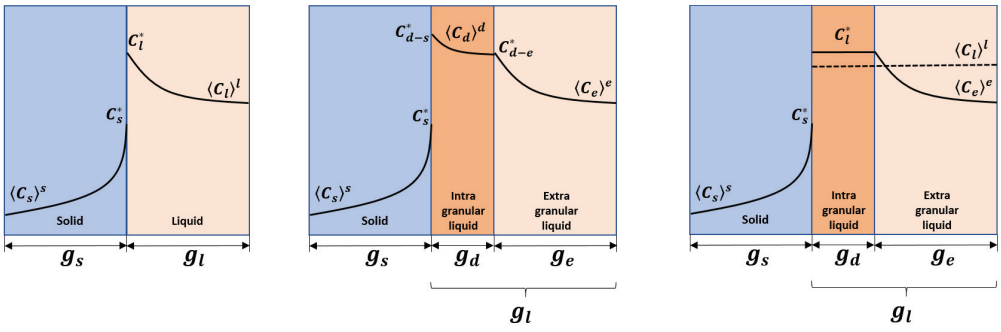

Fig 2-2 1D schematics of the grain growth models a) Two-Phase, b) Three-Phase and c) Simplified Three-Phase

The importance of an accurate microstructure model to predict macrosegregation formation has been established in the previous sections. In the following sections, we discuss in detail the two microstructure models we use in this thesis work: two-phase model based on Ref [79] and a simplified three-phase model novel to this work. The simplified three phase model is derived from the three-phase model based on Refs [60,93,94]

2.2.1. Two-Phase Grain Growth Model

The two-phase grain growth model consists of two phases – solid and liquid ($g_s + g_l = 1$) and a simple 1D schematics can be seen in Fig 2-2a. The grains are assumed to be spherical or globular throughout their growth history. But coupling the grain growth model with macroscopic transport process introduces additional problems due to the separation of scales, both length and time. Resolving the full set of coupled equations and solving them numerically requires extremely small time steps. To avoid this problem we employ a splitting methodology proposed by Založnik and Combeau [79]. The equations are decoupled so that they are treated separately in two stages. In the first stage, the convective terms are globally resolved to obtain change due to macroscopic transport. In the second stage, the local contributions of grain growth kinetics are resolved and integrated to obtain change due to grain growth, initialized from the transport solution. The two contributions are added to obtain the total variation. By doing this, we use different time scales to treat macroscopic transport and grain growth kinetics. An illustration of the splitting methodology is provided by using a generic equation:

$$\frac{\partial \varphi}{\partial t} = A\varphi + B\varphi \tag{2-23}$$

Here *A* and *B* are the convective and growth terms respectively. When we use the splitting scheme, the above equation can be resolved as follows:

$$\frac{\partial \varphi^{tr}}{\partial t} = A\varphi^{tr}, \;\; \varphi^{tr}(t_o) = \varphi_o \quad \text{on } [t_o, t_o + \Delta t] \tag{2-24}$$

$$\frac{\partial \varphi^{gr}}{\partial t} = B\varphi^{gr}, \;\; \varphi^{gr}(t_o) = \varphi^{tr}(t_o + \Delta t) \quad \text{on } [t_o, t_o + \Delta t] \tag{2-25}$$

The superscripts *tr* and *gr* represent the transport and growth step respectively. The final value of the iteration is given by $\varphi^{gr}(t_o + \Delta t)$. The introduction of splitting can introduce error and the viability of the scheme depends on how small the error is. This error analysis and solution algorithm is provided in Ref [79]. Now we focus our attention on application of the splitting method on conservation equations for a binary alloy system. The mass and solute balance equations for transport phase based on Fig 2-2a are written:

$$\frac{\partial}{\partial t}(\rho_s g_s) + \nabla \cdot (\rho_s g_s \langle \vec{v}_s \rangle^s) = 0 \tag{2-26}$$

$$\frac{\partial}{\partial t}(\rho_l g_l) + \nabla \cdot \left(\rho_l g_l \langle \vec{v}_l \rangle^l\right) = 0 \tag{2-27}$$

$$\frac{\partial}{\partial t}(\rho_s g_s \langle C_s \rangle^s) + \nabla \cdot (\rho_s g_s \langle \vec{v}_s \rangle^s \langle C_s \rangle^s) = 0 \tag{2-28}$$

$$\frac{\partial}{\partial t}\left(\rho_l g_l \langle C_l \rangle^l\right) + \nabla \cdot \left(\rho_l g_l \langle \vec{v}_l \rangle^l \langle C_l \rangle^l\right) = 0 \tag{2-29}$$

Diffusion and growth are treated in the second step and we write mass and solute balance equations for the growth phase:

$$\frac{\partial}{\partial t}(\rho_s g_s) = \Gamma_s \tag{2-30}$$

$$\frac{\partial}{\partial t}(\rho_l g_l) = -\Gamma_s \tag{2-31}$$

$$\frac{\partial}{\partial t}(\rho_s g_s \langle C_s \rangle^s) = \Gamma_s C_s^* + \frac{\rho_s S_v D_s}{\delta_s}(C_s^* - \langle C_s \rangle^s) \tag{2-32}$$

$$\frac{\partial}{\partial t}\left(\rho_l g_l \langle C_l \rangle^l\right) = -\Gamma_s C_l^* + \frac{\rho_l S_v D_l}{\delta_l}\left(C_l^* - \langle C_l \rangle^l\right) \tag{2-33}$$

Here, Γ_k is the mass flux of phase *k* at the phase interface due to phase change, C_k^* is the interface concentration, δ_k is the diffusion length of phase *k*, D_k is the diffusion coefficient for phase *k* and S_v is the interfacial area density. Also, the solute balance at the solid liquid interface is given by Eq (2-34).

$$\Gamma_s(C_l^* - C_s^*) = \frac{\rho_s S_v D_s}{\delta_s}(C_s^* - \langle C_s \rangle^s) + \frac{\rho_l S_v D_l}{\delta_l}\left(C_l^* - \langle C_l \rangle^l\right) \tag{2-34}$$

Evaluation of diffusion lengths and interfacial area density are key to this grain growth model. Various models have been proposed [59,60,71,88,93] and they are summarized by Bedel [26]. For spherical

grain, we model them similar to the model proposed in by Ni and Beckermann [95] and the expressions are presented in Table 2-1.

Table 2-1 Closing relations for two-phase model

Geometric relations for globular grains

$$R_s = \left(\frac{3g_s}{4\pi N_g}\right)^{1/3}, \quad S_v = 4\pi(R_s)^2 N_g$$

Diffusion Lengths

$$\delta_s = \frac{R_s}{5}, \delta_l = min\left\{R_s\left(\frac{1}{1-g_s^{\frac{1}{3}}} + \frac{Sc^{\frac{1}{3}}Re^{n(Re)}}{3(1-g_s)}\right)^{-1}, R_s\right\}$$

where, $n(Re) = \frac{2Re^{0.28}+4.65}{3(Re^{0.28}+4.65)}$, $Re = \frac{\rho_l(1-g_s)(2R_s)}{\mu_l}\left|\langle\vec{v}_s\rangle^s - \langle\vec{v}_l\rangle^l\right|$, $Sc = \frac{\mu_l}{\rho_l D_l}$

Phase Diagram

$$C_s^* = k_p C_l^*$$

Where R_s, N_g, μ_l, *Sc* and *Re* are the radius of the grain, local grain density, viscosity of the liquid phase, Schmidts number and Reynolds number, respectively. Once diffusion lengths and interfacial area density values are evaluated, they can be used to estimate the solute concentration (C_l^*) at the solid-liquid interface and the mass flux of solid phase at the phase interface due to phase change (Γ_s). Then we use this information to calculate the diffusion flux into solid ($\frac{\rho_s S_v D_s}{\delta_s}(C_s^* - \langle C_s\rangle^s)$) and liquid ($\frac{\rho_l S_v D_l}{\delta_l}\left(C_l^* - \langle C_l\rangle^l\right)$) phases respectively. By this we can estimate the grain growth at each time step. A detailed explanation of this procedure is available in Ref [79].

2.2.2. Full and Simplified Three-Phase Grain Growth Model

The modelling of grain growth by considering two phases is simple. However, it does not represent realistic physics and usually results in over prediction of macrosegregation formation as reported by Combeau et al. [68]. The grain growth is usually dependent on the solutal diffusion at the solid-liquid interface. An accurate evaluation of this solutal profile also depends on the interfacial area which further depends on the morphology of the grain. By considering a spherical morphology in globular grain, the model predictions are far from accurate. Hence, accounting for dendritic morphology is important and the model development has been in the works since 1980s. First the three-phase grain growth model is introduced and it is simplified in the subsequent section. The 1D schematics of the three-phase model is shown in Fig 2-2b. In the three-phase model we consider solid (*s*), intragranular liquid (*d*) and extragranular liquid (*e*) phases. A simple representation of the grain structure can be seen in Fig 2-3b. The intragranular liquid phase (g_d) is separated by the extragranular liquid phase (g_e) by an envelope (dashed line), a smooth surface enclosing the primary solid (g_s). The volume fraction relations between each phase is given below.

$$g_s + g_d + g_e = 1 \tag{2-35}$$

$$g_d + g_e = g_l \tag{2-36}$$

$$g_{env} = g_s + g_d \tag{2-37}$$

While the two liquid phases are the same hydrodynamic phases, they are treated separately to describe the different scales of diffusion arising from the dendritic morphology in the volume average methodology. Also, the densities of the two liquid phases are identical and equal to the density of the average liquid phase ($\rho_d = \rho_e = \rho_l$). Using the splitting method again, we write the macroscopic conservation equations for mass and solute balance for each phase:

$$\frac{\partial}{\partial t}(\rho_s g_s) + \nabla \cdot (\rho_s g_s \langle \vec{v}_s \rangle^s) = 0 \tag{2-38}$$

$$\frac{\partial}{\partial t}(\rho_l g_d) + \nabla \cdot \left(\rho_l g_d \langle \vec{v}_l \rangle^d\right) = 0 \tag{2-39}$$

$$\frac{\partial}{\partial t}(\rho_l g_e) + \nabla \cdot (\rho_l g_e \langle \vec{v}_l \rangle^e) = 0 \tag{2-40}$$

$$\frac{\partial}{\partial t}(\rho_s g_s \langle C_s \rangle^s) + \nabla . (\rho_s g_s \langle \vec{v}_s \rangle^s \langle C_s \rangle^s) = 0 \tag{2-41}$$

$$\frac{\partial}{\partial t}\left(\rho_l g_d \langle C_d \rangle^d\right) + \nabla \cdot \left(\rho_l g_d \langle \vec{v}_l \rangle^d \langle C_d \rangle^d\right) = 0 \tag{2-42}$$

$$\frac{\partial}{\partial t}(\rho_l g_e \langle C_e \rangle^e) + \nabla \cdot (\rho_l g_e \langle \vec{v}_l \rangle^e \langle C_e \rangle^e) = 0 \tag{2-43}$$

Similarly, we write the microscopic conservation equations for all the phases:

$$\frac{\partial}{\partial t}(\rho_s g_s) = \Gamma_s \tag{2-44}$$

$$\frac{\partial}{\partial t}(\rho_l g_d) = \Gamma_{env} - \Gamma_s \tag{2-45}$$

$$\frac{\partial}{\partial t}(\rho_l g_e) = -\Gamma_{env} \tag{2-46}$$

$$\frac{\partial}{\partial t}(\rho_s g_s \langle C_s \rangle^s) = \Gamma_s C_s^* + \frac{\rho_s S_v^s D_s}{\delta_s}(C_s^* - \langle C_s \rangle^s) \tag{2-47}$$

$$\frac{\partial}{\partial t}\left(\rho_l g_d \langle C_d \rangle^d\right) = \Gamma_{env} C_{d-e}^* - \Gamma_s C_{d-s}^* + \frac{\rho_l S_v^{env} D_l}{\delta_{d-e}}\left(C_{d-e}^* - \langle C_d \rangle^d\right) + \frac{\rho_l S_v^s D_l}{\delta_{d-s}}\left(C_{d-s}^* - \langle C_d \rangle^d\right) \tag{2-48}$$

$$\frac{\partial}{\partial t}(\rho_l g_e \langle C_e \rangle^e) = -\Gamma_{env} C_{d-e}^* + \frac{\rho_l S_v^{env} D_l}{\delta_{e-d}}(C_{d-e}^* - \langle C_e \rangle^e) \tag{2-49}$$

Where S_v^{env} is the interfacial area density for the grain envelope and S_v^s is the interfacial area density of the solid inside the envelope. The solutal balance at the interface between solid-intragranular liquid and intragranular-extragranular liquid are given below:

$$\Gamma_s(C^*_{d-s} - C^*_s) = \frac{\rho_s S^s_v D_s}{\delta_s}(C^*_s - \langle C_s\rangle^s) + \frac{\rho_l S^s_v D_l}{\delta_{d-s}}\left(C^*_{d-s} - \langle C_d\rangle^d\right) \tag{2-50}$$

$$0 = \frac{\rho_l S^{env}_v D_l}{\delta_{d-e}}\left(C^*_{d-e} - \langle C_d\rangle^d\right) + \frac{\rho_l S^{env}_v D_l}{\delta_{e-d}}(C^*_{d-e} - \langle C_e\rangle^e) \tag{2-51}$$

Now we introduce the following simplifications to the three-phase model. The simplified three-phase model is illustrated in Fig 2-2c.

$$\frac{S^s_v D_l}{\delta^{d-s}_l} \to \infty, \quad \frac{S^{env}_v D_l}{\delta^{d-e}_l} \to \infty \tag{2-52}$$

$$C^*_l = C^*_{d-s} = C^*_{d-e} = \langle C_d\rangle^d \tag{2-53}$$

$$\langle \vec{v}_l\rangle^d = \langle \vec{v}_l\rangle^e = \langle \vec{v}_l\rangle^l \tag{2-54}$$

$$g_l\langle C_l\rangle^l = g_d C^*_l + g_e\langle C_e\rangle^e \tag{2-55}$$

We assume perfect diffusion in the intragranular liquid, expressed by Eq. (2-52). Due to this, we introduce the average concentration of the intragranular liquid which becomes equal to the interfacial concentration as shown in Eq. (2-53). As mentioned in the beginning, we treat the two liquid phases as the same hydrodynamic phases. This assumption allows us to replace the intragranular and extragranular liquid velocity with averaged liquid velocity as given by Eq. (2-54). It is also convenient to express the solute mass balance for the liquid phases in terms of averaged liquid concentrations as shown in Eq. (2-55). Using these simplifications, we can further resolve the system of equations given from Eq. (2-44) to Eq. (2-50). The full derivation is not presented here and can be referred to in Paper III. The final system of solute conservation equations for the solid, liquid and interfacial solute balance is given from Eq. (2-56) to Eq. (2-58).

$$\frac{\partial}{\partial t}(\rho_s g_s\langle C_s\rangle^s) = \Gamma_s C^*_s + \frac{\rho_s S^s_v D_s}{\delta_s}(C^*_s - \langle C_s\rangle^s) \tag{2-56}$$

$$\frac{\partial}{\partial t}\left(\rho_l g_l\langle C_l\rangle^l\right) = -\Gamma_s C^*_l + \frac{\rho_l S^{env}_v D_l}{\delta_{e-d}}\frac{g_l}{g_e}\left(C^*_l - \langle C_l\rangle^l\right) \tag{2-57}$$

$$\Gamma_s(C^*_l - C^*_s) = \frac{\rho_s S^s_v D_s}{\delta_s}(C^*_s - \langle C_s\rangle^s) + \frac{\rho_l S^{env}_v D_l}{\delta_{e-d}}\frac{g_l}{g_e}\left(C^*_l - \langle C_l\rangle^l\right) \tag{2-58}$$

The simplified three-phase model solute conservation equations (Eq. (2-56)-(2-58)) has few additional terms (marked in red), when compared with the two-phase model solute conservation equations (Eq. (2-32) - (2-34)). These terms account for the third phase in the microscopic growth step and the transport step remains the same with two conservation equations for solid and liquid respectively.

As discussed in the previous section, the two-phase grain growth is due to the solute diffusion across the solid-liquid interface. In the three-phase grain growth, along with solute diffusion, the solidification is also governed by the dendritic tip growth kinetics. In principle, the three-phase grain growth is a combination of primary solidification and the dendrite tip growth. This tip growth can be evaluated by considering a hemispherical profile [8] or parabolic profile [89]. In the current work, we use the hemispherical tip growth model. The closing relations to evaluate diffusion lengths, interfacial areas, dendrite tip velocities are given in Table 2-2. The tip velocity is given by V_{tip}.

Table 2-2 Closing relations for the simplified three-phase model

Geometric relations for dendritic grains

$$R_f = \left(\frac{3}{4\pi N_g}\right)^{1/3}$$

$$R_s = R_f g_s^{1/3}, \quad S_v^s = 4\pi (R_s)^2 N_g$$

$$R_{env} = R_f g_{env}^{1/3}, \quad S_v^{env} = 4\pi (R_{env})^2 N_g$$

Dendrite tip kinetics

$$\Gamma_{env} = \rho_l S_v^{env} V_{tip}$$

$$V_{tip} = \frac{\partial R_{env}}{\partial t} = \left[\frac{D_l m_l C_l^* (k_p - 1)}{\Gamma_{GT}}\right] (\Omega)^2 \, , Supersaturation\ ratio\ \Omega = \frac{g_l}{g_e}\frac{\left(C_l^* - \langle C_l \rangle^l\right)}{C_l^*(1-k_p)}$$

Diffusion Lengths

$$\delta_s = \frac{R_s}{5}, \delta_{e-d} = = d\left\{\frac{d}{R_{env}} - \frac{f(R_{env},\Delta)+g\left(R_f,R_{env},\Delta\right)}{d\left[R_{env}+d-(R_{env}+\Delta+d)e^{-\frac{\Delta}{d}}\right]-f(R_{env},\Delta)+\left(e^{-\frac{\Delta}{d}}-1\right)g\left(R_f,R_{env},\Delta\right)}\right\}^{-1}$$

$$d = D_l / V_{tip}\,, \quad f(R_{env},\Delta) = \frac{\left[(R_{env}+\Delta)^2-(R_{env})^2\right]}{2}, \quad g\left(R_f,R_{env},\Delta\right) = \frac{\left[\left(R_f\right)^3-(R_{env}+\Delta)^3\right]}{[3(R_{env}+\Delta)]}$$

$$\Delta = \frac{2R_{env}}{Sh}, \qquad Sh = \frac{2}{3(1-g_{env})} Sc^{\frac{1}{3}} Re^{n(Re)}$$

$$n(Re) = \frac{2Re^{0.28}+4.65}{3(Re^{0.28}+4.65)}, \; Re = \frac{\rho_l(1-g_s)(2R_s)}{\mu_l}\left|\langle \vec{v}_s \rangle^s - \langle \vec{v}_l \rangle^l\right|, \; Sc = \frac{\mu_l}{\rho_l D_l}$$

Phase Diagram

$$C_s^* = k_p C_l^*$$

As mentioned before, the entire mathematical framework is written for binary alloys. It is possible to extend this methodology to multicomponent alloys as shown by Rappaz and Boettinger [96].

2.3. Macroscopic Momentum Transport

In this section we discuss the macroscopic transport or more specifically the momentum equation modelling. Here also we split our discussion into two-phase and three-phase (simplified) models.

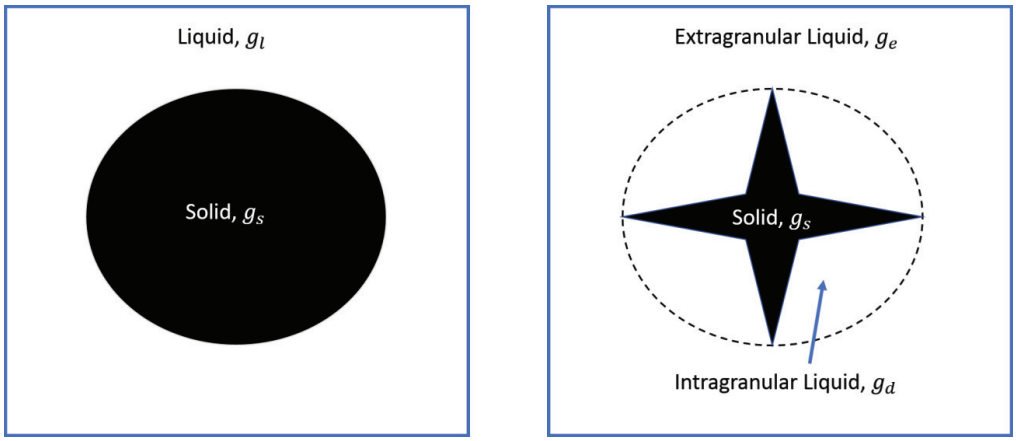

a) b)

Fig 2-3 Equiaxed grain morphology, a) two-phase globular grain and b) three-phase dendritic grain

2.3.1. Two-Phase Transport

We solve the liquid and solid momentum equation separately and they are given in Eq. (2-59) and Eq. (2-60)

$$\frac{\partial}{\partial t}\left(\rho_l g_l \langle\vec{v}_l\rangle^l\right) + \nabla\cdot\left(\rho_l g_l \langle\vec{v}_l\rangle^l \langle\vec{v}_l\rangle^l\right) = -g_l\nabla p_l + \nabla\cdot\left(g_l\mu_l\nabla\langle\vec{v}_l\rangle^l\right) + g_l\rho_l^b\vec{g} + M_{ls} \quad (2\text{-}59)$$

$$\frac{\partial}{\partial t}\left(\rho_s g_s \langle\vec{v}_s\rangle^s\right) + \nabla\cdot\left(\rho_s g_s \langle\vec{v}_s\rangle^s \langle\vec{v}_s\rangle^s\right) = -g_s\nabla p_l + \nabla\cdot\left(g_s\mu_s\nabla\langle\vec{v}_s\rangle^s\right) + g_s\rho_s^b\vec{g} - M_{ls} \quad (2\text{-}60)$$

Where ρ_k^b, $\vec{g}$ and M_{ls} are the buoyancy density for phase *k*, acceleration due to gravity and source term to model drag force respectively. Before we move to the description of the source term, we can simplify Eq. (2-60) based on the previously established theory [97] where we can ignore the effects of inertial and viscous forces. This simplifies Eq. (2-60) to Eq. (2-61).

$$0 = -g_s\nabla p_l + g_s\rho_s^b\vec{g} - M_{ls} \quad (2\text{-}61)$$

Eq. (2-61) has reduced into an algebraic equation and by modelling the source term M_{ls}, we can arrive at the explicit expression for solid velocity. The globular morphology is illustrated in Fig 2-3a, where the spherical solid phase is surrounded by liquid phase. Based on this we can define two regions of solid motion demarcated by the packing fraction (g_{pack}). In the first region, called slurry, the solid fraction is lower than the packing fraction and the solid is free to move. In the second region, called packed region, the solid fraction is higher than the packing fraction and the grains form a rigid porous network. The porous matrix is assumed to move with the casting velocity. We resolve the source term M_{ls} depending on the flow regime as shown in Eq. (2-62). For solid fraction lower than packing fraction, we model using

the interfacial drag term. When solid fraction exceeds the packing fraction, the drag is now modelled by a Darcy term.

$$M_{ls} = \begin{cases} \dfrac{3 g_s C_D \mu_l Re}{4(2R_s)^2(1-g_s)}\left(\langle \vec{v}_s \rangle^s - \langle \vec{v}_l \rangle^l\right) & g_s < g_{pack} \\ \dfrac{g_l^2 \mu_l}{K}\left(\langle \vec{v}_s \rangle^s - \langle \vec{v}_l \rangle^l\right), K = \dfrac{{l_{KC}}^2}{180}\dfrac{{g_l}^3}{(1-g_l)^2} & g_s > g_{pack} \end{cases} \tag{2-62}$$

Where C_D, μ_l, Re, R_s, K and l_{KC} are the drag-coefficient for spherical particles taken from Agarwal and O'Neil [98], liquid viscosity, particle Reynolds number, radius of the grain, permeability calculated using Kozeny-Carman relation and characteristic length of the porous media. By using the first condition in Eq. (2-62) and substituting in Eq. (2-61) we obtain the expression for solid velocity.

$$\langle \vec{v}_s \rangle^s = \langle \vec{v}_l \rangle^l + \frac{4(2R_s)^2(1-g_s)}{3 C_D \mu_l Re}\left(-\nabla p_l + \rho_s^b \vec{g}\right) \tag{2-63}$$

But the above equation is valid only in the slurry region and we need an additional equation to explicitly impose the solid velocity to casting velocity when the grains have packed, given by Eq. (2-64).

$$\langle \vec{v}_s \rangle^s = \vec{V}_{cast} \tag{2-64}$$

2.3.2. Simplified Three-Phase Transport

In the simplified three-phase model, we have assumed that the intrinsic velocities of extragranular and intragranular liquid is the same as the averaged liquid velocity (Ref Eq.(2-54)). This assumption reduces the macroscopic transport to two-phase transport model with a liquid and solid momentum equation. But at the microscopic level, the morphology influences the drag model and this needs to be accounted for in its calculation. Morphology of the equiaxed grain can be defined by introducing the internal solid fraction (g_i). It is given by Eq. (2-65). As the internal fraction approaches 1, the grains are globulitic (globular for the value 1) and as the internal solid fraction approaches 0, the grains are more dendritic.

$$g_i = \frac{g_s}{g_s + g_d} = \frac{g_s}{g_{env}} \tag{2-65}$$

Now we redefine the slurry and packed regions by considering the envelope fraction instead of solid fraction, which was the case in two-phase transport model. The new equation for modelling the source term in momentum equation is given by Eq. (2-66). Comparing with Eq. (2-62), we can see that the solid fraction is replaced by an envelope fraction and the radius of the solid grain is replaced by the radius of the envelope (R_{env}), all marked in red.

$$M_{ls} = \begin{cases} \dfrac{3g_{env}C_D\mu_l Re}{4(2R_{env})^2(1-g_{env})}\left(\langle\vec{v}_s\rangle^s - \langle\vec{v}_l\rangle^l\right) & g_{env} < g_{pack} \\ \dfrac{g_l^2\mu_l}{K}\left(\langle\vec{v}_s\rangle^s - \langle\vec{v}_l\rangle^l\right), K = \dfrac{{l_{KC}}^2}{180}\dfrac{{g_l}^3}{(1-g_l)^2} & g_{env} > g_{pack} \end{cases} \quad (2\text{-}66)$$

By using the above relations, we obtain the new expression of solid velocity for a dendritic grain and is given in Eq. (2-67). Here also we replace solid fraction with envelope fraction and we end up with an additional term – internal solid fraction (g_i), all marked again in red. This way, we can incorporate the morphology information in the calculation of solid velocity. It should be noted that the liquid momentum equation does not change, and we use the same expression given in Eq. (2-59).

$$\langle\vec{v}_s\rangle^s = \langle\vec{v}_l\rangle^l + \frac{4(2R_s)^2(1-g_{env})g_i}{3C_D\mu_l Re}\left(-\nabla p_l + \rho_s^b\vec{g}\right) \quad (2\text{-}67)$$

3. Summary of Publications

This chapter provides a brief summary of the published/submitted papers. In total, six papers are presented, and the most important results are discussed.

PAPER I
INVESTIGATION OF MACROSEGREGATION FORMATION IN ALUMINIUM DC CASTING FOR DIFFERENT ALLOY SYSTEMS

In DC casting of aluminium, many types of alloys are used. The structural properties, especially the strength, are improved by using these alloys. Macrosegregation indicates the non-uniformity of these alloy elements. Hence, the first step in improving the understanding of macrosegregation formation involves the investigation of the influence of alloy element. To conduct this study, three different binary alloys are chosen: Al-4.5wt%Mg, Al-4.5wt%Cu and Al-8.375wt%Zn. A two-phase multiscale solidification model is employed, and numerical simulations are performed using a simplified 2D sheet ingot geometry. The model accounts for globular grain motion, thermal-solutal convection and shrinkage induced flow and the resulting flow patterns are illustrated in Fig 3-1. The flow pattern for grain motion and shrinkage induced flow individually is the same for all the binary alloys considered. The grains tend to settle along the mushy zone, towards the center of the ingot. Shrinkage flow acts in deeper parts of mushy zone with a diverging and converging flow pattern towards the center and surface of the ingot respectively. Instead, thermal-solutal convection can result in complicated flow pattern depending on the alloy. Thermal convection individually results in clockwise flow pattern as heavy cooled liquid settles down along the inclined mushy zone. Solutal convection depends on the weight of the solute element. Cu and Zn are heavier than Al. They tend to follow a clockwise pattern, settling down along the mushy zone. Mg on the other hand is lighter than Al. It tends to float and consequently, causes an anticlockwise flow pattern. For Cu and Zn, thermal and solutal convection complement each other and result in a strong, clockwise convection loop. For Mg, the thermal and solutal convection compete with each other and result in breaking up of flow flops: a clockwise thermal loop and an anticlockwise solutal loop, as can be seen from Fig 3-1.

Studying these transport mechanisms individually and in combined form provided an insight into the macrosegregation formation, especially at the center of the ingot. For Al-Cu and Al-Zn, globular grain motion and thermal-solutal convection act towards the center of the ingot. This results in reduced relative velocities between the solid grain and liquid. Consequently, macrosegregation formation is almost non-existent at the center of the ingot. But when shrinkage induced flow is added, it results in negative segregation at the center of the ingot, typically observed in experimental results. For Al-Mg, grain motion and thermal-solutal convection in combined form results in negative segregation at the center of the ingot. Due to the weak convection flow, the relative velocities between solid grains and liquid is not entirely reduced, leading to negative segregation at the center of the ingot. Shrinkage induced flow acts in addition to grain motion, which further depletes solute element.

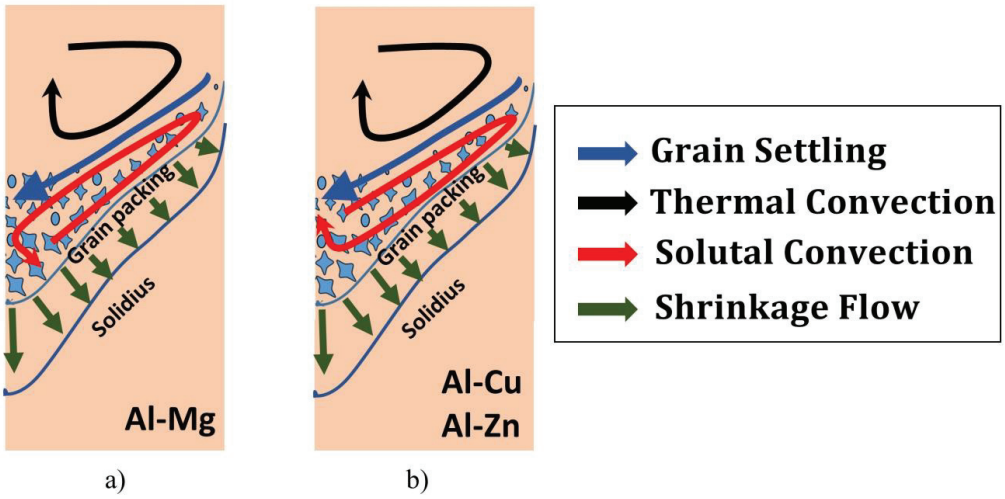

Fig 3-1 Illustration of various transport mechanisms in DC casting for a) Al-Mg system and b) Al-Cu and Al-Zn system

All the binary alloy systems showed negative segregation towards the center of the ingot. But transport mechanisms predominantly responsible for this negative segregation depended on the type of the alloy- shrinkage induced flow for Al-Cu and Al-Zn system and shrinkage induced flow in combination with grain motion for Al-Mg system.

Influence of Packing Fraction

As mentioned in the literature review, the value of packing fraction is ambiguous and it can influence grain settling and eventually macrosegregation formation. In this and the rest of papers, a packing fraction of 0.3 is assumed. However, it is important to understand the influence of packing fraction on macrosegregation formation. This aspect has been investigated as a part of this thesis but has not been included in any papers. Hence, the discussion is presented here.

Al-4.5wt%Mg binary alloy is considered with only globular grain motion as the active transport mechanism. Three different packing fraction are chosen: 0.1, 0.3, 0.45. The results are presented in Fig 3-2. An increase in packing fraction leads to intensification of the negative segregation towards the center. This is due to the extensive solute lean settling of globular grains. This settling expulses solute rich liquid upward and settles in the mid-section. The enhanced settling correspondingly enhances the mid-section positive segregation. Even though packing fraction increases negative segregation at center and positive mid-section segregation at the center, the increase is not substantial at higher packing fractions. The liquid flow pattern, however, remains unchanged in all the cases.

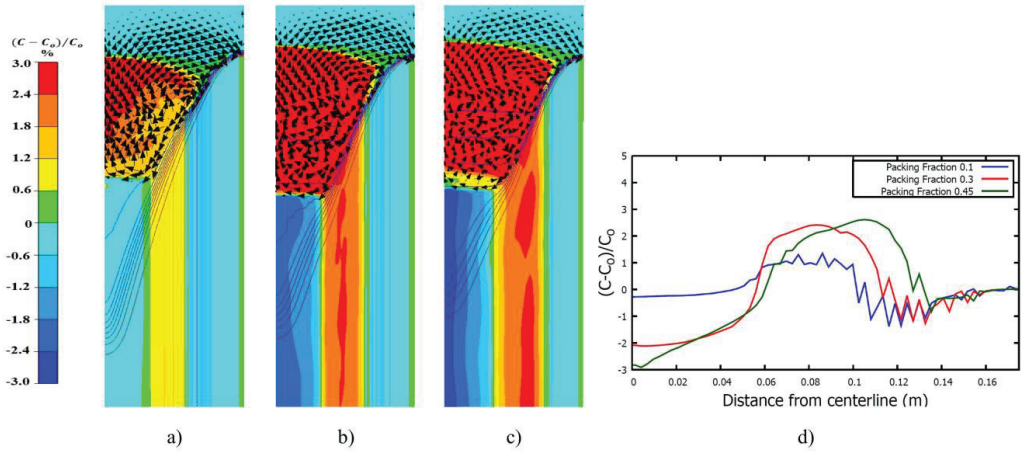

Fig 3-2 Relative macrosegregation contours over plotted with relative liquid velocity vectors for Al-4.5wt%Mg for packing fraction a) 0.1, b) 0.3 and c) 0.45. Relative macrosegregation profiles along the ingot thickness are plotted for the same cases are plotted in d)

Paper II

3D MACROSEGREGATION MODELLING OF DC CASTING OF ALUMINIUM ALLOY AND ITS COMPARISON WITH 2D MODEL AND EXPERIMENT

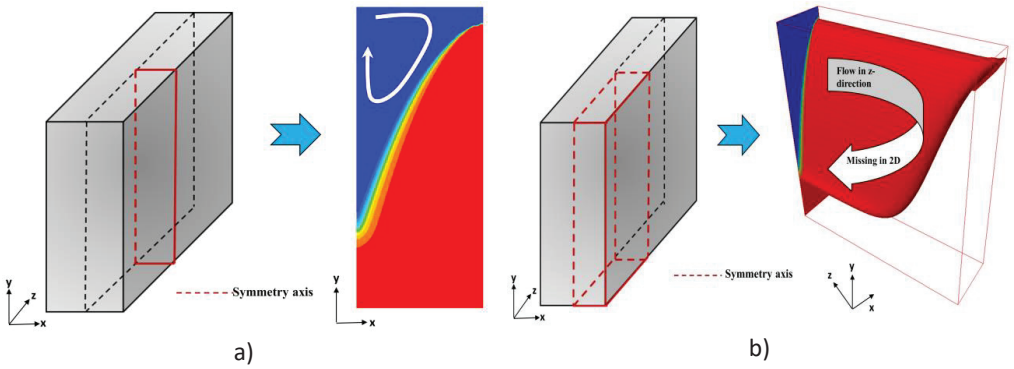

Fig 3-3 Illustration of simplification of process domain of sheet ingot in a) 2D modelling and b) 3D modelling

Sheet ingots have an asymmetric geometry and its simplification into a 2D model, as has been done previously and in *paper I,* can result in an unrealistic description of flow field. This is better illustrated in

Fig 3-3. In Fig 3-3a, the simplification of the 3D ingot (left) into a 2D ingot (right) is shown. A 2D plane is taken from the geometric center of the ingot, marked in red. The dotted line indicates symmetry axes. The resulting flow resolution is only in 2 dimensions (x-y plane), indicated by the white arrow. This approach is used in *paper I.* A more accurate modelling of the flow is possible by conducting 3D simulations by considering a quarter of the ingot, shown in Fig 3-3b. Instead of symmetry axis, symmetry planes are formed by combining the red dotted symmetry lines. The flow along the ingot width (z-direction), which was ignored in 2D simulations, is accounted for by this approach. This provides a better opportunity to study flow pattern in sheet ingots, thereby providing an assessment of the influence of 3D space on macrosegregation formation.

In the current paper, the modelling work is based on the EMPACT project[23–25] where experimental data along the x-z plane and thickness of the ingot are reported. The experimental case cast AA5182 alloy and combo bag inlet setup was used. Grain refiners were used and the reported grain structure was globulitic. This observation allows the usage of two-phase globular grain growth model in simulations. The modelling in 3D had several simplifications as it was the first attempt to compare 3D simulations with experiments. AA5182 alloy was modelled as a binary Al-4.06wt%Mg alloy as magnesium is the major alloy element and has a dominant effect on solidification process and density variations. The inlet combo bag setup was simplified with an open inlet. Simulation runs were conducted to include all the transport mechanisms: solidification shrinkage induced flow, thermal-solutal convection and globular grain motion. Al-4.06wt%Mg has a very thin mushy zone and a coarse mesh was used to keep the computational times within acceptable limits. Due to these factors, a finer resolution of the mushy zone was beyond the scope of this work. Grain motion reduces the thickness of the inclined mushy zone towards the surface of the ingot. As a result, the deeper parts of mushy zone in this region are not adequately resolved where shrinkage induced flow is active. These factors ultimately resulted in divergence. To avoid this problem, two cases were conducted. One case coupled grain motion and thermal-solutal convection. In the other case, only shrinkage induced flow was considered. This decomposition of transport mechanisms would not hinder the analysis as grain motion and thermal-solutal convection are active in the slurry region ($0.0<g_s<g_{pack}$) and shrinkage induced flow is dominant in the packed region ($g_s > g_{pack}$). Macrosegregation contour maps from the model on the x-z plane were used to compare with the experimental contour maps. Slices along the symmetry plane were used to obtain macrosegregation profiles along the ingot thickness and were used to compare with the experimental profiles. These results were also compared with 2D sheet ingot simulations.

Along the ingot thickness, both 3D and 2D simulations showed similar macrosegregation profiles. The influence of ingot width was considered minimum as the symmetry plane on which data was compared was far away from the cooling surface. One discrepancy is the simplification of the inlet. The combo bag set up can create complex 3D flow which might modify macrosegregation. Comparison with experimental results yielded only qualitative agreement as the extent of the negative segregation at the center of the ingot was overpredicted by the models. Similar behavior was observed when macrosegregation maps along x-z plane were compared between model and experiment. However, the presence of a band of negative segregation in the center along the x-z plane in experiment could be explained by grain motion in simulation. In spite of several simplifications, it was possible to qualitatively

compare experimental macrosegregation contours in sheet ingots using fully realized 3D simulation. Finally, solute accumulation in this 3D ingot simulation was similar to the solute accumulation in simulation cases in *paper I* where Mg was the alloy element. Mg was found to be floating near the inlet due to it being lighter than Al.

Paper III
A SIMPLIFIED THREE-PHASE MODEL OF EQUIAXED SOLIDIFICATION FOR THE PREDICTION OF MICROSTRUCTURE AND MACROSEGREGATION IN CASTINGS

Description of grain morphology forms an integral part in understanding the macrosegregation formation. It directly affects the settling of grains, interaction with the liquid melt and lastly, macrosegregation formation. Assumption of globular grains might result in a simple numerical implementation but will eventually lead to incorrect macrosegregation predictions. There is always a need for an accurate modelling of grain morphology by accounting for the complex morphology. This is possible by introducing an additional phase, resulting in three phases. The three-phase grain growth model consists of solid phase, intragranular and extragranular liquid phase. In contrast, a two-phase grain growth model consists of only solid and liquid phase. Due to the introduction of an additional phase in the three-phase model, it results in 5 couple transport equations to describe the grain growth: for envelope volume, mass and concentrations for solid and intragranular liquid. This causes considerable complexities in the numerical implementation. To avoid this problem, a simplified three-phase grain growth model is proposed in this paper. It reduces the number of coupled transport equations to 3: for envelope volume, solid mass and solid concentration. This simplified three-phase model is then compared with the full three-phase model to show the formers viability. The simplified model accurately predicts the recalescence behavior which forms an integral step for coupling with the nucleation models. The model predicts more dendritic grain morphologies than the full model. But the morphology transition is captured rather well.

This model is then verified by applying it to an industrial sized DC cast ingot, accounting for grain motion, thermo-solutal convection and shrinkage induced flow. It is shown that the grain morphology has direct impact on macrosegregation formation. At higher grain density, it is also shown that the grains approach globular morphology, similar to other experimental [24] and numerical observations [69].

Paper IV
APPLICATION OF AN EQUIAXED GRAIN GROWTH AND TRANSPORT MODEL TO STUDY MACROSEGREGATION IN A DC CASTING EXPERIMENT

To build confidence over the simplified three-phase model proposed in *paper III*, the model predictions of macrosegregation and grain structure need to be validated against experimental results. This is done in this paper and experimental data published by Zhang et al. [30,31] were taken as the reference. Two types of inlet melt feeding scheme were used in casting AA7050 billets. In the first type, melt was distributed through four branches. In the second type, melt was directed to the center of the billet in the form of a vertical jet.

For the first type of inlet, the process model was simplified with an inlet and distributor setup. The macrosegregation profiles from the model showed a very good comparison with experimental profiles when the morphology of the equiaxed grains was accounted for. When the grains are assumed to be spherical, over prediction of negative segregation at the center and incorrect prediction of macrosegregation in other parts of the billet was observed. This observation further strengthened the need for an accurate morphology description. The grain structure prediction was of the similar order observed in the experiments. But the variation of grain size across the cross-section of the billet, observed in the experiments, was not observed in model predictions.

Using the second type of inlet, reasonable agreement was observed between macrosegregation profiles using experiments and model predictions accounting for grain morphology. Similar to the previous inlet case, imposing globular morphology resulting in inaccurate macrosegregation prediction. Grain structure prediction in this case was also of the similar order observed in experiments.

Some important observations in this validation study are:

- Morphology prediction and its subsequent effect on macrosegregation formation is accurately described by the simplified three-phase model.
- Using two types of inlets, it was shown experimentally that the macrosegregation can be modified. With model predictions from two inlets showing good comparison with experimental data, we can conclude that the model is sensitive not only to grain morphology but also to the type of inlet mechanism.
- The model also predicts the resuspension of equiaxed grains (both globular and dendritic) using a vertical inlet jet.

Based on this validation study, the confidence in the simplified three-phase model is attained. This helps in conducting further case studies and comparison studies with experimental data, described in the next papers.

Paper V
IMPACT OF INLET FLOW ON MACROSEGREGATION FORMATION ACCOUNTING FOR GRAIN MOTION AND MORPHOLOGY EVOLUTION IN DC CASTING OF ALUMINIUM

One of the main causes of negative segregation observed at the center of the ingot/billet in DC casting process is due to the presence of solute lean grains. They usually nucleate along the inclined mushy zone and travel towards the center of the domain. This settling behavior, if restricted, could potentially eliminate (or reduce) negative segregation at the center of the cast product. Recent experimental work [33] strengthened this idea where the introduction of inlet jet resulted in grain resuspension and eliminated negative segregation at the center of the ingot. Indeed, this vertical jet should not be strong as it can wash away the solute elements which can prove to be counter-productive. This research introduced a methodology to optimize macrosegregation formation.

This forms the basis of first application of the three-phase model to understand macrosegregation formation. Numerical test cases are conducted on axis symmetric billets of 315 mm diameter, cast with

AA7050 alloy. The inlet flow is controlled by modifying the inlet radius. Several cases are conducted by solving for dendritic morphology and imposing globular morphology. It is established that, by using the numerical model, macrosegregation formation can be modified significantly by modifying the inlet flow and accounting for grain morphology. Grain resuspension of both globular and dendritic grains was observed for inlet with strong jet. For relatively weaker inlet jets, only dendritic grains were resuspended whereas the globular grains managed to overcome the inlet jet to settle towards the center of the billet. This provided the first insight into the link between inlet flow and morphology.

Modification of macrosegregation, which was the goal of this work, was achieved. Optimization of macrosegregation was not possible. One of the main reasons is the narrow operating range of the inlet flow (10mm-15mm) for the billet radius of 157.5mm. This limited the jet intensity at which grains could be resuspended.

Paper VI

3D NUMERICAL ANALYSIS OF MACROSEGREGATION FORMATION IN DC CASTING OF ALUMINIUM ALLOYS ACCOUNTING FOR INLET FLOW AND GRAIN MORPHOLOGY AND TRANSPORT

In this paper, the study conducted in *paper V* is extended to sheet ingots. A sheet ingot of 350mm thickness and 2600mm width with Al-8.375wt%Zn binary alloy is chosen for this study. Numerical resolution of the mushy zone is an important ingredient in accurate resolution of transport mechanisms. However, the simulation times for 3D simulation with mesh refinement can take prohibitively long time. To avoid this problem, a relatively thin ingot with a thick mushy zone is considered. Two types of inlet mechanisms are considered – a simplified open inlet where liquid metal is assumed to enter the domain from the top surface and an inlet with vertical jet where the liquid metal enters through an orifice of 30mmx30mm at the center of the ingot. For each inlet, we impose globular and solve for dendritic morphology. A total of four cases are discussed.

The macrosegregation contours on the horizontal x-z plane and profiles along the thickness (x-direction) are compared. By varying the inlet flow and accounting for grain morphology, modification of macrosegregation is shown possible. This is evident with all the four cases showing macrosegregation pattern different from each other. The grain sedimentation is altered depending on the choice of inlet flow. For simplified open inlet, a wide region of grain sedimentation along the ingot width was observed. But with an inlet jet, the grain sedimentation was pushed away from the center of the ingot. All these factors modified macrosegregation. Similar flow behavior was observed for both globular and dendritic grains. But the final macrosegregation pattern was different for the two morphologies because dendritic grains carry less solute depleted solid than globular grains. As for the work conducted in *paper V,* macrosegregation could be modified significantly by accounting for inlet flow and morphology of the grains in sheet ingot. With 3D simulations, flow visualization of equiaxed grain sedimentation and its interaction with inlet flow could be obtained. However, it should be noted that this is a numerical study.

4. Conclusions and Future Work

Macrosegregation formation in DC casting of aluminium alloys is a multiscale solidification problem. Several aspects, ranging from microscopic growth to macroscopic transport, leading to macrosegregation formation have been studied in this work under a single framework. This framework also provided an opportunity to transition from 2D to 3D sheet ingot modelling. A previously published two-phase volume averaged solidification model and a simplified three-phase volume averaged solidification model, developed in this work, were used to assess various mechanisms.

The impact of alloy element on macrosegregation formation in binary alloy systems has been assessed by considering Al-4.5wt%Mg, Al-4.5wt%Cu and Al- 8.375wt%Zn. Mg is lighter than Al while Cu and Zn are heavier than Al. Thermo-solutal convection for Al-Mg was weak due to light Mg competing with the heavy cooled liquid. Solutal gradient was in the opposite direction of thermal gradient. On the other hand, thermo-solutal convection for other two alloys was strong due to co-operating thermal and solutal gradients. This difference leads to different transport phenomena contributing to negative segregation at the center of the ingot. Shrinkage-induced flow and grain motion together contribute to negative segregation in the center for the Al-Mg system. For Al-Cu and Al-Zn, it is mainly due to shrinkage-induced flow as the impact of grain motion negative segregation at the center of the ingot is reduced by cooperating thermal and solutal convection. Nonetheless, the final macrosegregation pattern was similar for all binary alloys considered in this study and in each case, grains were observed to settle in the center of the ingot. This work was done using a two-phase globular grain growth model.

Macrosegregation formation in AA5182 sheet ingots was investigated to assess the influence of 3D ingot geometry on macrosegregation formation. Experimental data for this case is available from the EMPACT project. Both 3D and 2D simulations were conducted and compared with experimental results. Combo bag inlet setup has been used in the experiment but was simplified in the simulations by assuming that the liquid metal enters the domain from the top. It was shown that for this open inlet, 2D and 3D (in the center) simulations show similar macrosegregation pattern along ingot thickness and have a good qualitative comparison with experiments. Horizontal macrosegregation predictions (possible only in 3D simulations) also had a qualitative comparison with experiments. A band of negative segregation in the ingot center was observed in the experiment and simulation. Nucleation of equiaxed grains occurs along the inclined mushy zone and they sediment towards the center of the ingot due to buoyancy effects. The presence of these solute lean grains resulted in a band of negative segregation. The intensity of negative and positive segregation in the center and mid-section of the ingot, however, were under-predicted by the simulations.

A simplified three-phase grain growth model is proposed and the model is a novel approach as it solves for three-phase grain growth kinetics, coupled with two-phase macroscopic transport. This allows a simplified implementation in spite of solving for the complex morphology of the equiaxed grain. Validation with a full three-phase model indicated reasonable correlation but the simplified model was

predicting a more dendritic structure. The model is further validated with experimental macrosegregation profiles for AA7050 alloy in an axis symmetric billet. A good comparison between experiment and simulation was observed, especially in the center of the billet, when the dendritic morphology was accounted for. This emphasized the presence of equiaxed grains at the billet center and the influence of grain morphology on macrosegregation formation. The grain structure prediction was in the same order as in the experimental observations.

The presence of equiaxed grains at the center of the ingot is usually attributed to negative segregation. This was the basis of the work done by Wagstaff and Allanore [91], where an inlet jet was introduced to resuspend the equiaxed grains and modify macrosegregation formation and to an extent eliminate the negative segregation. In this work, the simplified three-phase model is used to study macrosegregation modification with an inlet jet in both axis symmetric billets and sheet ingots. Axis symmetric billets, even though have 2D profile, mimic 3D structure due to the boundary conditions. Sheet ingots on the other hand have an anti-symmetric geometry and they are solved in 3D in this work. In the billet cases an AA7050 alloy is studied and in the sheet ingot cases an Al-8.375wt%Zn is studied. Macrosegregation was modified by resuspending and recirculation of equiaxed grains with the introducing an inlet jet. The extent of modification also depended on the grain morphology and the grain interaction with inlet melt. Numerical analysis also indicated the relative ease with which dendritic grains could be resuspended.

The framework developed in this work makes significant progress in understanding macrosegregation formation and modification: considering the interaction between microstructure and macroscopic transport and inlet flow. Future work should focus on extending this framework to include, but not restricted to, several physical and numerical aspects mentioned below:

- The current simplified three-phase model employs simple constitutive models to predict grain growth in the presence of important solutal interactions between growing and moving grains. Significant research is being done and several advanced constitutive models have been proposed which could be integrated in the current model.
- As mentioned before, the inlet flow has been simplified by considering an open inlet. But in reality, a combo-bag setup is used. Modelling this inlet setup is important as it significantly modifies the flow pattern and might help us in answering the discrepancies in macrosegregation predictions when compared with experiment.
- One major problem in solving 3D cases is the accurate resolution of the mushy zone. The current study employed a uniform mesh and more accurate resolution of the mushy zone by refining the mesh globally can lead to prohibitive computational cost. This can be avoided by adaptive mesh refining. Mushy zone and the region around it can be adaptively refined. This does not significantly alter the computational cost but resolves the mush zone more accurately.

5. Bibliography

[1] Facts About Aluminum, (n.d.). http://www.livescience.com/28865-aluminum.html.

[2] Aluminum or Aluminium Facts, (n.d.). https://www.thoughtco.com/aluminum-or-aluminium-facts-606496.

[3] L.C. Nicolli, Mathematical Modelling of Macrosegregation Formation Caused by Deformation of the Mushy Zone, PhD Thesis, University of Oslo, 2005.

[4] How it's made, (n.d.). https://www.hydro.com/en/about-aluminium/how-its-made/.

[5] M.C. Fleming, Solidification Processing, McGraw-Hill, New York, 1974.

[6] J. Campbell, Castings, Butterworth Heinemann, 1991.

[7] J.A. Dantzing, M. Rappaz, Solidification, EPFL Press, 2009.

[8] W. Kurz, D.J. Fisher, Fundamentals of Solidification, Trans Tech Publications Ltd, Zurich, 1998.

[9] T. Jalanti, PhD Thesis, PhD Thesis, Ecole Polytechnique Fédérale de Lausanne, Laussanne, Switzerland, 2000.

[10] C.J. Vreeman, J.D. Schloz, M.J.M. Krane, Direct Chill Casting of Aluminum Alloys: Modeling and Experiments on Industrial Scale Ingots, J. Heat Transfer. 124 (2002) 947. doi:10.1115/1.1482089.

[11] M. Založnik, A. Kumar, H. Combeau, M. Bedel, P. Jarry, E. Waz, Influence of Transport Mechanisms on Macrosegregation Formation in Direct Chill Cast Industrial Scale Aluminum Alloy Ingots, Adv. Eng. Mater. 13 (2011) 570–580. doi:10.1002/adem.201000341.

[12] C.J. Vreeman, M.J.M. Krane, F.P. Incropera, The effect of free-floating dendrites and convection on macrosegregation in direct chill cast aluminum alloys Part I: Model Development, Int. J. Heat Mass Transf. 43 (2000) 677–686. doi:10.1016/S0017-9310(99)00175-1.

[13] A. V. Reddy, C. Beckermann, Simulation of the effects of thermosolutal convection, shrinkage induced flow and solid transport on macrosegregation and equaixed grain size distribution in a DC continous cast Al-Cu round ingot, Mater. Process. Comput. Age II. (1995) 89–102.

[14] I. Vušanović, M.J.M. Krane, Macrosegregation in horizontal direct chill casting of ternary Al alloys: Investigation of solid motion, IOP Conf. Ser. Mater. Sci. Eng. 27 (2011). doi:10.1088/1757-899X/27/1/012069.

[15] K.O. Tveito, A. Pakanati, M. M'Hamdi, H. Combeau, M. Založnik, A Simplified Three-Phase Model of Equiaxed Solidification for the Prediction of Microstructure and Macrosegregation in Castings, Metall. Mater. Trans. A. 49 (2018) 2778–2794. doi:10.1007/s11661-018-4632-1.

[16] A. Pakanati, K.O. Tveito, M. M'Hamdi, H. Combeau, M. Založnik, Impact of Inlet Flow on

Macrosegregation Formation Accounting for Grain Motion and Morphology Evolution in DC Casting of Aluminium, in: Martin O. Light Met. 2018. TMS 2018. Miner. Met. Mater. Ser. Springer, Cham, 2018: pp. 1089–1096. doi:10.1007/978-3-319-72284-9_142.

[17] A. Stangeland, A. Mo, Ø. Nielsen, D. Eskin, M. M'Hamdi, Development of thermal strain in the coherent mushy zone during solidification of aluminum alloys, Metall. Mater. Trans. A Phys. Metall. Mater. Sci. 35 A (2004) 2903–2915. doi:10.1007/s11661-004-0238-x.

[18] E. Haug, A. Mo, H.J. Thevik, Macrosegregation near a cast surface caused by exudation and solidification shrinkage, Int. J. Heat Mass Transf. 38 (1995) 1553–1563. doi:10.1016/0017-9310(94)00286-5.

[19] M. Založnik, Modelling of Macrosegregation in Direct Chill Casting, PhD Thesis, Graduate School University of Nova Gorica, 2006.

[20] H. Yu, D.A. Granger, Macrosegregation in aluminum alloy ingot cast by the semicontinuous direct chill method, in: Alum. Alloy. Their Phyiscal Mech. Prop., Sheffield, UK, 1986: pp. 17–29.

[21] R.C. Dorward, D.J. Beernsten, Effects of casting practice on macrosegregation and microstructure of 2024 alloy billet, in: Light Met., 1990: pp. 919–924.

[22] B. Gariepy, Y. Caron, Investigation in the effects of the casting parameters on the extent of centerline macrosegregation in DC cast sheet ingots, in: Light Met. 1991, 1991: pp. 961–971.

[23] A. Joly, G.U. Grün, D. Daloz, H. Combeau, G. Lesoult, Effect of Grain Refinement on Macrosegregation in Direct Chill Semi-Continuous Casting of Aluminium Sheet Ingot, Mater. Sci. Forum. 329–330 (2000) 111–120. doi:10.4028/www.scientific.net/MSF.329-330.111.

[24] G. Lesoult, V. Albert, B. Appolaire, H. Combeau, D. Daloz, A. Joly, C. Stomp, G.U. Grün, P. Jarry, Equi-axed growth and related segregations in cast metallic alloys, Sci. Technol. Adv. Mater. 2 (2001) 285–291. doi:10.1016/S1468-6996(01)00055-9.

[25] D. Daloz, H. Combeau, A. Joly, G. Lesoult, G.-U. Grün, P. Jarry, B. Commet, Étude Sur L'Origine De La Macroségrégation Centrale Dans La Coulée Semi-Continue D'Aluminium, Mater. 2002. (2002).

[26] M. Bedel, Étude de la formation des structures de solidification et des macroségrégations en coulée semi-continue d'aluminium, PhD Theses Université de Lorraine, Nancy,France, 2014.

[27] L. Zhang, D.G. Eskin, a. Miroux, T. Subroto, L. Katgerman, Influence of Melt Feeding Scheme and Casting Parameters During Direct-Chill Casting on Microstructure of an AA7050 Billet, Metall. Mater. Trans. B Process Metall. Mater. Process. Sci. 43 (2012) 1–9. doi:10.1007/s11663-012-9711-x.

[28] D.G. Eskin, J. Zuidema, V.I. Savran, L. Katgerman, Structure formation and macrosegregation under different process conditions during DC casting, Mater. Sci. Eng. A. 384 (2004) 232–244. doi:10.1016/j.msea.2004.05.066.

[29] D.G. Eskin, V.I. Savran, L. Katgerman, Effects of Melt Temperature and Casting Speed on the Structure and Defect Formation during Direct-Chill Casting of an Al-Cu Alloy, Metall. Mater. Trans. A. 36A (2005) 1965–1976. doi:10.1007/s11661-005-0132-1.

[30] L. Zhang, D.G. Eskin, A. Miroux, T. Subroto, L. Katgerman, Effect of Inlet Geometry on

Macrosegregation During the Direct Chill Casting of 7050 Alloy Billets: Experiments and Computer Modelling, IOP Conf. Ser. Mater. Sci. Eng. 33 (2012) 1–8. doi:10.1088/1757-899X/33/1/012019.
[31] L. Zhang, D.G. Eskin, A. Miroux, T. Subroto, L. Katgerman, Influence of Melt Feeding Scheme and Casting Parameters During Direct-Chill Casting on Microstructure of an AA7050 Billet, Metall. Mater. Trans. B Process Metall. Mater. Process. Sci. (2012) 1–9. doi:10.1007/s11663-012-9711-x.
[32] D.G. Eskin, Physical Metallurgy of Direct Chill Casting of Aluminum Alloys, Boca Raton: CRC Press, 2008.
[33] S.R. Wagstaff, A. Allanore, Minimization of Macrosegregation in DC Cast Ingots Through Jet Processing, Metall. Mater. Trans. B Process Metall. Mater. Process. Sci. 47 (2016) 3132–3138. doi:10.1007/s11663-016-0718-6.
[34] S.R. Wagstaff, A. Allanore, Centerline Depletion in Direct-Chill Cast Aluminum Alloys: The Avalanche Effect and Its Consequence for Turbulent Jet Casting, Metall. Mater. Trans. B Process Metall. Mater. Process. Sci. 47 (2016) 3139–3143. doi:10.1007/s11663-016-0756-0.
[35] S.R. Wagstaff, A. Allanore, Jet Mixing in Direct-Chill Casting of Aluminum: Crater Effects and its Consequence on Centerline Segregation, Metall. Mater. Trans. B Process Metall. Mater. Process. Sci. 48 (2017) 2114–2122. doi:10.1007/s11663-017-0986-9.
[36] M.C. Fleming, G.E. Nero, Macrosegregation: Part I, Trans. TMS-AIME. 239 (1967) 1449–1461.
[37] M.C. Fleming, R. Mehrabian, G.E. Nero, Macrosegregation: Part II, Trans. TMS-AIME. 242 (1967) 41–49.
[38] M.C. Fleming, G.E. Nero, Macrosegregation: Part III, Trans. TMS-AIME. 242 (1976) 50–55.
[39] R. Mehrabian, M. Keane, M.C. Flemings, Interdendritic fluid flow and macrosegregation; influence of gravity, Metall. Mater. Trans. 1 (1970) 1209–1220. doi:10.1007/BF02900233.
[40] D.R. Poirier, P.J. Nandapurkar, S. Ganesan, The energy and solute conservation equations for dendritic solidification, Metall. Trans. B. 22 (1991) 889–900. doi:10.1007/BF02651165.
[41] J. Wanqi, Further discussions on the solute redistribution during dendritic solidification of binary alloys, Metall. Mater. Trans. B. 25 (1994) 731–739. doi:10.1007/BF02655181.
[42] I. OHNAKA, Mathematical analysis of solute redistribution during solidification with diffusion in solid phase., Trans. Iron Steel Inst. Japan. 26 (1986) 1045–1051. doi:10.2355/isijinternational1966.26.1045.
[43] E.J. Pickering, Macrosegregation in Steel Ingots: The Applicability of Modelling and Characterisation Techniques, ISIJ Int. 53 (2013) 935–949. doi:10.2355/isijinternational.53.935.
[44] S.D. Ridder, S. Kou, R. Mehrabian, Effect of Fluid Flow on Macrosegregation in Axi-Symmetric Ingots, Metall. Trans. B. 12 (1981) 435–447.
[45] W. Liu, Modélisation par éléments finis des phénomènes thermomécaniques et de macroségrégation dans les procédés de solidification, PhD Thesis, Ecole des Mines de Paris, France, 2005.
[46] W.D. Bennon, F.P. Incropera, A continuum model for momentum, heat and species transport in binary solid-liquid phase change systems-I. Model formulation, Int. J. Heat

Mass Transf. 30 (1987) 2161–2170. doi:10.1016/0017-9310(87)90094-9.
[47] W.D. Bennon, F.P. Incropera, A continuum model for momentum, heat and species transport in binary solid-liquid phase change systems-II. Application to solidification in a rectangular cavity, Int. J. Heat Mass Transf. 30 (1987) 2171–2187. doi:10.1016/0017-9310(87)90095-0.
[48] W.D. Bennon, F.P. Incropera, The evolution of macrosegregation in statically cast binary ingots, Metall. Trans. B. 18 (1987) 611–616. doi:10.1007/BF02654275.
[49] V.R. Voller, C. Prakash, A fixed grid numerical modelling methodology for convection-diffusion mushy region phase-change problems, Int. J. Heat Mass Transf. 30 (1987) 1709–1719. doi:10.1016/0017-9310(87)90317-6.
[50] V.R. Voller, A.D. Brent, C. Prakash, The modelling of heat, mass and solute transport in solidification systems, Int. J. Heat Mass Transf. 32 (1989) 1719–1731. doi:10.1016/0017-9310(89)90054-9.
[51] J. Ni, F.P. Incropera, Extension of the continuum model for transport phenomena occurring during metal alloy solidification-I. The conservation equations, Int. J. Heat Mass Transf. 38 (1995) 1271–1284. doi:10.1016/0017-9310(94)00236-O.
[52] J. Ni, F.P. Incropera, Extension of the continuum model for transport phelnomena occurring during metal alloy solidification-II. Microscopic considerations, Int. J. Heat Mass Transf. 38 (1995) 1285–1296. doi:10.1016/0017-9310(94)00237-P.
[53] M.J.M. Krane, Macrosegregation development during solidification of a multicomponent alloy with free-floating solid particles, Appl. Math. Model. 28 (2004) 95–107. doi:10.1016/S0307-904X(03)00121-5.
[54] C. Beckermann, R. Viskanta, Mathematical Modeling of Transport Phenomena During Alloy Solidification, Appl. Mech. Rev. 46 (1993) 1–26. doi:10.1115/1.3120318.
[55] C. Beckermann, MELTING AND SOLIDIFICATION OF BINARY MIXTURES WITH DOUBLE-DIFFUSIVE CONVECTION IN THE MELT, PhD Thesis, Purdue University, West Lafayette (IN), USA, 1987.
[56] C. Beckermann, R. Viskanta, Double-diffusive convection during dendritic solidification of a binary mixture, Phys. Chem. Hydrodyn. 10 (1988) 195--213.
[57] J. Ni, C. Beckermann, A volume-averaged 2-phase model for transport phenomena during solidification, Metall. Trans. B---Process Metall. 22 (1991) 349–361.
[58] S. Ganesan, D.R. Poirier, Conservation of mass and momentum for the flow of interdendritic liquid during solidification, Metall. Trans. B. 21 (1990) 173–181. doi:10.1007/BF02658128.
[59] C.Y. Wang, C. Beckermann, A multiphase solute diffusion model for dendritic alloy solidification, Metall. Trans. A. 24 (1993) 2787–2802. doi:10.1007/BF02659502.
[60] C.Y. Wang, C. Beckermann, Equiaxed dentritic solidification with convection: Part I. multiscale/multiphase modeling, Metall. Mater. Trans. A. 27A (1996) 2754–2764.
[61] C.Y. Wang, C. Beckermann, Part II . Numerical Simulations for an AI-4 Wt Pct Cu Alloy, Metall. Mater. Trans. A. 27A (1996) 2765–2783.
[62] C. Beckermann, C.Y. Wang, Equiaxed dendritic solidification with convection: Part III. Comparisons with NH4Cl-H2O experiments, Metall. Mater. Trans. A. 27 (1996) 2784–2795. doi:10.1007/BF02652371.
[63] M.C. Schneider, C. Beckermann, Formation of macrosegregation by multicomponent

thermosolutal convection during the solidification of steel, Metall. Mater. Trans. A. 26 (1995) 2373–2388. doi:10.1007/BF02671251.
[64] A. Ludwig, M. Wu, Modeling of globular equiaxed solidification with a two-phase approach, Metall. Mater. Trans. A. 33 (2002) 3673–3683. doi:10.1007/s11661-002-0241-z.
[65] M. Wu, A. Ludwig, A. Buhrig-Polaczek, M. Fehlbier, P.R. Sahm, Influence of convection and grain movement on globular equiaxed solidification, Int. J. Heat Mass Transf. 46 (2003) 2819–2832. doi:10.1016/S0017-9310(03)00054-1.
[66] A. Ludwig, M. Wu, Modeling the columnar-to-equiaxed transition with a three-phase Eulerian approach, Mater. Sci. Eng. A. 413–414 (2005) 109–114. doi:10.1016/j.msea.2005.08.184.
[67] M. Wu, A. Ludwig, Using a three-phase deterministic model for the columnar-to-equiaxed transition, Metall. Mater. Trans. A Phys. Metall. Mater. Sci. 38 A (2007) 1465–1475. doi:10.1007/s11661-007-9175-9.
[68] H. Combeau, M. Založnik, S. Hans, P.E. Richy, Prediction of macrosegregation in steel ingots: Influence of the motion and the morphology of equiaxed grains, Metall. Mater. Trans. B Process Metall. Mater. Process. Sci. 40 (2009) 289–304. doi:10.1007/s11663-008-9178-y.
[69] M. Založnik, H. Combeau, The influence of the morphology evolution of free-floating equiaxed grains on the macrosegregation in a 3.3-ton steel ingot, Model. Cast. Weld. Adv. Solidif. Process. XII. (2009) 165–172.
[70] H. Combeau, A. Kumar, M. Založnik, Modeling of equiaxed grain evolution and macrosegregations development in Steel Ingots, Trans. Indian Inst. Met. 62 (2009) 285–290.
[71] M. Wu, A. Ludwig, Modeling equiaxed solidification with melt convection and grain sedimentation—I: Model description, Acta Mater. 57 (2009) 5621–5631. doi:10.1016/j.actamat.2009.07.067.
[72] M. Wu, A. Ludwig, Modeling equiaxed solidification with melt convection and grain sedimentation-II. Model verification, Acta Mater. 57 (2009) 5632–5644. doi:10.1016/j.actamat.2009.07.067.
[73] M. Wu, A. Fjeld, A. Ludwig, Modelling mixed columnar-equiaxed solidification with melt convection and grain sedimentation - Part I: Model description, Comput. Mater. Sci. 50 (2010) 32–42. doi:10.1016/j.commatsci.2010.07.005.
[74] M. Wu, A. Fjeld, A. Ludwig, Modelling mixed columnar-equiaxed solidification with melt convection and grain sedimentation – Part II: Illustrative modelling results and parameter studies, Comput. Mater. Sci. 50 (2010) 43–58. doi:10.1016/j.commatsci.2010.07.005.
[75] J. Li, M. Wu, A. Ludwig, A. Kharicha, Simulation of macrosegregation in a 2.45-ton steel ingot using a three-phase mixed columnar-equiaxed model, Int. J. Heat Mass Transf. 72 (2014) 668–679. doi:10.1016/j.ijheatmasstransfer.2013.08.079.
[76] M. Ahmadein, M. Wu, A. Ludwig, Analysis of macrosegregation formation and columnar-to-equiaxed transition during solidification of Al-4 wt.%Cu ingot using a 5-phase model, J. Cryst. Growth. 417 (2015) 65–74. doi:10.1016/j.jcrysgro.2014.07.039.
[77] K.O. Tveito, M. Bedel, M. Založnik, H. Combeau, M. M'Hamdi, a Kumar, P. Dutta, Numerical study of the impact of inoculant and grain transport on macrosegregation and

microstructure formation during solidification of an Al-22%Cu alloy, IOP Conf. Ser. Mater. Sci. Eng. 33 (2012) 012089. doi:10.1088/1757-899X/33/1/012089.
[78] M. Bedel, K.O. Tveito, M. Založnik, H. Combeau, M. M'Hamdi, A model study of the impact of the transport of inoculant particles on microstructure formation during solidification, Comput. Mater. Sci. 102 (2015) 95–109. doi:10.1016/j.commatsci.2015.01.028.
[79] M. Založnik, H. Combeau, An operator splitting scheme for coupling macroscopic transport and grain growth in a two-phase multiscale solidification model: Part I - Model and solution scheme, Comput. Mater. Sci. 48 (2010) 1–10. doi:10.1016/j.commatsci.2009.04.036.
[80] Y. Xu, Experimental and numerical modelling study on the nucleation and grain growth of inoculated aluminium alloys, PhD Thesis, Norwegian University of Science and Technology, Trondheim, Norway, 2017.
[81] S.. Flood, L. Katgerman, V.R. Voller, The calculation of macrosegregation and heat and fluid flow in DC casting of aluminium alloys, in: Model. Cast. Weld. Adv. Solidif. Process. V, Warrnedale (PA), USA, 1991: pp. 683–690.
[82] A. V. Reddy, N.C. Beckermann, Modeling of macrosegregation due to thermosolutal convection and contraction-driven flow in direct chill continuous casting of an Al-Cu round ingot, Metall. Mater. Trans. B. 28 (1997) 479–489. doi:10.1007/s11663-997-0115-2.
[83] C.J. Vreeman, F.P. Incropera, The effect of free-floating dendrites and convection on macrosegregation in direct chill cast aluminum alloys Part II: Predictions for Al-Cu and Al-Mg alloys, Int. J. Heat Mass Transf. 43 (2000) 687–704. doi:10.1016/S0017-9310(99)00175-1.
[84] T. Jalanti, M. Swierkosz, M. Gremaud, M. Rappaz, Modelling of macrosegregation in continuous casting of aluminium, DGM Conf. (2000) 1–7.
[85] M. Založnik, B. Šarler, Thermosolutal flow in metals and implications for DC casting, Model. Cast. Weld. Adv. Solidif. Process. XI. (2006) 243–250.
[86] M. Založnik, A. Kumar, H. Combeau, M. Bedel, P. Jarry, E. Waz, The Coupling of Macrosegregation With Grain Nucleation, Growth and Motion in DC Cast Aluminum Alloy Ingots, Essent. Readings Light Met. Vol. 3, Cast Shop Alum. Prod. (2013) 848–853. doi:10.1002/9781118647783.ch106.
[87] M. Bedel, L. Heyvaert, M. Založnik, H. Combeau, D. Daloz, G. Lesoult, Process-scale modelling of microstructure in direct chill casting of aluminium alloys, IOP Conf. Ser. Mater. Sci. Eng. 84 (2015). doi:10.1088/1757-899X/84/1/012100.
[88] B. Appolaire, H. Combeau, G. Lesoult, Modeling of equiaxed growth in multicomponent alloys accounting for convection and for the globular/dendritic morphological transition, Mater. Sci. Eng. A. 487 (2008) 33–45. doi:10.1016/j.msea.2007.11.030.
[89] J. Lipton, M.E. Glicksman, W. Kurz, Equiaxed dendrite growth in alloys at small supercooling, Metall. Trans. A. 18 (1987) 341–345. doi:10.1007/BF02825716.
[90] L. Heyvaert, M. Bedel, M. Založnik, H. Combeau, Modeling of the Coupling of Microstructure and Macrosegregation in a Direct Chill Cast Al-Cu Billet, Metall. Mater. Trans. A. 48 (2017) 4713–4734. doi:10.1007/s11661-017-4238-z.
[91] S.R. Wagstaff, A. Allanore, Modification of Macrosegregation Patterns in Rolling Slab

Ingots by Bulk Grain Migration, in: Williams E. Light Met. 2016, 2016: pp. 715–719. doi:10.1002/9781119274780.ch120.
[92] C. Beckermann, Modeling of macrosegregation: Past, present and future, Proc. Mert. C. Flemings Symp. Solidif. Mater. Process. (2000) 297–310.
[93] M. Rappaz, P. Thévoz, Solute diffusion model for equiaxed dendritic growth, Acta Metall. 35 (1987) 1487–1497. doi:10.1016/0001-6160(87)90094-0.
[94] M. Rappaz, P.H. Thévoz, Solute diffusion model for equiaxed dendritic growth: Analytical solution, Acta Metall. 35 (1987) 2929–2933. doi:10.1016/0001-6160(87)90292-6.
[95] J. Ni, C. Beckermann, Modeling of globulitic alloy solidification with convection, J. Mater. Process. Manuf. Sci. 2 (1993) 217–231.
[96] M. Rappaz, W.J. Boettinger, On dendritic solidification of multicomponent alloys with unequal liquid diffusion coefficients, Acta Mater. 47 (1999) 3205–3219. doi:10.1016/S1359-6454(99)00188-3.
[97] L. Heyvaert, Modélisation de la formation des structures et des microporosités durant la solidification d'alliages d'aluminium, PhD Thesis, Université de Lorraine, Nancy, France, 2015.
[98] P.K. Agarwal, B.K. O'Neill, Transport phenomena in multi-particle systems - I. Pressure drop and friction factors: Unifying the hydraulic-radius and submergedobject approaches, Chem. Eng. Sci. 43 (n.d.) 2487–2499.

Paper I

INVESTIGATION OF MACROSEGREGATION FORMATION IN ALUMINIUM DC CASTING FOR DIFFERENT ALLOY SYSTEMS

Akash Pakanati, Mohammed M'Hamdi, Hervé Combeau and Miha Založnik

Is not included due to copyright
available at https://doi.org/10.1007/s11661-018-4731-z

Paper II

3D MACROSEGREGATION MODELLING OF DC ASTING OF ALUMINIUM ALLOY AND ITS COMPARISON WITH 2D MODEL AND EXPERIMENT

Akash Pakanati, Mohammed M'Hamdi, Hervé Combeau and Miha Založnik

Paper III

A SIMPLIFIED THREE-PHASE MODEL OF EQUIAXED SOLIDIFICATION FOR THE PREDICTION OF MICROSTRUCTURE AND MACROSEGREGATION IN CASTINGS

Knut Omdal Tveito, Akash Pakanati, Mohammed M'Hamdi, Hervé Combeau and Miha Založnik

Paper IV

APPLICATION OF AN EQUIAXED GRAIN GROWTH AND TRANSPORT MODEL TO STUDY MACROSEGREGATION IN A DC CASTING EXPERIMENT

Akash Pakanati, Knut Omdal Tveito, Mohammed M'Hamdi, Hervé Combeau and Miha Založnik

APPLICATION OF AN EQUIAXED GRAIN GROWTH AND TRANSPORT MODEL TO STUDY MACROSEGREGATION IN A DC CASTING EXPERIMENT

Akash Pakanati[1], Knut Omdal Tveito[1], Mohammed M'Hamdi[1,2], Hervé Combeau[3], Miha Založnik[3]

[1] Dept. of Materials Technology, NTNU, N-7491 Trondheim, Norway
[2] SINTEF Materials and Chemistry, N-0314 Oslo, Norway
[3] Université de Lorraine, CNRS, Institut Jean Lamour – IJL, F-54000 Nancy, France

* Corresponding author: Mohammed M'Hamdi (Mohammed.Mhamdi@sintef.no)

Abstract

A simplified three-phase, multiscale macrosegregation model which describes the growth kinetics of equiaxed grains and the coupling between microstructure morphology and the macroscopic transport has been proposed previously. In this paper, the model is validated by comparing the numerical model predictions to experimental data from DC casting of an AA7050 alloy billet. The morphology of the equiaxed grains has an important influence on the macrosegregation and we show that the model predictions are accurate when the grain morphology is described correctly.

Keywords: Macrosegregation, Solidification, Equiaxed Grains, DC-Casting

1. Introduction

One of the main phenomena causing macrosegregation in direct-chill (DC) cast aluminium alloy products is the motion of free-floating equiaxed grains. The solute-lean grains settle towards the bottom of the solidification zone (mushy zone) and eject solute-rich liquid. This tends to cause negative macrosegregation in the vicinity of the centerline of the casting and positive macrosegregation elsewhere. The intensity of this effect on macrosegregation depends largely on the morphology of the equiaxed grains – dendritic or globular[1–4]. The grain morphology has an impact on the motion and the packing of free-floating equiaxed grains[5] as well as on the permeability of the packed grain layer. The development of the microstructure (grain size, morphology) is also strongly conditioned by macroscopic flow, which determines the transport of grains and of inoculant particles acting as nucleation sites throughout the casting[6].

Control of microstructure and macrosegregation in DC casting via process parameters, such as casting speed, grain refinement or melt feeding, require a detailed understanding of the involved physical mechanisms. Such understanding is still lacking and the support of modeling is vital to improve the control of the complex casting process. Volume-average multiscale and multiphase models that couple the description of the process-scale transport with detailed models of dendritic grain growth have been developed for around 30 years[3,7–13] and have been applied to other casting processes, mainly to ingot castings[14–17]. This type of modeling is much less developed for DC casting. Most DC casting models were based on simple solidification models and did not account for the description of nucleation and of grain growth kinetics[18–23]. Models that included grain growth kinetics did either not consider grain motion at all[1] or assumed a globular morphology for the free-floating grains[23,24]. Detailed models that focused on grain structure and morphology were not coupled with grain motion and macrosegregation[25]. Simulations of macrosegregation were thus limited to globular grains and could not correctly describe the influence of grain morphology.

Only recently a multiscale model of DC casting, sufficiently advanced to describe the morphology development during grain growth, fully coupled with grain motion, and macrosegregation, was developed and applied by Tveito et al.[3]. This three-phase volume-average [8] model accounts for solidification shrinkage, thermosolutal convection, grain transport, heat transfer, solute transport and equiaxed grain growth. In addition to these aspects, nucleation on grain refiners and strong coupling between nucleation, growth and transport of grain refiner particles, which are important in DC casting of Al alloys, are also accounted for in this model. The impact of morphology on macrosegregation formation in a DC cast ingot was shown qualitatively. This model was also successfully applied to analyze the influence of the flow and of grain refinement on grain size and morphology in a large sheet ingot[26,27] and in a cylindrical billet[4].

In this paper, we use the model of Tveito et al. to investigate the influence of melt feeding on the formation of macrosegregation and microstructure in AA7050 alloy billets. The study is based on experiments conducted by Zhang et al. [21,28]. We show that a good description of microstructure morphology is an important ingredient to accurately predict macrosegregation formation.

2. Numerical Model

The three-phase, multiscale numerical model of equiaxed solidification, proposed by Tveito et al.[3], is based on the volume-averaging approach of Wang and Beckermann[9] and employs the operator splitting algorithm proposed by Založnik and Combeau [29]. For a detailed description of the model the reader is referred to these papers. Only the main features are described here and the model equations are summarized in Table 1. The Euler-Euler volume averaged model has two parts – macroscopic transport and microscopic growth. The macroscopic transport accounts for solute and heat transfer coupled with liquid flow induced by solidification shrinkage and thermosolutal convection. The densities of liquid and solid are assumed to be constant but different and the Bousinessq approximation is used for the liquid density in the buoyancy term accounting for thermal and solutal effects. The volume occupied by a dendritic grain is given by the volume of its envelope. Two flow regimes are considered and the flow regime depends on the local volume fraction of the grain envelopes (g_{env}). For envelope fractions smaller than the packing fraction (g_{pack}, a model parameter) the solid (equiaxed) grains are freely floating. The interfacial drag term C_D in Equation (9) is modeled in the same manner as in Ref.[29] for spherical particles but by considering the envelope fraction instead of the solid fraction. For envelope fractions greater than the packing fraction, grains are assumed to form a rigid porous solid matrix moving with the casting velocity, $\vec{V}_{cast}$. The interfacial drag in the porous medium is modeled by a Darcy term, where the hydrodynamic permeability is calculated by the Kozeny Carman relation, using the characteristic size of the porous structure, l_{KC}.

The microscopic part is treated locally within each volume element. The model accounts for finite diffusion in both solid and liquid phases and local thermal equilibrium is assumed. Nucleation of grains is assumed to occur on grain-refiner (inoculant) particles. According to the athermal nucleation theory of Greer et. al[30], the critical undercooling for free growth of a grain on an inoculant particle of diameter d is given by $\Delta T_c = 4\Gamma_{GT}/d$ where Γ_{GT} is the Gibbs-Thompson coefficient. The number of activated particles then depends on the size distribution of the particle population, which can be represented by an exponential distribution density function This representation holds for the largest particles, which are activated at small undercoolings and therefore successful as nuclei. This size distribution is then discretized into *m* classes of inoculants. Each class *i* is represented by a volumetric population density, N_{nuc}^i, and a critical undercooling, ΔT_c^i . When the local undercooling reaches the critical undercooling of class *i*, its local inoculant density, N_{nuc}^i, is instantaneously added to the grain number density, N_g, and N_{nuc}^i becomes locally zero. The conservation equations for the density of each inoculant class and the grain number density are shown in Equations (10) and (11), respectively, where Φ^i represents the transfer of population density from inoculants to grains upon nucleation.

The diffusion-controlled growth of dendritic grains is described by a volume-averaged model that distinguishes three hydrodynamic phases: solid (g_s), intragranular liquid (g_d), and extragranular liquid (g_e)[31]. The sum of the volume fraction of the three phases should result in unity ($g_s + g_d + g_e = 1$). The distinction between the two liquid phases is made because the diffusion time in the intragranular liquid is governed by the secondary dendrite arm spacing (SDAS) and in the extragranular liquid by the distance between grains. The intragranular liquid is at thermodynamic equilibrium throughout the solidification because of the short diffusion time at the SDAS scale. The extragranular liquid remains undercooled and the undercooling depends on the solute diffusion from the intragranular into the extragranular liquid. The growth of the solid is governed by diffusion at the solid-intragranular liquid interface. The grain envelopes are assumed to be spheres growing with the speed of the primary dendrite tips. Their growth is given by a model of a hemispherical dendrite tip, which links the tip speed to the volume-averaged undercooling in the extragranular liquid. Since it distinguishes between the growth of the solid skeleton and of the grain envelope, the model gives a quantification of the grain morphology via the fraction of solid in the envelope – the internal solid fraction: $g_{intern} = g_s/g_{env}$. For $g_{intern} \ll 1$ the grains are considered to be dendritic, for $g_{intern} \approx 1$ they are globular.

The grain growth is described by the three phases microscopically. However, the macroscopic transport considers only two phases: the solid and the liquid phase. This is obtained by considering equal velocities of the intragranular and extragranular liquid phases and by combining their solute conservation equations. This approach, described in Ref[3], results in a single liquid phase leading to a two-phase macroscopic transport system.

Table 1: System of Equations

Macroscopic Conservation Equations

Averaged mass balance of liquid phase	$\frac{\partial}{\partial t}(\rho_l g_l) + \nabla.(\rho_l g_l \langle \vec{v}_l \rangle^l) = \Gamma^l$	(1)
Averaged mass balance of solid phase	$\frac{\partial}{\partial t}(\rho_s g_s) + \nabla.(\rho_s g_s \langle \vec{v}_s \rangle^s) = \Gamma^s$	(2)
Averaged solute balance of liquid phase for component i	$\frac{\partial}{\partial t}\left(\rho_l g_l \langle C_{i,l} \rangle^l\right) + \nabla.\left(\rho_l g_l \langle \vec{v}_l \rangle^l \langle C_{i,l} \rangle^l\right) = -\Gamma^s C_i^{*,l} + \frac{\rho_l S_v^{env} D_{i,l}}{\delta_i^{e-d}} \frac{g_l}{g_e}\left(C_i^{*,l} - \langle C_{i,l} \rangle^l\right)$	(3)
Averaged solute balance of solid phase for component i	$\frac{\partial}{\partial t}\left(\rho_s g_s \langle C_{i,s} \rangle^s\right) + \nabla.\left(\rho_s g_s \langle \vec{v}_s \rangle^s \langle C_{i,s} \rangle^s\right) = \Gamma^s C_i^{*,s-d} + \frac{\rho_s S_v^s D_{i,s}}{\delta_i^{s-d}}\left(C_i^{*,s-d} - \langle C_{i,s} \rangle^s\right)$	(4)
Averaged mixture enthalpy	$\frac{\partial}{\partial t}(\rho_m h_m) + \nabla.(\rho_s g_s \langle \vec{v}_s \rangle^s \langle h_s \rangle^s) + \nabla.(\rho_l g_l \langle \vec{v}_l \rangle^l \langle h_l \rangle^l) = \nabla.((g_l k_l + g_s k_s)\nabla T)$	(5)
Averaged envelope fraction	$\frac{\partial}{\partial t}(\rho_s g_{env}) + \nabla.(\rho_s g_{env} \langle \vec{v}_s \rangle^s) = \Gamma^{env}$	(6)
Averaged liquid momentum	$\frac{\partial}{\partial t}(\rho_l g_l \langle \vec{v}_l \rangle^l) + \nabla.(\rho_l g_l \langle \vec{v}_l \rangle^l \langle \vec{v}_l \rangle^l) = -g_l \nabla p_l + \nabla.(g_l \mu_l \nabla \langle \vec{v}_l \rangle^l) + g_l \rho_{l,b} \vec{g} + M_{ls}$	(7)
Averaged solid momentum	$0 = -g_s \nabla p_l + g_s \rho_{s,b} \vec{g} - M_{ls} \quad g_{env} < g_{pack}$ $\langle \vec{v}_s \rangle^s = \vec{V}_{cast} \quad g_{env} > g_{pack}$	(8)

Source term in momentum equation

$$M_{ls} = \begin{cases} \dfrac{3 g_{env} C_D \mu_l Re}{4(2R_{env})^2(1-g_{env})}(\langle \vec{v}_s \rangle^s - \langle \vec{v}_l \rangle^l) & g_{env} < g_{pack} \\ \dfrac{g_l^2 \mu_l}{K}(\langle \vec{v}_s \rangle^s - \langle \vec{v}_l \rangle^l), K = \dfrac{{l_{KC}}^2}{180}\dfrac{{g_l}^3}{(1-g_l)^2} & g_{env} > g_{pack} \end{cases} \quad (9)$$

Nucleation Modelling

Innoculant Motion

$$\frac{\partial}{\partial t}\left(N_{nuc}^i\right) + \nabla.\left(\langle \vec{v}_l \rangle^l N_{nuc}^i\right) = -\Phi^i \quad (10)$$

Grain Population Balance

$$\frac{\partial}{\partial t}\left(N_g\right) + \nabla.\left(\langle \vec{v}_s \rangle^s N_g\right) = \sum_{i=1}^{N_{nuc}^i} \Phi^i \quad (11)$$

Source term in nucleation modelling

$$\Phi^i = \begin{cases} N_{nuc}^i \partial(t), \Delta T < \Delta T_c^i \\ 0, \quad else \end{cases}, i = 1, \dots, m \quad (12)$$

Microscopic Conservation Equations

Mass balance at solid-liquid interface

$$\Gamma_l + \Gamma_s = 0 \quad (13)$$

Solute balance at solid-liquid interface

$$\Gamma^s\left(1-k_{p,i}\right)C_i^{*,l} = \frac{\rho_s S_v^s D_{i,s}}{\delta_i^{s-d}}\left(k_{p,i}C_i^{*,l} - \langle C_{i,s} \rangle^s\right) + \frac{\rho_l S_v^{env} D_{i,l}}{\delta_i^{e-d}}\frac{g_l}{g_e}\left(C_i^{*,l} - \langle C_{i,l} \rangle^l\right) \quad (14)$$

Growth rate of grain envelope. The tip velocity (V_{tip}) is computed using hemispherical tip model proposed by Rappaz and Boettinger[32]

$$\Gamma^{env} = \rho_l S_v^{env} V_{tip} \quad (15)$$

Diffusion lengths

$$\delta_i^{s-d} = \frac{R^{s,eq}}{5} \quad (16)$$

$$\delta_i^{e-d} = d_i\left\{\frac{d_i}{R^{env}} - \omega\right\}^{-1} \quad (17)$$

$$\omega = \frac{f(R^{env},\Delta_i) + g(R_f,R^{env},\Delta_i)}{d_i\left[R^{env} + d_i - (R^{env}+\Delta_i+d_i)e^{-\Delta_i/d_i}\right] - f(R^{env},\Delta_i) + (e^{-\Delta_i/d_i}-1)g(R_f,R^{env},\Delta_i)}$$

$$R_f = \left(\frac{3}{4\pi N_g}\right)^{1/3}, \quad R^{env} = R_f g_{env}^{1/3}, \quad R^{s,eq} = R_f g_s^{1/3},$$

$$S_v^{env} = 4\pi(R^{env})^2 N_g, \quad S_v^s = 4\pi(R^{s,eq})^2 N_g$$

$$d_i = D_{l,i}/V_{tip}, \; f(R_{env},\Delta_i) = \frac{[(R^{env}+\Delta_i)^2 - (R^{env})^2]}{},$$

$$g\left(R_f,R^{env},\Delta_i\right) = \frac{\left[\left(R_f\right)^3 - (R^{env}+\Delta_i)^3\right]^2}{[3(R^{env}+\Delta_i)]}, \Delta_i = \frac{2R^{env}}{Sh_i}$$

$$Sh_i = \frac{2}{3(1-g_{env})} Sc_i^{\frac{1}{3}} Re^{n(Re)}, \; Sc_i = \frac{\mu_l}{\rho_l D_{l,i}}, n(Re) = \frac{2Re^{0.28}+4.65}{3(Re^{0.28}+4.65)}$$

$$Re = \frac{\rho_l(1-g_{env})(2R^{env})}{\mu_l}\left|\langle \vec{v}_s \rangle^s - \langle \vec{v}_l \rangle^l\right|$$

Thermodynamic relations at solid-liquid interface	$C_i^{*,s-d} = k_{p,i} C_i^{*,l}$	(18)
	$T_{liq} = T_m + \sum_i m_{l,i} c_{l,i}^*$	(19)
	$\Delta T = T - T_m - \sum_i m_{l,i} c_{l,i}^*$	(20)

3. DC Casting Experiment

The experiments are those performed by Zhang et al. and a detailed description of the experimental setup is found in Refs. [21,28]. Four cylindrical AA7050 billets with a diameter of 315 mm were cast with different casting conditions in a conventional DC casting mold without hot top. The casting temperature was 680 °C and all the billets were grain refined by the same amount of Al5Ti1B master alloy, 2 kg/ton. Two types of melt feeding schemes were used. The melt was poured into the mold either through a semi-horizontal feeding scheme or a vertical feeding scheme. In the former method, the melt was diverted to four branches through a cross-shaped splitter while in the later method, the melt was poured directly in the center of the mold. Two casting speeds were used for each melt feeding scheme. For the semi-horizontal feeding scheme, 50 mm/min and 90 mm/min speeds were used. For the vertical feeding scheme, 50 mm/min and 60 mm/min speeds were used.

The composition of the alloy elements across the billet diameter was measured on points which were about 1 cm apart. The grain size was measured using linear intercept method. The morphology of the grains observed was normally dendritic with the grain size depending on the melt feeding scheme which impacted the sump profile and flow pattern in the liquid pool and slurry zone. The sump profile and the flow pattern were characterized by running 2D computer simulations using ALSIM6 (a casting-simulation software developed by the Institute for Energy Technology, Kjeller, Norway). A low Rayleigh number (LRN) turbulent energy-pseudo turbulent dissipation ($k - \epsilon$) model was used to address the turbulence problem in that simulation.

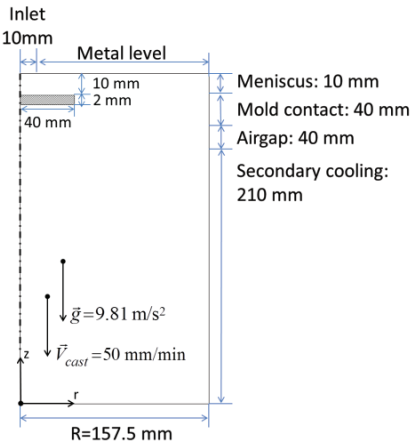

Figure 1: Simplified geometry of the semi-horizontal melt feeding scheme (Inlet 1)

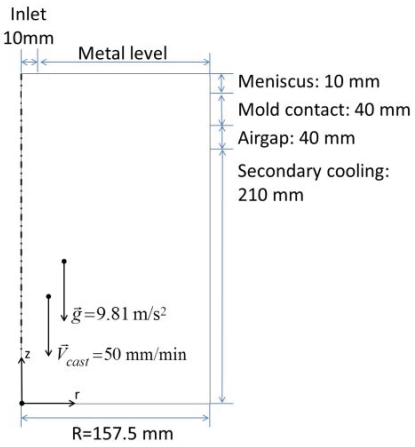

Figure 2: Simplified geometry of the vertical melt feeding scheme (Inlet 2)

4. Problem Description

The experiments are modelled as a 2D axisymmetric problem. The semi-horizontal melt feeding geometry (referred to as Inlet 1 from now on) is simplified by introducing a vertical inlet and a fixed disc 10 mm below the inlet, as shown in Figure 1. The vertical melt feeding geometry (referred to as Inlet 2 from now on) is obtained by removing the fixed disc from the geometry in Figure 1 resulting in the simplified geometry as shown in Figure 2. In this paper, we analyze only the experiments with the casting velocity of 50 mm/min for both inlet schemes. Detailed boundary conditions for energy, liquid and solid momentum are given in Table 2. The inlet velocity is calculated from the global mass balance. The inlet temperature of the liquid metal is fixed at 953.15 K (680 °C), as in the experiments. The heat is extracted by primary cooling through the mold and by secondary cooling directly to the falling water film flowing over the ingot surface. Primary cooling consists of three zones: meniscus, mold, and air gap. The boundary conditions are specified in Table 2 with the ambient temperature (T_{amb}) specified for each boundary. The heat transfer coefficient due to secondary cooling is modelled using Weckmann and Niessen[33] correlation, as shown in Eq. (21).

$$h_{secondary}(T) = \{A + B \cdot (T[\mathrm{K}] + T_{water}[\mathrm{K}])\} \cdot \left(\frac{Q_{water}}{P}\right)^{\frac{1}{3}} + C \cdot \frac{(T - T_{sat})^3}{T - T_{water}} \quad (21)$$

$$A = -167000\ [\mathrm{W \cdot s^{\frac{1}{3}} \cdot m^{-8/3}}];$$

$$B = 352\ [\mathrm{W \cdot s^{1/3} \cdot m^{-8/3} \cdot K^{-1}}]; \qquad C = 20.8\ [\mathrm{W \cdot m^{-2} \cdot K^{-2}}]$$

Where $h_{\mathrm{Secondary}}$ is the heat transfer coefficient, T is the surface temperature of the ingot, T_{water} is the water temperature, T_{sat} is the boiling temperature of the water, Q_{water} is the water flow rate per ingot, and P is the ingot perimeter. All parameter values are given in Table 2.

The thermophysical data for AA7050 alloy is given in Table 3. The linearized phase diagram defined by the liquidus slope, partition coefficient and the pure melting temperature, has been adjusted to fit the solidification path of AA7050 calculated from the microstructure code ALSTRUC [34]. The constant solute diffusion coefficients were calculated from Ref. [35] at the liquidus temperature of the nominal alloy. The density of solid accounting for buoyancy effects is assumed to be constant. The liquid density is calculated as function of solid fraction using a solidification path following the Scheil law. The density evolution during solidification for both solid and liquid phase can be seen in Figure 3a. The grain packing fraction as previously mentioned is a model parameter and it is hard to describe its value accurately. In DC casting modelling, packing fraction values used are usually between 0.15 and 0.3[4,23,24,36–38]. In the current work, the packing fraction is set at 0.3. Another poorly understood parameter value is the characteristic length size (l_{KC}) used in the calculation of the permeability of the mushy zone. The characteristic length size is often approximated by the secondary dendrite arm spacing (SDAS) in dendritic grains and by the grain size in globular grains[4]. Dendritic grains are larger than globular grains and the grain structure observed in the experiments is dendritic with an average grain size of ~250μm and ~350 μm [28]. The characteristic length value (75μm) used to describe the permeability of the simulated dendritic grains is a reasonable approximation of the actual SDAS. Also, the same value can be applied to simulate globular grains as they are smaller than dendritic grains.

Table 2: Boundary Conditions for Energy and Liquid Momentum		
Boundary	Energy	Liquid Momentum
Inlet	T_{cast} = 953.15 K	calculated
Metal Level	$h_{primary}$ = 20 W/(m^{2}K) , T_{amb} = 373.15 K	Slip
Meniscus	$h_{primary}$ = 0 W/(m^{2}K)	Nonslip

Mold Contact	$h_{primary}$= 600 W/(m^{2}K) , T_{amb} = 293.15 K	Nonslip
Air Gap	$h_{primary}$ = 120 W/(m^{2}K) , T_{amb} = 293.15 K	Nonslip
Direct Chill	Based on Equation (21) , $T_{amb} = T_{water} = 293.15$ K, $T_{sat} = 373.15$ K $Q_{water} = 40\ l/min$	Nonslip
Outlet	-	-

The size distribution for TiB_2 inoculant particles is taken from Ref. [39] for 2 kg/ton of grain refiner of type Al-Ti-B. The distribution is modeled by an exponential function for inoculant diameters between 1 and 10 µm. The distribution density function of the population of inoculant particles, when, as usually, represented as a function of the particle diameter, is continuously decreasing. However, when expressed as a function of the critical undercooling, this distribution reaches a maximum at around 0.5 °C, as can be seen in Figure 3b. In the present study, the distribution is discretized into 20 classes: undercooling intervals are defined by increasing step size from 0.1 to 2.1 °C. The inoculant density distribution and the undercooling intervals used for the discretization are shown in Figure 3b.

Table 3: Thermophysical data for AA7050 alloy used in the numerical simulations.

Property	**Unit**	**Value**	**Property**	**Unit**	**Value**
c_p	J.kg^{-1}.K^{-1}	1.3x10^3	ρ_l	kg/m^3	2468.7
L_f	J kg^{-1}	3.63x10^5	ρ_s	kg/m^3	2617.9
Γ_{GT}	K.m	1.9x10^{-7}	$\rho_{s,b}$	kg/m^3	2538.9
μ_l	N.S.m^{-2}	1.28x10^{-3}	β_T	K^{-1}	-1.1 x10^{-4}
k_l	W.m^{-1}.K^{-1}	75.0	l_{KC}	m	7.5 x10^{-5}
k_s	W.m^{-1}.K^{-1}	185.0	g_{pack}	-	0.3
T_m	K	940.15			
T_{eut}	K	723.15			

Property	**Unit**	**Zn**	**Mg**	**Cu**
$C_{0,i}$	wt.%	6.24	2.05	2.12
$k_{p,i}$	-	0.39	0.29	0.09
$m_{l,i}$	K wt.%$^{-1}$	-2.81	-3.88	-4.09
$D_{l,i}$	m^2 s^{-1}	2.682x10e^{-9}	7.326x10^{-9}	4.372x10^{-9}
$D_{s,i}$	m^2 s^{-1}	2.385x10e^{-12}	1.664x10^{-12}	8.363x10^{-13}
$\beta_{c,i}$	(wt.%)$^{-1}$	-1.23 x10^{-2}	4.0x10^{-3}	-7.3x10^{-3}

The transport equations are solved with a Finite Volume Method (FVM) and the SIMPLE-algorithm for staggered grid is used for pressure-velocity coupling. A SIMPLE algorithm based FVM code has been previously employed by Založnik et al. [40] to compare with a highly accurate spectral code to simulate the unsteady thermal natural convection in a cavity, in conditions representative of DC casting. They showed that the SIMPLE based FVM code can be highly accurate to resolve the flow physics. This establishes our confidence in using SIMPLE algorithm for the current work. The convective terms are discretized with a first-order upwind scheme and for time discretization a fully implicit first-order scheme is used. For all simulations a structured grid of 8192 cells ($N_r \times N_z$ =64x128) is employed. Submerged boundary conditions are used to account for the fixed disc below the inlet for Inlet 1. The time step (for macroscopic transport) is set constant to 0.03 s and the simulations are run until steady-state conditions prevail. Each case took around 8h of CPU time using 8 physical cores in Abel computer

cluster. The cluster has compute nodes with 64 GiB memory and use the Linux Operating system (64 bit CentOS 6).

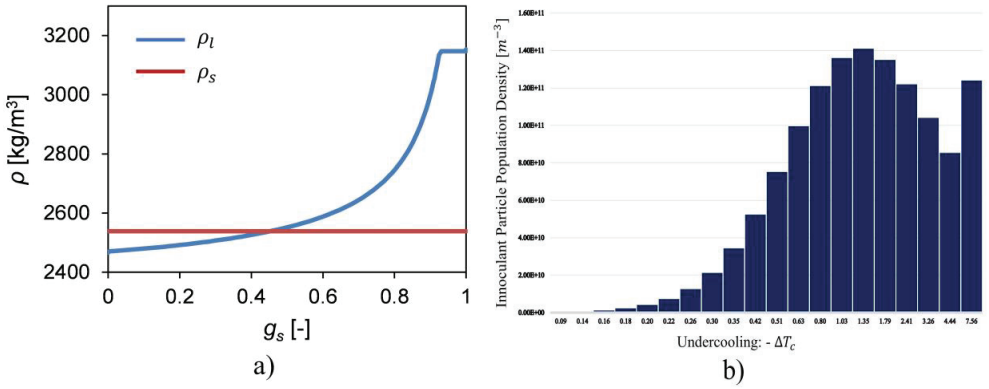

Figure 3: a) Density as a function of solid fraction using the Scheil model for the solidification path and b) inoculant distribution.

5. Results and Discussion

All studied cases are summarized in Table 4. A total of four cases (1-4) based on the inlet mechanism and grain growth model are considered. Similar to the flow characterization done in Zhang et al. [21,28], a Low Rayleigh number (LRN) turbulent energy-pseudo turbulent dissipation ($k-\epsilon$) model was used to address the turbulence problem in this simulation. For Case 1 and Case 3, a globular grain morphology is realized by imposing $g_{env} = g_s$. For Case 2 and 4, the grain morphology is simulated, revealing the impact of dendritic growth.

Table 4: Simulation Cases

Description	Case
Inlet 1 – Globular Grain Growth Model	1
Inlet 1 – Dendritic Grain Growth Model	2
Inlet 2 – Globular Grain Growth Model	3
Inlet 2 – Dendritic Grain Growth Model	4

5.1. Inlet 1

Figure 4a shows the macrosegregation pattern of Zn (Mg and Cu closely follow Zn similar to experimental observations and are not plotted in this work) together with relative velocity, $\vec{v}_l - \vec{V}_{cast}$, vectors for Case 1. For the sake of simplicity, from now on we remove the averaging terms when describing the solid and liquid velocities ($\langle\vec{v}_l\rangle^l = \vec{v}_l$ and $\langle\vec{v}_s\rangle^s = \vec{v}_s$). The impact of forced convection due to the fixed disc is restricted close to the surface as can be seen from the direction of relative velocity vectors. Close to the surface the cooling rate is high, which results in rapid grain growth and only a narrow region of slurry regime ($0<g_s<g_{pack}$) is observed. Thus, the contribution from grain motion is less significant close to the surface and the macrosegregation formation is primarily from natural and forced convection (liquid flow through packed solid phase) and shrinkage induced flow which acts in the packed regime (indicated by arrows perpendicular to solid fraction contours). The cooling rate decays towards the center of the billet and the size of the slurry region grows. Grain transport significantly affects the shape of the sump and the evolution of the solid fraction towards the center of the billet. Since the solid density is higher than liquid density up to solid fraction 0.5 (Figure 3a), grains tend to

settle down at the center of the billet resulting in negative segregation. The settling of the grains results in expulsion of liquid in the upward direction which can be seen in Figure 4c. Shrinkage induced flow also acts in this region but in the packed regime which also contributes to the negative segregation. The overall macrosegregation profile as shown in Figure 6a for Case 1 has negative segregation at the center of the billet and slightly positive segregation towards the surface. Comparing the radial profile for Case 1 with experimental profile shows an over prediction of negative segregation at the center of the billet and in-sufficient prediction of the sub-surface and surface segregation.

For Case 2, we introduce the dendritic model. As the evolution of the envelope fraction differs from the solid fraction, the instant of grain packing occurs at a lower solid fractions for increasing degree of dendritic morphology. The radial profile of internal solid fraction ($g_{intern} = g_s/g_{env}$) at the packing is plotted in Figure 7a for Case 2. Globular morphology is observed for an internal solid fraction value close to 1, whereas dendritic morphology is observed for internal solid fraction value close to 0. Due to increased cooling rate and local undercooling, the grains become more dendritic towards the cooled surface. As we move towards the center of the billet, the cooling rate decays but grain transport also has a strong impact on the cooling rate. The cooling rate of an individual free-floating equiaxed grain depends on the trajectory it makes through the mushy zone. At the center there are a lot of grains that went through slow cooling not only because the distance between the liquidus and solidus is larger in the center, but primarily because they traveled a long distance through a very weakly undercooled slurry zone before settling. Their growth was thus even slower than that indicated by the estimation given by the mushy zone thickness. As a result, the grains are more globulitic towards the center. This feature is well reproduced by the radial profile in Figure 7a. The impact of the grain motion on the grain growth is shown in Figure 8a the map of constitutional undercooling in the solidification zone clearly shows that nucleation occurs only in a very limited region adjacent to the packing front in the outer half of the billet. Grains found in the billet center are thus also generated in the nucleation region and go through a prolonged stage of slow growth on their trajectory to the final position. We can also observe that the maximum in the experimental profile of grain size (at around 100 mm from the centerline), shown in Figure 6c, coincides with the point of detachment of the flow from the packing front. It is probable that the peak in grain size appears here because there is no grain nucleation and only weak grain settling at this location. Close to the surface only a narrow region of grain motion is observed as the grains pack at a low solid fraction and the permeability is sufficiently high to allow a significant liquid velocity through the packed region. This can be seen in Figure 4b. Consequently, the macrosegregation close to the surface is primarily formed by forced and thermal- solutal convection through the packed solid, resulting in negative segregation close to the surface and positive segregation towards mid-radius. Towards the center of the billet as the grains become less dendritic, grain transport becomes an important mechanism. Similar to globular grains in the previous case, dendritic (or slightly globulitic) grains settle at the center of the billet. This results in expulsion of solute rich liquid indicated by the upward arrows in Figure 4d. Since dendritic grains pack at lower solid fractions, the intensity of solute depletion is less severe when compared with Case 1 with globular grains. Finally, the shrinkage induced flow acts in similar fashion as in Case 1, producing negative segregation at the center and positive segregation towards the surface.

The grain morphology given by the dendritic model clearly indicates a tendency towards globularization or dendritization of the local equiaxed microstructure but is not to be considered as quantitatively predictive. The predictions depend somewhat on the choice of assumptions and constitutive models, the envelope shape and the primary tip growth kinetics having the largest impact. The present model assumes a spherical envelope shape and hemispherical dendrite tips. Different pertinent models have been used in literature: envelopes of spherical[31,41–43], octahedral[4,11,12,42,44] and hexapod[12] shape, and dendrite tip growth laws based on hemispherical and paraboloidal tips. Generally, spherical envelopes lead to smaller specific envelope surface area per grain volume and to larger fractions of intergranular liquid[11]. As shown in several studies[11,42,45,46], spherical envelopes lead to predictions of somewhat smaller internal solid fraction than octahedral envelopes. This is mainly due to the larger volume of the envelopes, while the volume of the solid phase remains very similar. The stronger assumption is that of hemispherical tips. At the same undercooling, hemispherical tips grow significantly faster than

paraboloidal tips. Detailed analyses have shown that at given solidification conditions the hemispherical tip model predicts a more dendritic grain morphology than the paraboloidal tip model[4,42,46]. While a similar globular-dendritic transition is predicted with both models, the transition from dendritic to globular is shifted to higher grain densities or lower cooling rates with the hemispherical tip model. For example, Nielsen et al.[42] argued that the spherical envelope and the hemispherical tip model gave better predictions of the experimentally observed morphologies of interacting grains in inoculated Al-Cu alloys than the paraboloidal tip model and octahedral envelopes. The physical reasons for this were not explained, but it is clear that dendrite growth models based on models of free dendritic growth are rather simplistic for describing the growth of strongly interacting grains and that improved constitutive models are needed[47].

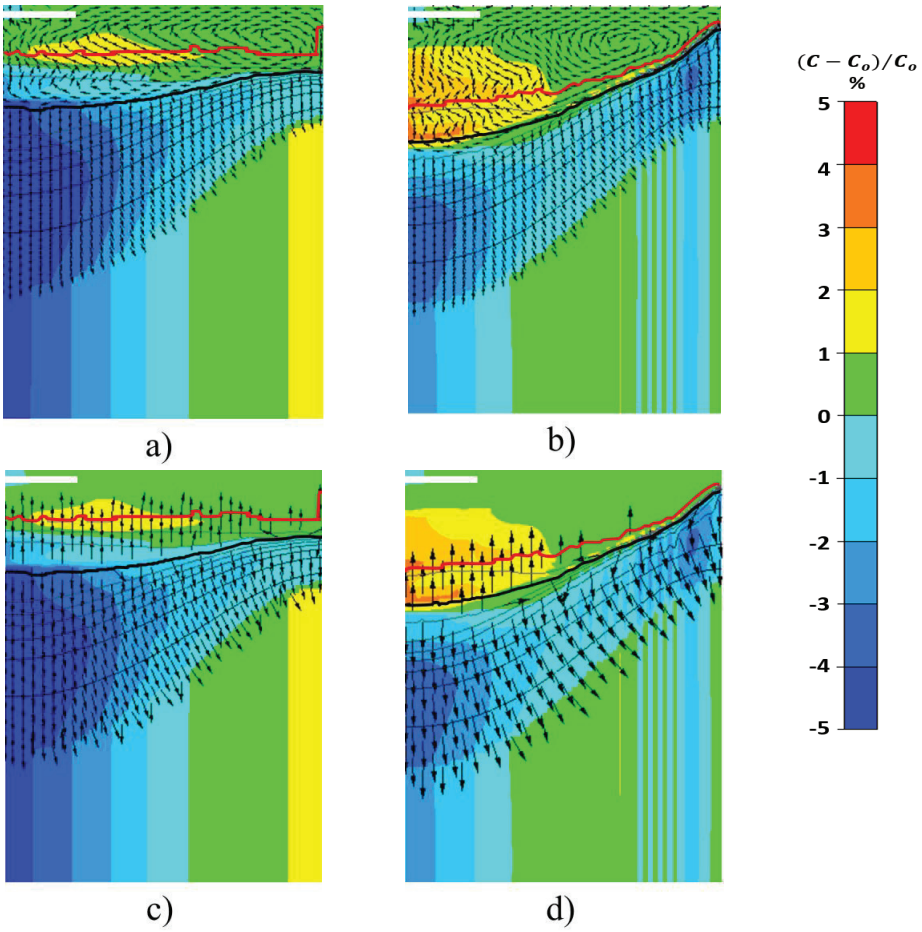

Figure 4: a) & b) Relative composition of Zn in % together with relative velocity $\vec{v}_l - \vec{V}_{cast}$ vectors and iso-lines of solid fraction for Case 1 and envelope fraction for Case 2; c) & d) Relative composition of Zn in % together with relative velocity $\vec{v}_l - \vec{v}_s$ vectors and iso-lines of solid fraction for Case 1 and envelope fraction for Case 2. Only right half of the cross-section of the billet is shown with the left vertical edge corresponds to symmetric axis. The liquidus and the packing front are marked by thick red and black curves. e) The common color bar of relative segregation for all cases.

The final macrosegregation profile for Case 2 is shown in Figure 6a along with Case 1 and with the experimental profile. The intensity of centerline negative segregation and mid-section positive segregation is very well reproduced by Case 2 when compared with experiment. The surface and sub-surface segregation is only qualitatively reproduced. This region is strongly influenced by forced convection and this could be the main source of error. In the current simulation, the semi-horizontal melt feeding scheme used in the experiments is simplified by an inlet-distributor setup. This might not reproduce the accurate flow pattern which can affect the macrosegregation formation close to the surface. Figure 6c shows the grain sizes for Case 1 and 2 against the experimentally measured grain size. From the experimental profile, the grains are smallest close to the surface where the cooling rate is high. Grains coarsen towards the center of the billet due to the decayed cooling rate. These variations are not predicted by the numerical model that predict a rather flat profile. The grain size predicted by Case 2 towards the surface compares well with experimental data.

5.2. Inlet 2

Figure 5a shows the macrosegregation pattern of Zn together with relative velocity $\vec{v}_l - \vec{V}_{cast}$ vectors for Case 3. Compared to the flow patten observed in Inlet 1, the flow pattern seen in Inlet 2 is completely different due to vertical jet towards the center of the billet. Two flow loops can be seen – a counter clockwise loop in the center area and a clockwise loop at the quarter and surface of the billet. They collide around 40mm from the center of the billet. The resulting solid fraction profile shows a cliff shaped (almost vertical solidification front) pattern around this region. A similar flow pattern and solidification front is seen in the simulated profiles using ALSIM6 in the Ref[28].

At the center of the billet, macrosegregation formation is mainly due to washing of the solute due to the strong upstream flow due to forced convection. This can cause severe depletion near the cliff shaped region. Additonal cause of negative segregation is due to stacking up of globular grains which are formed next to the cliff or formed earlier at other locations and arrived there with the melt flow. The collision of two flow loops around this vertical solidifcation front blocks the horizontal movement of the solid grains. Hence, the suspension of grains and washing away of solute due to forced convection results in severe depletion in this region. In addition, shrinkage induced flow also adds to the negative segregation. The segregation profile can be seen in Figure 6b. In the mid-section, we can observe some depletion. The forced convection is not strong in this area and the major contribution for macrosegregation is grain settling indicated by the solutal stratification (upward vectors) shown in Figure 5c. Towards the surface we can see positive segregation which can be explained due to grain settling in the mid-section region. As grains settle in the mid-section, the stratified solute is caught up in the clockwise flow loop and gets deposited towards the surface resulting in positive segregation. Shrinkage induced flow additionally contributes to positive segregation in this region. Comparison with experimental profile shows that for Case 3 (Figure 6b) there is an over prediction of negative segregation at the center and in-accurate prediction of macrosegregation at the mid-section and towards the surface.

For Case 4, we employ the dendritic model. The flow pattern for this case shown in Figure 5b is similar to the flow pattern for Case 3 shown in Figure 5a. The only difference is that the grains are dendritic in Case 4. A measure of dendritic morphology can be seen in Figure 7b. We could not track the internal solid fraction profile at the center due to limited or non-existent grain motion. Around 40 mm away from the center, some dendritic grains were observed with slightly globulitic morphology ($g_{intern} \sim 0.6$). The stacking up of dendritic grains along the vertical solidification front was similar to what was observed with globular morphology in Case 3 but the intensity of segregation was less severe due to packing of dendritic grains at lower solid fractions. Nonetheless, additional depletion of solute occurs in the center due to forced convection and shrinkage induced flow. In the mid-section, grain settling dominates which can be seen in solutal stratification from Figure 5d. But due to the dendritic morphology in this region ($g_{intern} \sim 0.3$), the intensity of negative segregation due to grain settling is not severe. So is the stratification of solute which gets caught up in the clockwise flow loop to get deposited towards the

surface. The main contributor for macrosegregation in sub-surface and surface area is shrinkage induced flow which results in negative and positive segregation respectively.

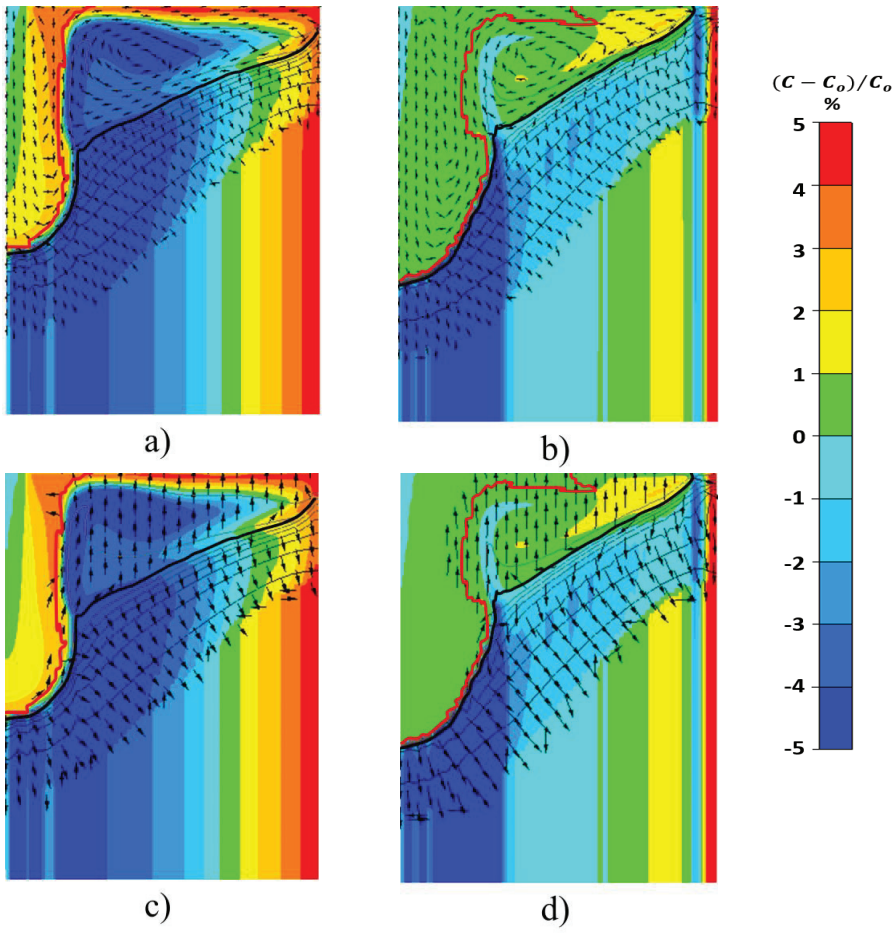

Figure 5: a) & b) Relative composition of Zn in % together with relative velocity $\vec{v}_l - \vec{V}_{cast}$ vectors and iso-lines of solid fraction for Case 3 and envelope fraction for Case 4; c) & d) Relative composition of Zn in % together with relative velocity $\vec{v}_l - \vec{v}_s$ vectors and iso-lines of solid fraction for Case 3 and envelope fraction for Case 4. Only right half of the cross-section of the billet is shown with the left vertical edge corresponds to symmetric axis. The liquidus and the packing front are marked by thick red and black curves. e) The common color bar of relative segregation for all cases.

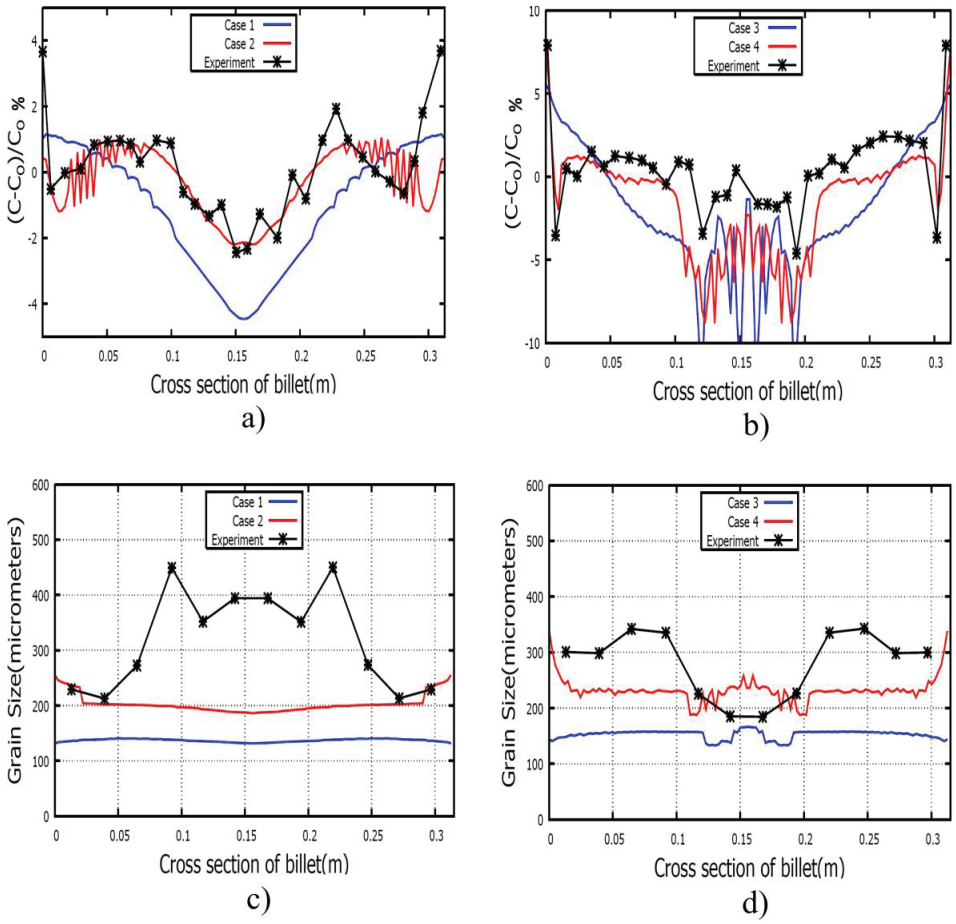

Figure 6: a) Radial profile of macrosegregation in Zn from simulation shown for Case 1 and Case 2; b) Radial profile of macrosegregation in Zn from simulation shown for Case 3 and Case 4; c) Radial profile of grain size from simulation shown for Case 1 and Case 2; d) Radial profile of grain size from simulation shown for Case 3 and Case 4. Experimental profile shown in black for both macrosegregation and grain size.

Comparison with experimental profile shows that for Case 4 (Figure 6b) there is an over prediction of negative segregation at the center. Though it should be noted that depletion of solute in the center is not as intense as in Case 3 where we consider globular grains. In the mid-section the simulated profile from Case 4 qualitatively follows the experimental profile and a very good co-relation between the both can be seen towards the surface. Case 4 macrosegregation profile compares reasonably well with experiment with some discrepancy in the center. This could possibly be explained by over prediction insufficient resolution of turbulence (only 2 equation model) which results in washing away of the solute in the center. In Figure 6d, we compare the radial profile of grain sizes measured during experiment with simulated profiles from Case 3 and 4. In the vertical melt feeding scheme, intense flow is observed at the center. Also due to a vertical solidification front, the cooling rate is quite high in the center. As a result, small grains are observed in the central part of the billet. The grain size increases towards the mid-section and slightly decreases at the surface. Case 3 predicts an almost flat profile for grain sizes.

The order of magnitude of the grain size predicted is right for Case 4 but the variations across the billet diameter are not correctly predicted. The mid-section coarse grain structure seen in the experiment is not directly predicted by Case 4. A more detailed analysis of grain nucleation, growth, and transport, shown in Figure 8b, shows that the reported coarse grain region is located at the meeting point of the two flow circulations. Because of the flow orientation the deposition rate of free-floating equiaxed grains at the meeting point is weak. Also, the meeting point is a region of very low undercooling, i.e., without nucleation of new grains. The structure at this location is therefore composed of few slowly growing grains, resulting in a localized band of coarse grain morphology.

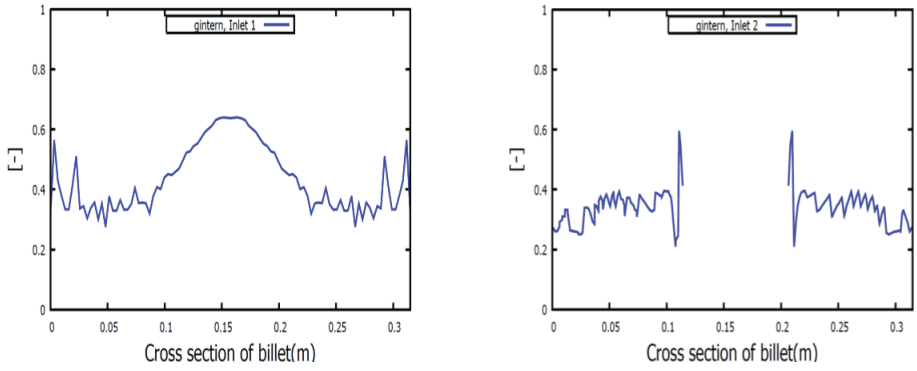

a) b)

Figure 7: Radial profile of internal solid fraction (g_{intern}) at instant of packing for a) Case 2 and b) Case 4

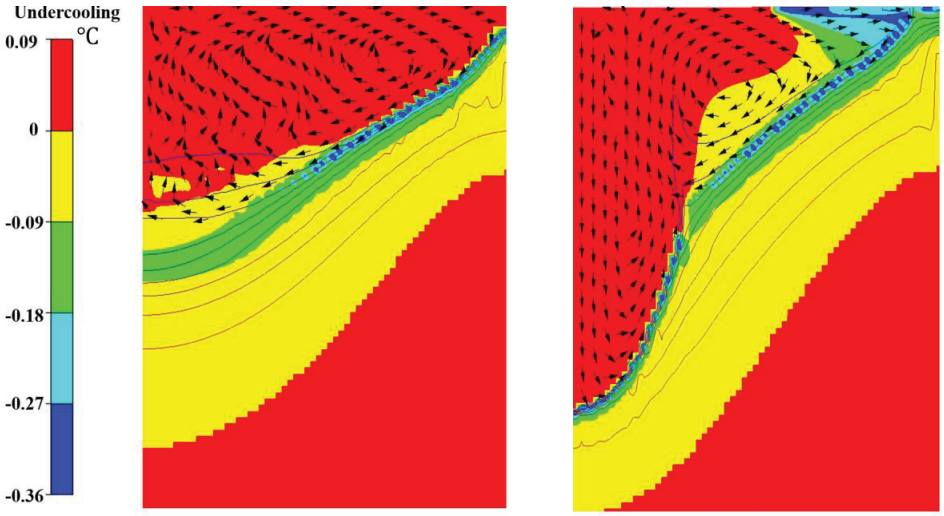

Figure 8: Undercooling (given by Eq. 20) in the billet for a) Case 2 and b) Case 4, indicating regions of nucleation (blue and green), grain growth (yellow) and grain remelting (red). The solid velocity vectors (black) show the grain trajectories through the solidification zone. The lines are isopleths of envelope fraction.

6. Conclusions

A simplified three-phase, multiscale solidification model coupling macroscopic transport and equiaxed grain growth was previously proposed[3]. This model was novel in its approach as it introduces three phases in describing equiaxed grain growth but solves only two-phase macroscopic transport equations. A limited demonstration of the model to predict macrosegregation in DC casting accounting for grain morphology was done previously. In this paper we conducted a proper validation study by both imposing globular morphology and simulating dendritic morphology and comparing with experiments.

Two different types of inlet melt flow were considered. In the first type, the geometry was simplified in simulation which resulted in slight variations in macrosegregation prediction towards the surface of the billet when compared with experiment. But the center line depletion and mid-section segregation were well predicted when dendritic morphology was considered. In the second type of inlet, macrosegregation formation predicted by the numerical model considering dendritic morphology could be qualitatively compared with the experimental data. For both types of inlets, globular grain growth model overpredicted the negative segregation at the center and in-accurately predicted macrosegregation in other parts of the billet indicating the necessity of accurate morphology modelling.

Grain size predictions are of the right order of magnitude when compared with experimental observations, especially when dendritic morphology is accounted for. But the variation of the grain size across the cross section of the billet is not accurately predicted by the model for both the type of inlets. Several modelling aspects can affect the grain size and morphology prediction. Packing fraction is one of them and its value is ambiguous. Another aspect is the inaccurate resolution of nucleation zone. In DC casting process, the nucleation zone is quite small and even reasonably fine grids might not be able to resolve it completely. Therefore, this could be a critical factor. Lastly, the current model uses simplified constitutive models to predict grain growth in the presence of important solutal interactions between growing grains. Advanced constitutive models have been proposed recently[47] which could be integrated in the current model. These are some of the aspects which could be clarified in future work.

Acknowledgement

This work is conducted within the framework of PRIMAL project of which Hydro Aluminium ASA, Alcoa Norway ANS, Aleris Rolled Products Germany GmbH, Institute of Energy Technology (IFE), NTNU and SINTEF are the partners. This project is supported by the Research Council of Norway. A.P and M.M acknowledge the support of NOTUR High Performance Computing program. H.C and M.Z. acknowledge the support by the French State through the program "Investment in the future" operated by the National Research Agency (ANR) and referenced by ANR-11 LABX-0008-01 (LabEx DAMAS).

Table 5: Nomenclature

$< C_{i,} >$	average mass concentration of solute i, wt. %	T_{cast}	casting temperature, K
$< C_i^{*,} >$	average equilibrium mass concentration of solute i, wt. %	T_{liq}	temperature of liquidus, K
$C_{o,i}$	mean concentration of solute i, wt. %	T_m	melting temperature of pure Al, K
c_p	specific heat, J.kg^{-1}K	T_{eut}	eutectic temperature, K
C_D	drag co-efficient, -	ΔT	undercooling, K
d	diameter of inoculant particle, m	ΔT_c	critical undercooling for nucleation, K
$D_{,i}$	diffusion coefficient of solute i, $\mathrm{m^2 s^{-1}}$	$\langle \vec{v}_l \rangle^l$	intrinsic average velocity of liquid phase, $\mathrm{ms^{-1}}$

g	volume fraction, -	$\langle \vec{v}_s \rangle^s$	intrinsic average velocity of solid phase, ms^{-1}
g_{pack}	packing fraction, -	$\vec{V}_{cast}$	casting velocity, ms^{-1}
g_{intern}	internal solid fraction, -	V_{tip}	velocity of dendrite tip, ms^{-1}
$\vec{\boldsymbol{g}}$	acceleration due to gravity, ms^{-2}	β_T	thermal expansion coefficient, K
$\langle h_l \rangle^l$	averaged liquid enthalpy, Jkg^{-1}	$\beta_{C,i}$	solutal expansion coefficient of solute i, $\%\mathrm{w}^{-1}$
$\langle h_s \rangle^s$	averaged solid enthalpy, Jkg^{-1}	δ_i	diffusion length of solute i, - m
h_m	mixture enthalpy, Jkg^{-1}	$\delta(t)$	Dirac function
$h_{primary}$	primary cooling heat transfer coefficient, $\mathrm{Wm}^{-2}\mathrm{K}^{-1}$	Γ_{GT}	Gibbs Thomson co-efficient, Km
$h_{secondary}$	secondary cooling heat transfer coefficient, $\mathrm{Wm}^{-2}\mathrm{K}^{-1}$	Γ	growth rate, $\mathrm{kgm}^{-3}\mathrm{s}^{-1}$
$k_{p,i}$	partition coefficient of solute i, -	κ	thermal conductivity, $\mathrm{W.m}^{-1}$. K
K	permeability, m^2	ρ_l	liquid density, kgm^{-3}
L_f	Latent heat of fusion, $\mathrm{J.kg}^{-1}$	ρ_s	solid density used to account for shrinkage, kgm^{-3}
l_{kc}	characteristic length for permeability, m	$\rho_{l,b}$	liquid buoyancy density used to account for Bousinessq approximation, kgm^{-3}
$m_{l,i}$	liquidus slope of solute i, $\mathrm{K\ wt.\%}^{-1}$	$\rho_{s,b}$	solid buoyancy density used to account for grain motion, kgm^{-3}
N_{nuc}^i	volumetric population density, m^{-3}	ρ_m	mixture density, kgm^{-3}
N_g	grain density, m^{-3}	μ_l	liquid dynamic viscosity, Pa s
p_l	liquid pressure, Nm^{-2}		
P	perimeter of the ingot, m		
Q_{water}	water flow rate, $\mathrm{m}^3\mathrm{s}^{-1}$		***Subscripts and Superscripts***
R_{env}	radius of the envelope, m	l	liquid
$R^{s,eq}$	radius of the solid grain, m	s	solid
Re	Reynolds number	env	envelope
S_v	interfacial area density, m^{-1}	e	extragranular liquid
Sc	Schmidts number	d	intragranular liquid
t	time, s	$s\text{-}d$	solid-liquid interface
T	temperature, K	$e\text{-}d$	intra-extra granular liquid interface
T_{water}	temperature of cooling water, K	*	equilibrium
T_{sat}	temperature of boiling water, K	l,b	liquid buoyancy
		s,b	solid buoyancy

7. References

1 A. V. Reddy and N.C. Beckermann: *Metall. Mater. Trans. B*, 1997, vol. 28, pp. 479–89.

2 G. Lesoult, V. Albert, B. Appolaire, H. Combeau, D. Daloz, A. Joly, C. Stomp, G.U. Grün, and P. Jarry: *Sci. Technol. Adv. Mater.*, 2001, vol. 2, pp. 285–91.

3 K.O. Tveito, A. Pakanati, M. M'Hamdi, H. Combeau, and M. Založnik: *Metall. Mater. Trans. A*, 2018, vol. 49, pp. 2778–94.

4 L. Heyvaert, M. Bedel, M. Založnik, and H. Combeau: *Metall. Mater. Trans. A*, 2017, vol. 48, pp. 4713–34.

5 A. Olmedilla, M. Založnik, B. Rouat, and H. Combeau: *Phys. Rev. E*, ,

DOI:10.1103/PhysRevE.97.012910.
6 M. Bedel, K.O. Tveito, M. Založnik, H. Combeau, and M. M'Hamdi: *Comput. Mater. Sci.*, 2015, vol. 102, pp. 95–109.
7 M. Rappaz: *Int. Mater. Rev.*, 1989, vol. 34, pp. 93–124.
8 J. Ni and C. Beckermann: *Metall. Trans. B---Process Metall.*, 1991, vol. 22, pp. 349–61.
9 C.Y. Wang and C. Beckermann: *Metall. Mater. Trans. A*, 1996, vol. 27A, pp. 2754–64.
10 M. Wu, A. Ludwig, A. Buhrig-Polaczek, M. Fehlbier, and P.R. Sahm: *Int. J. Heat Mass Transf.*, 2003, vol. 46, pp. 2819–32.
11 M. Wu and A. Ludwig: *Acta Mater.*, 2009, vol. 57, pp. 5621–5631.
12 M. Wu, A. Fjeld, and A. Ludwig: *Comput. Mater. Sci.*, 2010, vol. 50, pp. 43–58.
13 M. Založnik and H. Combeau: *Comput. Mater. Sci.*, 2010, vol. 48, pp. 1–10.
14 H. Combeau, M. Založnik, S. Hans, and P.E. Richy: *Metall. Mater. Trans. B Process Metall. Mater. Process. Sci.*, 2009, vol. 40, pp. 289–304.
15 A. Kumar, M. Založnik, and H. Combeau: *Int. J. Adv. Eng. Sci. Appl. Math.*, 2010, vol. 2, pp. 140–8.
16 J. Li, M. Wu, A. Ludwig, and A. Kharicha: *Int. J. Heat Mass Transf.*, 2014, vol. 72, pp. 668–79.
17 M. Wu, A. Ludwig, and A. Kharicha: *Steel Res. Int.*, 2018, vol. 89, pp. 1–14.
18 T. Jalanti: PhD Thesis, Ecole Polytechnique Fédérale de Lausanne, Laussanne, Switzerland, 2000.
19 C.J. Vreeman and F.P. Incropera: *Int. J. Heat Mass Transf.*, 2000, vol. 43, pp. 687–704.
20 M. Založnik and B. Šarler: *Model. Cast. Weld. Adv. Solidif. Process. XI*, 2006, pp. 243–50.
21 L. Zhang, D.G. Eskin, A. Miroux, T. Subroto, and L. Katgerman: *IOP Conf. Ser. Mater. Sci. Eng.*, 2012, vol. 33, pp. 1–8.
22 Q. Du, D.G. Eskin, and L. Katgerman: *Metall. Mater. Trans. A Phys. Metall. Mater. Sci.*, 2007, vol. 38, pp. 180–9.
23 A. V. Reddy and C. Beckermann: *Mater. Process. Comput. Age II*, 1995, pp. 89–102.
24 M. Založnik, A. Kumar, H. Combeau, M. Bedel, P. Jarry, and E. Waz: *Adv. Eng. Mater.*, 2011, vol. 13, pp. 570–80.
25 A. Hakonsen, D. Mortensen, S. Benum, and H.E. Vatne: in *Light Metals*, TMS, Warrendale, PA, 1999, pp. 821–7.
26 M. Bedel, L. Heyvaert, M. Založnik, H. Combeau, D. Daloz, and G. Lesoult: *IOP Conf. Ser. Mater. Sci. Eng.*, 2015, vol. 84 (1), pp. 1–8.
27 H. Combeau, M. Založnik, and M. Bedel: *Jom*, 2016, vol. 68, pp. 2198–206.
28 L. Zhang, D.G. Eskin, a. Miroux, T. Subroto, and L. Katgerman: *Metall. Mater. Trans. B Process Metall. Mater. Process. Sci.*, 2012, vol. 43, pp. 1–9.
29 M. Založnik, A. Kumar, and H. Combeau: *Comput. Mater. Sci.*, 2010, vol. 48, pp. 1–10.
30 A.L. Greer, A.M. Bunn, A. Tronche, P. V. Evans, and D.J. Bristow: *Acta Mater.*, 2000, vol. 48, pp. 2823–35.
31 M. Rappaz and P.H. Thévoz: *Acta Metall.*, 1987, vol. 35, pp. 2929–33.
32 M. Rappaz and W.J. Boettinger: *Acta Mater.*, 1999, vol. 47, pp. 3205–19.
33 D. Weckman and P. Niessen: *Metall. Trans. B*, 1982, vol. 13, pp. 593–602.
34 A.L. Dons, E.K. Jensen, Y. Langsrud, E. Trømborg, and S. Brusethaug: *Metall. Mater. Trans. A*, 1999, vol. 30, pp. 2135–2146.
35 Y. Du, Y.A. Chang, B. Huang, W. Gong, Z. Jin, H. Xu, Z. Yuan, Y. Liu, Y. He, and F.Y. Xie: *Mater. Sci. Eng. A*, 2003, vol. 363, pp. 140–51.
36 C.J. Vreeman, M.J.M. Krane, and F.P. Incropera: *Int. J. Heat Mass Transf.*, 2000, vol. 43, pp. 677–86.
37 I. Vušanović and M.J.M. Krane: *IOP Conf. Ser. Mater. Sci. Eng.*, , DOI:10.1088/1757-899X/27/1/012069.
38 A. Pakanati, K.O. Tveito, M. M'Hamdi, H. Combeau, and M. Založnik: in *In: Martin O. (eds) Light Metals 2018. TMS 2018. The Minerals, Metals & Materials Series. Springer, Cham*, 2018, pp. 1089–96.
39 A. Tronche: PhD Thesis, University of Cambridge, Cambridge, England, 2000.

40 M. Založnik, S. Xin, and B. Šarler: *Int. J. Numer. Methods Heat Fluid Flow*, 2008, vol. 18, pp. 308–24.
41 C.Y. Wang and C. Beckermann: *Metall. Trans. A*, 1993, vol. 24, pp. 2787–802.
42 Ø. Nielsen, B. Appolaire, H. Combeau, and A. Mo: *Metall. Mater. Trans. A Phys. Metall. Mater. Sci.*, 2001, vol. 32, pp. 2049–60.
43 M.A. Martorano, C. Beckermann, and C.A. Gandin: *Metall. Mater. Trans.*, 2003, vol. 32, pp. 1657–74.
44 B. Appolaire, H. Combeau, and G. Lesoult: *Mater. Sci. Eng. A*, 2008, vol. 487, pp. 33–45.
45 M. Wu and A. Ludwig: *Acta Mater.*, 2009, vol. 57, pp. 5632–44.
46 M. Bedel: PhD Theses Université de Lorraine, Nancy,France, 2014.
47 M. Torabi Rad, M. Založnik, H. Combeau, and C. Beckermann: in *Solidification Processing 2017: Proceedings of the 6th Decennial International Conference on Solidification Processing*, 2017, pp. 326–9.

Paper V

IMPACT OF INLET FLOW ON MACROSEGREGATION FORMATION ACCOUNTING FOR GRAIN MOTION AND MORPHOLOGY EVOLUTION IN DC CASTING OF ALUMINIUM

Akash Pakanati, Knut Omdal Tveito, Mohammed M'Hamdi, Hervé Combeau and Miha Založnik

Paper VI

3D NUMERICAL ANALYSIS OF MACROSEGREGATION FORMATION IN DC CASTING OF ALUMINIUM ALLOYS ACCOUNTING FOR INLET FLOW AND GRAIN MORPHOLOGY

Akash Pakanati, Mohammed M'Hamdi, Hervé Combeau and Miha Založnik